THE UNIVERSITY OF CHICAGO

ULTRAFAST ENERGY TRANSFER AND ORIENTATIONAL DYNAMICS IN PHOTOSYNTHETIC BACTERIAL MEMBRANES

A DISSERTATION SUBMITTED TO
THE FACULTY OF THE DIVISION OF THE PHYSICAL SCIENCES
IN CANDIDACY FOR THE DEGREE OF
DOCTOR OF PHILOSOPHY

DEPARTMENT OF CHEMISTRY

BY
SARA CHAMBERLIN MASSEY

CHICAGO, ILLINOIS
JUNE 2019

To my husband, Kyle, my son, Jake, and my daughter, Ava. Thank you for bringing me joy!

TABLE OF CONTENTS

LIST OF FIGURES

LIST OF TABLES

ACKNOWLEDGMENTS

Thank you to my parents, Mary and Jim Chamberlin, and my siblings, Rachel Monroe and Derek Chamberlin, for supporting me and encouraging me through every step of life. Thank you to my family, Kyle, Jake, Ava, and Cosmo for making my time in graduate school some of the most joyful years of my life. I appreciate your understanding, your unwavering support, and the many laughs and smiles you bring me each day.

I thank Prof. Gregory Engel for being an extraordinarily supportive research advisor. Thank you for encouraging me to forge my own path, for offering guidance when I needed it, for giving me the confidence and creative freedom to design my own projects and experiments, and for allowing me the space to pursue my unique interests. Thank you for believing in me.

I was supported by a National Defense Science and Engineering Graduate (NDSEG) Fellowship from the Department of Defense, Air Force Office of Scientific Research (AFOSR). The research presented here was additionally funded by the Vannevar Bush Faculty Fellowship program and AFOSR, and completed in part with resources provided by the National Science Foundation MRSEC and the University of Chicago Research Computing Center.

I would like to thank my collaborators in the Hunter Group, Prof. C. Neil Hunter, Elizabeth Martin, Dr. Andrew Hitchcock, and Dr. Craig MacGregor-Chatwin for generously providing me with mutant *Rba. sphaeroides* cells and mutant *Synechocystis* sp cells and membrane fragments. I also thank my theory collaborators, Dr. Shu-Hao Yeh and Prof. Sabre Kais. I am grateful to Dr. Sarah R. Soltau for training me in the isolation of the LH2 pigment-protein complex and to the Photosynthesis group at Argonne National Laboratory for sharing their facilities and expertise.

I am so grateful to have found a supportive, collaborative group of young scientists in the Engel Group who have pushed me scientifically and also provided the scaffolding to help me succeed: my mentors, Dr. Moira Flanagan and Dr. Peter Dahlberg, my peers, Dr. John Otto, Dr. Nicholas Williams, and Po-Chieh Ting, my fellow Condon labmates, Sara Sohail, Jacob Higgins, Nicholas "Lil'Nick" Cleland, Dr. Marco Allodi, and Danika Nimlos, as well

as Elizabeth Bain, Lawson Lloyd, Richard Mazuski, Dr. Lili Wang, and Ryan Wood. I am thankful for these individuals and for all of the other Engel Group members, past and present, who laid the foundation for my work, tinkered with me, and challenged me to grow as a scientist, colleague, and mentor. I thank Dr. Karen Watters for scientific editing and helping me improve as a writer.

I thank Dr. Britni Ratliff for being an incredible example of an effective and thoughtful teacher, for pushing me to pursue training in pedagogy, for introducing me to the collaborative learning classroom, and for mentoring me throughout graduate school. I thank Prof. Scott Snyder and Prof. Andrei Tokmakoff for giving me the invaluable opportunity to teach Introductory General Chemistry here at UChicago, and Dr. Vera Dragisich for helping me grow personally and professionally over the years. I am grateful to my undergraduate research advisor, Prof. Katherine Willets, and my undergraduate physical chemistry professor, Prof. John Stanton, for believing in me from the start and continuing to support and encourage me over the years.

I acknowledge my first-year cohort for their wonderful support as well as their commiseration. To Darren Veit, Dr. Daniel Micheroni, Dr. Anthony Schlimgen, Hannah Rutledge, Edward Prybolsky, Dr. Nicole James, Dr. Michael Lueckheide, and Dr. Manas Sajjan. Thank you to University Ballet of Chicago for providing me with a creative outlet outside of the lab.

I am grateful to my committee members, Prof. Andrei Tokmakoff and Prof. Sarah King, for their guidance and mentorship.

ABSTRACT

Photosynthetic organisms have adapted to survive in their diverse native habitats, whether by maximizing light-harvesting efficiency in low-light environments or by quenching excess excitations to prevent the formation of damaging reactive oxygen species. Photosynthetic species follow a number of principles in the design of pigment-protein light-harvesters, including the dense packing of chromophores, repeating the same pigment many times, and using interactions with other pigments and the environment to tune the absorbance spectrum. We seek to understand the ultrafast dynamics of light harvesting in these organisms that take place on the femtosecond (10^{-15} s) timescale. In this thesis, I track energy moving through both energetically distinct and degenerate states by integrating ultrafast two-dimensional electronic spectroscopy with anisotropy and power-dependence experiments. I present results on the ultrafast energy transfer processes in the anoxygenic photosynthetic purple bacterium *Rhodobacter sphaeroides* and the oxygenic cyanobacterium *Synechocystis* sp PCC 6803 in their native membrane environments. Both of these organisms use light-harvesting antenna complexes to collect light energy and funnel that energy to an energetic trap known as the reaction center which produces a trans-membrane electron gradient that drives photosynthetic reactions.

In *Rhodobacter sphaeroides*, we collected the first two-dimensional electronic anisotropy spectra, revealing time-dependent dynamics of the transition dipole orientations in membrane-bound light harvesting complex 2 (LH2). This pioneering spectroscopy reveals orientational preferences for sequential absorption processes, ultrafast intra-band equilibrations, and differentiates energy transfer processes from spectrally overlapped states that are otherwise unresolvable. We investigated light-harvesting pathways in LH2 from organisms grown under varied light and oxygen conditions to determine whether an energy quenching pathway was introduced. We present a revised picture of the B850 dynamics in LH2, showing power dependent dynamics that were previously thought to be inherent to the B850 ring.

The first two-dimensional spectra of intact cyanobacterial thylakoid membranes are also

presented here. We seek to disentangle the spectral contributions of the fused antenna/reaction center photosystems in *Synechocystis* sp PCC 6803 and map out inter-complex energy transfer. Mutations deleting specific portions of the photosynthetic machinery enable us to attribute spectral features and dynamics to specific complexes that would otherwise be indistinct. Future planned experiments include the investigation of cyanobacterial photoprotection and the effect of iron stress on energy transfer pathways.

CHAPTER 1

INTRODUCTION TO ENERGY TRANSFER IN LIGHT HARVESTING

1.1 Photosynthetic Light Harvesting

Photosynthetic organisms use a funnel-like scheme to collect solar photons and transfer excitations from the site of energy absorption to the site of charge separation on the picosecond timescale. Light-harvesting antennae are pigment-protein complexes consisting of densely packed chromophores, such as chlorophyll, bacteriochlorophyll, bilins, and carotenoids, held by a protein scaffold. There are usually many antennae that collect and shuttle energy to a photosynthetic reaction center in a downhill energy gradient. These light-harvesting principles are ubiquitous, spanning photosynthetic bacteria, algae, and plants. This thesis will focus on light-harvesting in photosynthetic bacteria: specially the purple bacterium *Rhodobacter sphaeroides* (*Rba. sphaeroides*) and the cyanobacterium *Synechocystis* sp PCC 6803.

1.1.1 Light Harvesting in Purple Bacteria

Purple bacteria such as *Rba. sphaeroides* are anoxygenic photosynthetic bacteria native to lake bottoms, mud, and soil environments. *Rba. sphaeroides* can grow phototrophically under light or chemoheterotrophically under dark conditions. [1] These organisms form spherically shaped intracytoplasmic membrane vesicles called chromatophores which are densely embedded with integral membrane pigment-protein complexes. [2] The arrangement of the light-harvesting complexes is illustrated in Figure 1.1. The bacterial light-harvesting complex 2 (LH2) acts as a peripheral light-harvester and transfers energy downhill to light-harvesting complex 1 (LH1) which encircles and directs energy to the bacterial reaction center (RC). The LH2 complex is composed of 9 subunits containing an α/β heterodimer with 3 bac-

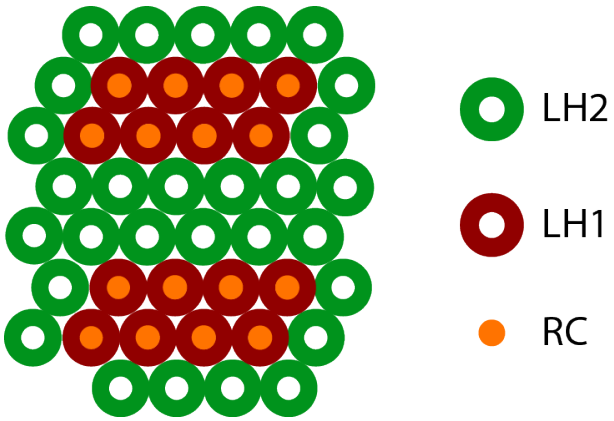

Figure 1.1: Illustration of the organization of light-harvesting complexes in the purple bacterial photosynthetic membrane. The photosynthetic unit is composed of 2 pools of 4 dimers light-harvesting 1 complexes (LH1, red) surrounded by 29 light harvesting 2 complexes (LH2, green). [5] Each LH1 monomer encircles a reaction center (RC, orange). Figure adapted from Reference [5] under the Creative Commons license https://creativecommons.org/licenses/by/4.0/legalcode.

teriochlorophyll a (BChl a) and a carotenoid molecule. The resulting ring structure has C_9 symmetry with two distinct rings of BChl: the lower energy B850 ring of 18 strongly coupled BChl with an absorbance maximum at 850 nm and the higher energy B800 ring of 9 less strongly coupled BChl with an absorbance maximum at 800 nm. [3] The Soret band (350-430 nm), Q_x band (585-605 nm), and Q_y bands (780-870 nm) of BChl a and S_2 band (430-550 nm) of carotenoids provide LH2 with broadband absorption across the visible and near-infrared (IR) spectrum. This broad absorption cross-section allows the organism to absorb most incident light. The Q_y absorbance of LH1 is energetically downhill from LH2, centered at 875 nm. LH1 forms an S-shaped dimer held together by the PufX protein. [4] Figure 1.2 shows the crystal structures of LH2 and the LH1-RC-PufX dimer with the experimentally determined inter-complex energy transfer rates. Inter-complex transfer between LH2 complexes occurs in 2.7 ps, LH2 transfers excitations to LH1 in 4.8 ps, inter-complex transfer between LH1 complexes occurs in 4.7 ps, and energy transfer from LH1 to the reaction center take 49 ps. [5] Energy transfer from LH1 to the RC is slightly uphill from 875 nm to 870 nm, accounting for the slower transfer time between these complexes. These time constants are presented as average rates. Intra-complex energy transfer in LH2 is discussed

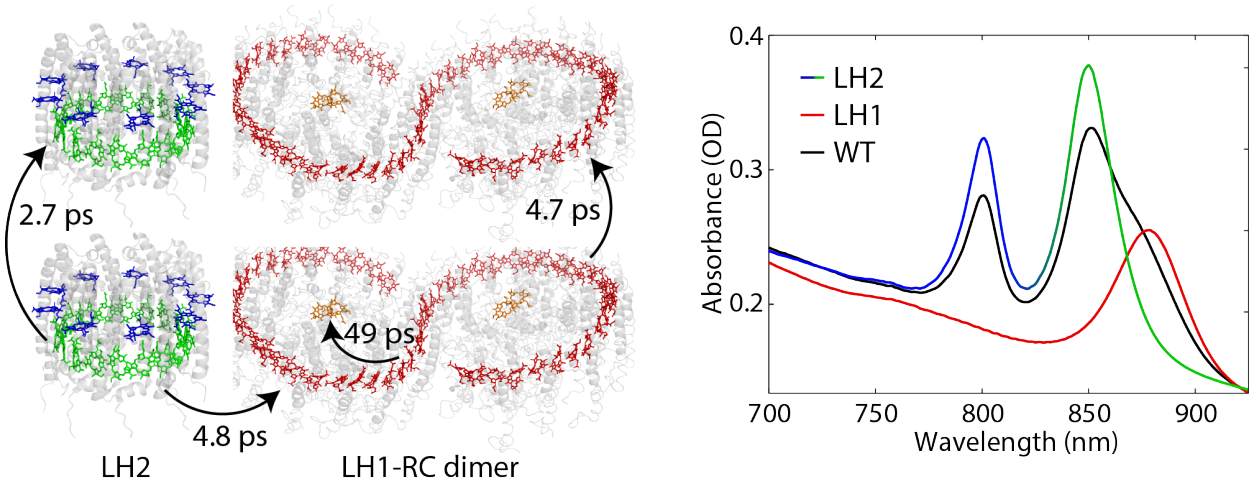

Figure 1.2: (Left) Crystal structures of LH2 (PDB ID: 1KZU [6]) and the LH1-RC-PufX dimer (PDB ID: 4V9G [7]) showing energy transfer rates determined by Dahlberg, et al. [5] The phytyl tails and carotenoids have been removed for visual clarity. (Right) Linear absorption spectra of LH2-only (blue-green), LH1-only (red) and wild-type (black) *Rba. sphaeroides* cells. Figure adapted from Reference [5] under the Creative Commons license https://creativecommons.org/licenses/by/4.0/legalcode.

in Chapters 3 - 5.

Each LH1 monomer encircles an RC which is the site of electron transfer and charge separation. Within an LH1 dimer, the monomeric units are energetically well connected. It has been proposed that the dimeric form with 2 reaction centers might allow excitations to move from one side of the dimer with a closed RC to the other side of the dimer with an open RC to maximize light harvesting. [8]. In the bacterial RC, an excitation starts at the site of the special pair BChl (P band). An electron is transferred via accessory BChl (B band) to the bacteriopheophytin (H band) which in turn is reduced, leaving a hole on the special pair and electron on the bacteriopheophytin. [9] The RC photochemistry initiates downstream processes that lead to the synthesis of adenosine triphosphate (ATP). [1] The experiments presented in this thesis interrogate the initial energy absorption and transfer events in the LH2 complex, though we seek to understand the function of LH2 in the greater context of

the light harvesting process.

1.1.2 Light Harvesting in Cyanobacteria

Cyanobacteria are oxygenic photosynthetic prokaryotes, producing oxygen, ATP, and nicotinamide adenine dinucleotide phosphate (NADPH). [10] Unlike purple bacteria, cyanobacteria produce oxygen gas as a photosynthetic byproduct and contain fused antenna/reaction center photosystems similar to those found in algae and higher plants. [4] These characteristics make them an ideal system in which to study to gain insight about light harvesting in more complex organisms. Figure 1.3 shows an illustrative model of the cyanobacterial photosynthetic apparatus. Phycobilisomes (PBS) act as the primary light-harvesting antennae in cyanobacteria, forming rod-core structures composed of phycobiliproteins (PBP) that sit atop the thylakoid membrane as extrinsic antennae. The rods form a downhill energy gradient from distal to proximal ends, with the highest energy sites of phycoerythrin (absorbance maximum 560 nm) at the distal ends of the rod, phycocyanin (absorbance maximum 620 nm) toward the proximal end of the rod, and the lowest energy sites at the allophycocyanin (APC) core of the PBS. [4, 11] Each PBP is composed of an α/β heterodimer that binds 1-3 bilin pigments. The PBP monomers assemble into ring-shaped trimers which form hexamers. [11] The PBS supercomplex forms from 6-8 rods, each composed of 2-4 hexamers, sitting atop a core of 2-5 cylinders, each composed of 1-2 APC hexamers.

Energy is transferred from the APC core of the PBS to the integral membrane fused antenna/reaction center complexes, Photosystem I (PSI) or Photosystem II (PSII). The crystal structures of PSI and PSII are shown in Figure 1.4. In cyanobacteria, PSI is primarily present in the trimer form and PSII in the dimer form. [14] Each PSI monomer contains 96 chlorophyll (Chl) molecules, and each PSII monomer contains 35 Chl. [10, 11, 13] PSII is the site of the oxygen-evolving complex, oxidizing water to produce molecular oxygen. [4] The ratio of the PSI:PSII varies with illumination intensity between 2:1 and 10:1 in cyanobacteria. [11]

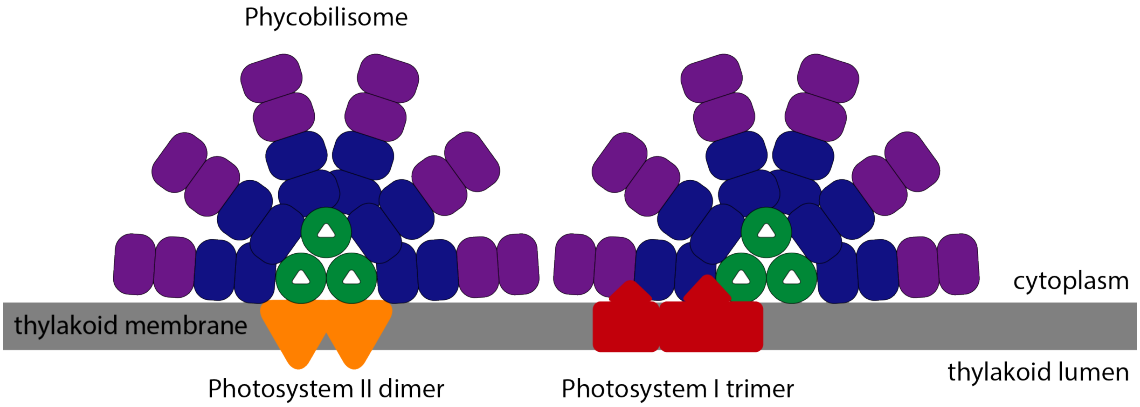

Figure 1.3: Illustration of the cyanobacterial photosynthetic thylakoid membrane. Phycobilisome rods containing phycoerythrin (purple) and phycocyanin (blue) funnel energy down to the allophycocyanin core (green) of the phycobilisome. Energy is then transferred to PSII (orange) or PSI (red) which are fused antenna/reaction center complexes embedded in the thylakoid membrane (gray). Crystal structures of the PSII dimer and PSI trimer are shown in Figure 1.4.

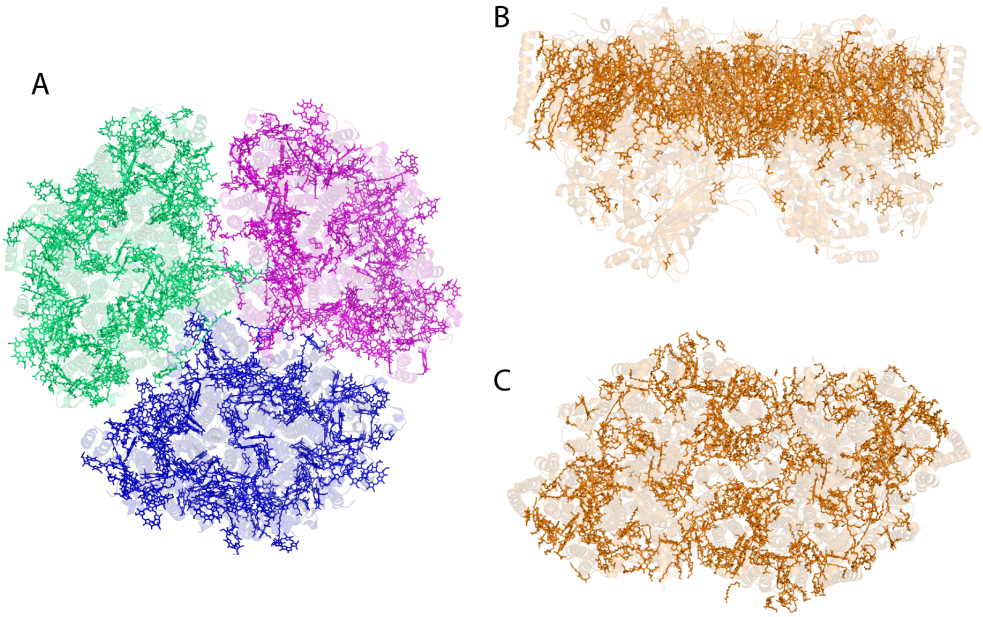

Figure 1.4: (A) Crystal structure of the Photosystem I trimer from *Thermosynechococcus elongatus* (PDB ID: 1JB0 [12]). The 3 PSI monomer units are shown in green, purple, and blue. (B) Side-view and (C) top-view of the crystal structure of the Photosystem II dimer from *Thermosynechococcus vulcanus* (PDB ID: 3WU2 [13]). In the side-view of PSII, the top of the structure is the cytoplasmic side and the bottom of the structure is exposed to the thylakoid lumen. Protein scaffold is shown semi-transparent.

Cyanobacterial photoprotection is regulated by the orange carotenoid protein (OCP) which, when photoactivated, binds to the PBS and quenches excitations. [15] Proposed experiments investigating the OCP nonphotochemical quenching (NPQ) mechanism are the topic of Section 7.2 (Future Directions).

1.2 Theories of Energy Transfer

Different theories have been developed to model energy transfer rates in systems depending on how strongly the system is influenced by the environment and donor-acceptor coupling. The following sections review the weak interchromophore coupling limit described by Förster theory, the strong interchromophore coupling limit described by Redfield theory, and intermediate regimes accounted for by modified Redfield and generalized Förster theories.

1.2.1 Förster Resonance Energy Transfer

The Förster limit dominates excited state energy transfer in the weak interchromophore coupling regime. This model treats the intermolecular interactions perturbatively to describe population transfer from a donor site to an acceptor site. [16, 17]

Fermi's golden rule describes the transitions arising from light-matter interactions, such as absorption and stimulated emission:

$$k_{a\to b} = \frac{2\pi}{\hbar} \mid \langle b \mid U \mid a \rangle \mid^2 \delta(E_b - E_a \pm \hbar\omega) \tag{1.1}$$

Where U is proportional to the interaction potential $-\mu \cdot E$. In the event of absorption, $E_b = E_a + \hbar\omega$, and in the event of stimulated emission, $E_b = E_a - \hbar\omega$. [18]

The rate constant governing energy transfer from donor to acceptor is described by Equation 1.2.

$$k_{DA} = k_f \left(\frac{R_0}{R}\right)^6 \tag{1.2}$$

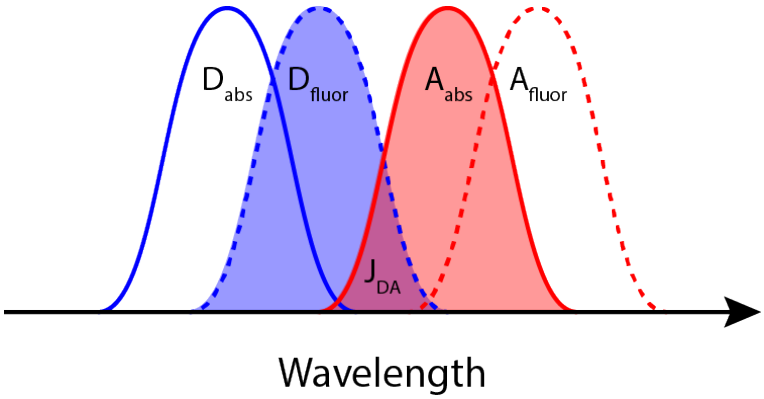

Figure 1.5: Schematic showing the spectral overlap integral J_{DA} (shaded purple) between the donor fluorescence spectrum, D_{fluor} (shaded blue), and acceptor absorbance spectrum, A_{abs} (shaded red), necessary for Förster Resonance Energy Transfer

The first order rate constant, k_{DA} depends on the donor fluorescence rate constant, k_f, the distance at which energy transfer is 50% efficient, R_0, and the distance between donor and acceptor, R. [4] FRET efficiency falls off sharply as distance between donor and acceptor increases due to its $\frac{1}{R^6}$ dependence. R_0 is a function of spectral overlap and orientation between donor and acceptor:

$$R_0^6 = \frac{8.79 \times 10^{-5} J_{DA} \kappa^2}{n^4} \text{Å} \tag{1.3}$$

Where J_{DA} is the spectral overlap integral shown in Figure 1.5 and κ^2 describes the orientation between the donor and acceptor transition dipoles, given by Equation 1.4.

$$\kappa = \cos\alpha - 3\cos\beta_1 \cos\beta_2 \tag{1.4}$$

α gives the angle between the transition dipoles and β_1 and β_2 are the angles between the respective transition dipoles and the radius vector connecting the donor and acceptor. [4, 17] For energy transfer from the B800 ring of LH2 to B850, R_0 is approximately 66 Å. [19]

1.2.2 Redfield Theory

In the opposite limit from FRET, Redfield theory governs energy transfer in the strong interchromophore coupling and weak system-bath interaction regime. This limit leads to a delocalized excitonic state and perturbative treatment of the thermal bath. Redfield theory accounts for all exciton couplings, working in the exciton basis rather than the site basis. [10]

Population transfer in the Redfield limit is described by equation 1.5:

$$k_{D\to A} = \pi J_{DA}[\rho(\omega_{DA})(1 + n(\omega_{DA})) + n(\omega_{AD})\rho(\omega_{AD})] \tag{1.5}$$

The energy transfer rate, $k_{D\to A}$, depends on the spatial overlap of donor and acceptor excitons, J_{DA}, the spectral density at the energy gap between donor and acceptor excitons, $\rho(\omega_{DA})$, and the Bose-Einstein distribution at the energy gap between donor and acceptor excitons, $n(\omega_{DA})$. [20]

1.2.3 Intermediate Regimes of Energy Transfer: Modified Redfield and Generalized Förster Theories

Photosynthetic systems often fall between the limits of standard Redfield or Förster models. Therefore, modified Redfield theory and generalized Förster theories have been developed to more accurately account for the energy transfer rates in these regimes.

Unlike standard Redfield theory, the modified Redfield approach treats part of the exciton-bath interaction non-perturbatively. Modified Redfield theory takes multiphonon processes into account [21] and gives more realistic population relaxation rates and lineshapes, but modified Redfield does not account for one-exciton coherences. [16] The modified Redfield approach is given by Equation 1.6.

$$k_{AADD} = 2\Re \int_0^\infty dt A_A(t) F_D^*(t) V_{AD}(t) \tag{1.6}$$

where $F(t)$ is the donor fluorescence lineshape function (Equation 1.7), $A(t)$ is the acceptor absorption lineshape function (Equation 1.8), and V gives the donor-acceptor interaction (Equation 1.9). [16, 21]

$$F_D(t) = e^{i(\omega-\omega_D)t+2i\lambda_{DDDD}t-g^*_{DDDD}(t)} \tag{1.7}$$

$$A_A(t) = e^{i(\omega-\omega_A)t-g_{AAAA}(t)} \tag{1.8}$$

$$\begin{aligned} V_{AD}(t) =& e^{2g_{DDAA}(t)+2i\lambda_{DDAA}t} \\ & \times [\ddot{g}_{ADDA}(t) - (\dot{g}_{DADD}(t) - \dot{g}_{DAAA}(t) + 2i\lambda_{DADD}) \\ & \times (\dot{g}_{DDAD}(t) - \dot{g}_{AAAD}(t) + 2i\lambda_{DDAD})] \end{aligned} \tag{1.9}$$

For the j^{th} exciton state, g_{jjjj} describes the line-broadening due to exciton-bath coupling and the reorganization energy is given by λ_{jjjj}. Both the line-broadening function and the reorganization energy are functions of the spectral density. [16, 21]

It is assumed that delocalization and the dynamics of localization are dictated by static disorder. The effects of polarons and phonon modes on dynamic localization of excitons are not considered. [16] We use modified Redfield theory for calculations on LH2 in Chapter 3.

In the generalized Förster approach, energy transfer is considered between delocalized clusters of sites, as opposed to between localized chromophores. The clusters are weakly coupled to one another and have small spatial overlap of the donor and acceptor wavefunctions. Generalized Förster theory describes energy transfer from LH2 to LH1 in which LH2 is a delocalized cluster of chromophores which is weakly coupled to LH1, another delocalized cluster of chromophores. Generalized Förster theory is described by Equation 1.10 for energy transfer from a delocalized donor exciton state, D, to a delocalized acceptor exciton state, A.

$$V_{DA} = \left|\sum_{n,m} c_n^D M_{nm} c_m^A\right|^2 \tag{1.10}$$

In Equation 1.10, m and n are chromophores from different clusters and M_{nm} describes the weak inter-cluster interaction. The wavefunction amplitudes c_n^D and c_m^A describe the participation of the n^{th} site in the donor exciton state and the m^{th} site in the acceptor exciton state. [16]

Combined Redfield-Förster approaches use modified Redfield theory to describe energy transfer rates within a strongly coupled cluster of sites and generalized Förster theory to describe inter-cluster energy transfer. [16]

1.3 Two-Dimensional Electronic Spectroscopy Theory

Two-dimensional electronic spectroscopy (2DES) correlates excitation and detection energies as a function of waiting time, T. 2DES provides lineshape information and reveals time-resolved couplings and paths of energy transfer. [22–24] Homogenous broadening, which results from fast interactions with the bath relative to the timescale of the experiment, is distinguishable from heterogenous broadening, which arises from environments that are relatively static on the timescale of the experiment such as disorder caused by slow motions of the protein scaffold. [16, 25] Three time ordered pulses interact with the system: pulses 1 and 2 act as pump pulses and pulse 3 acts as a probe pulse. The first light-matter interaction initiates a coherence between the ground and excited states and the system evolves phase during the coherence time delay, τ, between the first two pulses. Interaction with the second pulse puts the system in a population or zero-quantum coherence during the waiting time, T, between the second pulse and pulse 3. Phase evolves again during the detection time delay, t, following the interaction with pulse 3 until a signal is produced as the final light-matter interaction. [26, 27] The signal is detected by heterodyning with an attenuated local oscillator pulse. [23]

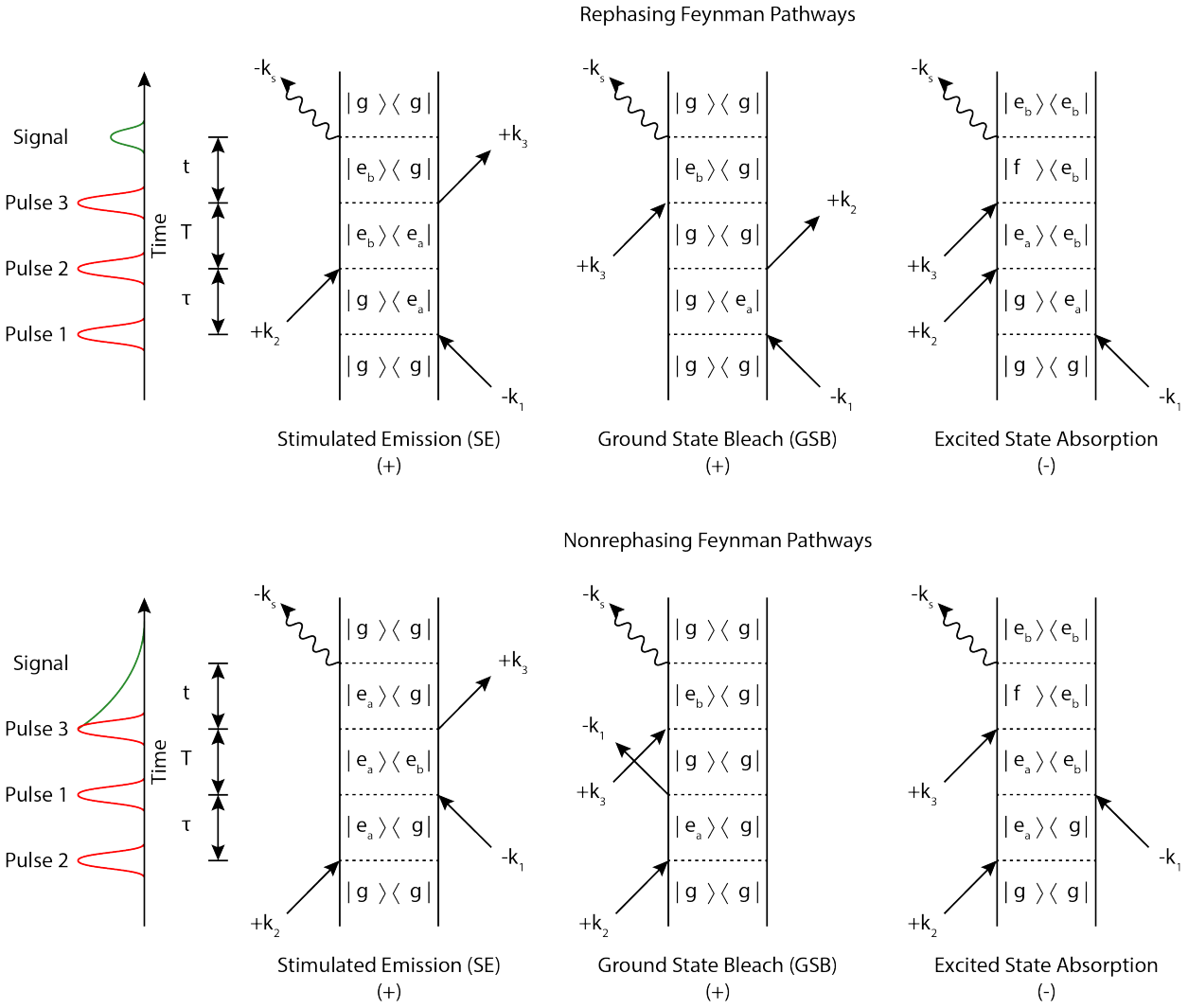

Figure 1.6: Double-sided Feynman diagrams corresponding to (top) rephasing pathways producing a photon echo signal and (bottom) nonrephasing pathways producing a free induction decay signal for (left) stimulated emission, (center) ground state bleach, and (left) excited state absorption. Nonrephasing pathways reverse the time ordering of Pulse 1 and Pulse 2 relative to the rephasing pathways to generate signals in the same phase-matched direction.

Figure 1.6 shows Feynman diagrams of rephasing pathways, in which the phase acquired during the coherence time, τ, is reversed during the detection time delay, t. Figure 1.6 also shows Feynman diagrams of nonrephasing pathways, in which there is not a reversal of phase acquired during τ and t. Stimulated emission, ground state bleach, and excited state absorption signals are interrogated in both rephasing and nonrephasing signals. Rephasing and nonrephasing signals are both detected in the same phase-matched direction of the wavevectors, $k_s = -k_1 + k_2 + k_3$, by reversing the time ordering of pulses 1 and 2. In the nonrephasing pathways, pulse 2 precedes pulse 1 in time. Absorptive spectra contain the real portion of both the rephasing and nonrephasing signals. Dispersive spectra contain the imaginary portions.

Feynman diagrams are diagrammatic representations of the response function. The third-order response function represented by the rephasing stimulated emission Feynman diagram (top left in Figure 1.6) takes the form of:

$$R = p_g \mid \mu_{ge_a} \mid^2 \mid \mu_{ge_b} \mid^2 e^{i\omega_{e_a g}(\tau) - i\omega_{e_b e_a}(T) - i\omega_{e_b g}(t) - \Gamma_{e_a g}(\tau) - \Gamma_{e_a e_b}(T) - \Gamma_{e_b g}(t)} \tag{1.11}$$

where p_g gives the probability of initially occupying the ground state, μ is the transition dipole moment for a light-matter interaction, ω_{eg} is the frequency of the energy gap $\frac{E_e - E_g}{\hbar}$ between two states, and Γ is a damping constant such that $\Gamma_{eg} = \Gamma_{ge}$. [28] For $a = b$, Equation 1.11 reduces to:

$$R = p_g \mid \mu_{ge} \mid^4 e^{i\omega_{eg}(\tau - t) - \Gamma_{eg}(\tau + t) - \Gamma_{ee}(T)} \tag{1.12}$$

For rephasing pathways, the phase acquired during the coherence time, $e^{+i\omega_{eg}\tau}$, is reversed during the detection time (t), $e^{-i\omega_{eg}t}$, generating a photon echo signal. Nonrephasing pathways do not exhibit this time-reversal property and acquire phase in the same direction during coherence time, $e^{-i\omega_{eg}\tau}$, and detection time, $e^{-i\omega_{eg}t}$, resulting in a free induction

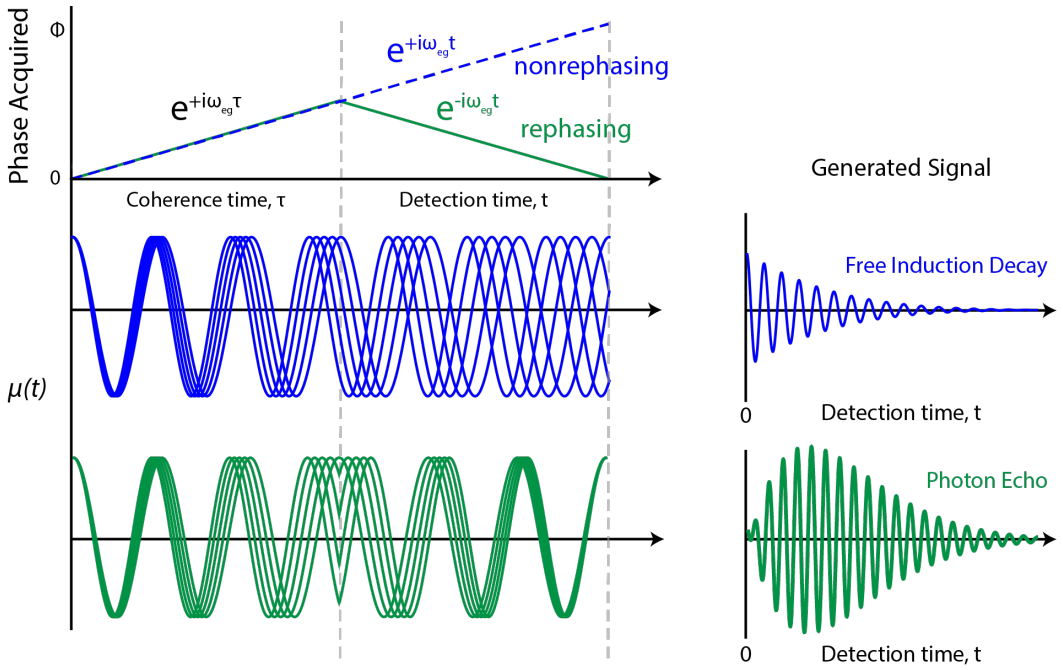

Figure 1.7: Phase acquired during the coherence time is reversed during the detection time for rephasing pathways (green) but not for nonrephasing pathways (blue). The phase reversal of rephasing pathways generates a photon echo signal. Nonrephasing pathways generate a free induction decay signal starting at t = 0 which is weaker than the photon echo. Figure adapted from Reference [28].

decay signal. Figure 1.7 shows the phase acquisition of rephasing and nonrephasing pathways during the coherence time and detection time delays generating photon echo and free induction decay signals, respectively.

A two-dimensional spectrum is a correlation map plotting signal as a function of detection and excitation energies. The excitation energy axis is generated by a Fourier transform over the coherence time delay. The detection energies are directly detected by spectrally resolving the signal using a spectrometer grating. Diagonal features arise from the stimulated emission (SE) and ground state bleach (GSB) Feynman pathways shown in Figure 1.6 in the case of $a = b$. These peaks are related to the linear absorption peaks, but scale nonlinearly as μ^4 instead of μ^2. [23] Crosspeak features arise from the SE and GSB pathways when $a \neq b$, from excited state absorption (ESA), or from pathways with population transfer during the waiting time, such as the SE and ESA rephasing pathways shown in Figure 1.8. SE and

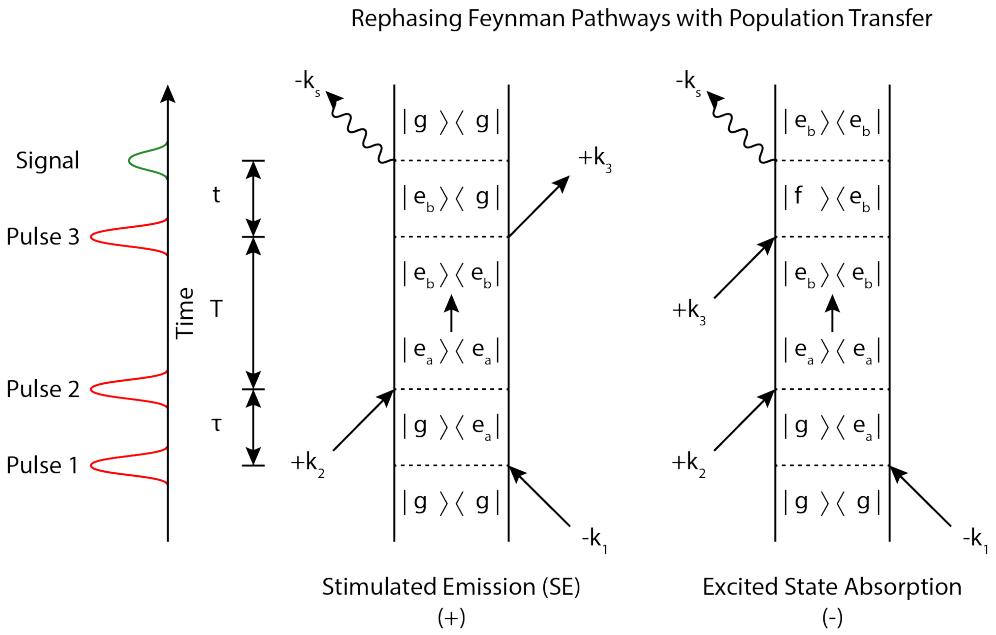

Figure 1.8: Double-sided Feynman diagrams corresponding to rephasing pathways producing a photon echo signal with population transfer during the waiting time for (left) stimulated emission and (right) excited state absorption.

GSB contribute to positive 2DES signals due to stronger signals from emission/bleach while ESA results in negative 2DES signals due to weaker signals from absorption of the incident field. The sign of these signals are a matter of convention and are the opposite sign of these signals typically reported in transient absorption experiments with units of ΔOD. [29]

REFERENCES

[1] D. J. Mothersole, D. A. Farmer, A. Hitchcock, and C. N. Hunter. Photosynthetic apparatus in purple bacteria. In R. Croce, R. van Grondelle, H. van Amerongen, and I. H. van Stokkum, editors, *Light Harvesting in Photosynthesis*, book section 6. CRC Press, Boca Raton, FL, 2018.

[2] M. K. Sener, J. D. Olsen, C. N. Hunter, and K. Schulten. Atomic-level structural and functional model of a bacterial photosynthetic membrane vesicle. *Proc. Natl. Acad. Sci. USA*, 104(40):15723–15728, 2007.

[3] M. Z. Papiz, S. M. Prince, T. Howard, R. J. Cogdell, and N. W. Isaacs. The structure and thermal motion of the B800–850 LH2 complex from *Rps. acidophila* at 2.0Å resolution and 100K: New structural features and functionally relevant motions. *J. Mol. Biol.*, 326:1523–1538, 2003.

[4] R. E. Blankenship. *Molecular Mechanisms of Photosynthesis*. John Wiley & Sons, Ltd, Chichester, West Sussex, 2nd edition, 2014.

[5] P. D. Dahlberg, P.-C. Ting, S. C. Massey, M. A. Allodi, E. C. Martin, C. N. Hunter, and G. S. Engel. Mapping the ultrafast flow of harvested solar energy in living photosynthetic cells. *Nat. Commun.*, 8:988–994, 2017.

[6] S. M. Prince, M. Z. Papiz, A. A. Freer, G. McDermott, A. M. Hawthornthwaite-Lawless, R. J. Cogdell, and N. W. Isaacs. Apoprotein structure in the LH2 complex from *Rhodopseudomonas acidophila* strain 10050: Modular assembly and protein pigment interactions. *J. Mol. Biol.*, 268:412–423, 1997.

[7] P. Qian, M. Z. Papiz, P. J. Jackson, A. A. Brindley, I. W. Ng, J. D. Olsen, M. J. Dickman, P. A. Bullough, and C. N. Hunter. Three-dimensional structure of the *Rhodobacter sphaeroides* RC-LH1-PufX complex: dimerization and quinone channels promoted by PufX. *Biochemistry*, 52(43):7575–7585, 2013.

[8] M. Sener, J. Hsin, L. G. Trabuco, E. Villa, P. Qian, C. N. Hunter, and K. Schulten. Structural model and excitonic properties of the dimeric RC-LH1-PufX complex from *Rhodobacter sphaeroides*. *Chem. Phys.*, 357(1-3):188–197, 2009.

[9] J.-L. Martin, J. Breton, A. J. Hoff, A. Migus, and A. Antonetti. Femtosecond spectroscopy of electron transfer in the reaction center of the photosynthetic bacterium *Rhodopseudomonas sphaeroides* R-26: Direct electron transfer from the dimeric bacteriochlorophyll primary donor to the bacteriopheophytin acceptor with a time constant of 2.8 $\pm$ 0.2 psec. *Proc. Natl. Acad. Sci. USA*, 83:957–961, 1986.

[10] M. Sener, J. Strumpfer, J. Hsin, D. Chandler, S. Scheuring, C. N. Hunter, and K. Schulten. Forster energy transfer theory as reflected in the structures of photosynthetic light-harvesting systems. *Chem. Phys. Chem.*, 12:518–531, 2011.

[11] L. Bar-Eyal, A. Shperberg-Avni, Y. Paltiel, N. Keren, and N. Adir. Light harvesting in cyanobacteria: The phycobilisomes. In R. Croce, R. van Grondelle, H. van Amerongen, and I. H. van Stokkum, editors, *Light Harvesting in Photosynthesis*, book section 5. CRC Press, Boca Raton, FL, 2018.

[12] P. Jordan, P. Fromme, H. T. Witt, O. Klukas, W. Saenger, and N. Krauss. Three-dimensional structure of cyanobacterial photosystem I at 2.5 Å resolution. *Nature*, 411:909–917, 2001.

[13] Y. Umena, K. Kawakami, J. R. Shen, and N. Kamiya. Crystal structure of oxygen-evolving photosystem II at a resolution of 1.9 Å. *Nature*, 473(7345):55–60, 2011.

[14] C. MacGregor-Chatwin, M. Sener, S. F. H. Barnett, A. Hitchcock, M. C. Barnhart-Dailey, K. Maghlaoui, J. Barber, J. A. Timlin, K. Schulten, and C. N. Hunter. Lateral segregation of photosystem I in cyanobacterial thylakoids. *Plant Cell*, 29(5):1119–1136, 2017.

[15] A. Pinnola, D. Kirilovsky, and R. Bassi. Photoprotective excess energy dissipation. In R. Croce, R. van Grondelle, H. van Amerongen, and I. H. van Stokkum, editors, *Light Harvesting in Photosynthesis*, book section 11. CRC Press, Boca Raton, FL, 2018.

[16] V. Novoderezhkin and R. van Grondelle. Physical origins and models of energy transfer in photosynthetic light harvesting. *Phys. Chem. Chem. Phys.*, 12:7352–7365, 2010.

[17] L. Valkunas, J. Chmeliov, and H. van Amerongen. The exciton concept. In R. Croce, R. van Grondelle, H. van Amerongen, and I. H. van Stokkum, editors, *Light Harvesting in Photosynthesis*, book section 12. CRC Press, Boca Raton, FL, 2018.

[18] G. C. Schatz and M. A. Ratner. *Quantum Mechanics in Chemistry*. Dover Publications, Inc., Mineola, NY, 2002.

[19] R. van Grondelle. Excitation energy transfer, trapping and annihilation in photosynthetic systems. *Biochim. Biophys. Acta*, 811:147–195, 1985.

[20] A. F. Fidler. *Monitoring Ultrafast Evolution of Electronic Structure Within Photosynthetic Antenna Complexes Using Multidimensional Spectroscopies*. Thesis, University of Chicago, 2013.

[21] M. Yang and G. R. Fleming. Influence of phonons on exciton transfer dynamics: comparison of the Redfield, Forster, and modified Redfield equations. *Chem. Phys.*, 282:163–180, 2002.

[22] M. Cho, T. Brixner, I. Stiopkin, H. Vaswani, and G. R. Fleming. Two dimensional electronic spectroscopy of molecular complexes. *J. Chin. Chem. Soc.*, 53:15–24, 2006.

[23] T. Brixner, T. Mancal, I. V. Stiopkin, and G. R. Fleming. Phase-stabilized two-dimensional electronic spectroscopy. *J. Chem. Phys.*, 121:4221–4236, 2004.

[24] T. Brixner, J. Stenger, H. M. Vaswani, M. Cho, R. E. Blankenship, and G. R. Fleming. Two-dimensional spectroscopy of electronic couplings in photosynthesis. *Nature*, 434:625–628, 2005.

[25] S. Mukamel. *Principles of Nonlinear Optical Spectroscopy*. Oxford University Press: New York, Oxford, 1995.

[26] Y. C. Cheng, G. S. Engel, and G. R. Fleming. Elucidation of population and coherence dynamics using cross-peaks in two-dimensional electronic spectroscopy. *Chem. Phys.*, 341(1-3):285–295, 2007.

[27] E. Harel, A. F. Fidler, and G. S. Engel. Single-shot gradient-assisted photon echo electronic spectroscopy. *J. Phys. Chem. A*, 115:3787–3796, 2011.

[28] A. Tokmakoff. Nonlinear spectroscopy. http://tdqms.uchicago.edu/page/nonlinear-and-two-dimensional-spectroscopy-notes, 2011.

[29] R. Berera, R. van Grondelle, and J. T. Kennis. Ultrafast transient absorption spectroscopy: Principles and application to photosynthetic systems. *Photosynth. Res.*, 101(2-3):105–118, 2009.

CHAPTER 2

EXPERIMENTAL METHODS AND INSTRUMENTATION

2.1 Spectroscopic Methods

We use a Coherent Micra oscillator with 60-70 nm bandwidth centered around 800 nm at 300-350 μW output to seed a Coherent Legend Elite regenerative amplifier that is pumped by a Coherent Evolution. The 80 MHz oscillator output is downselected to 5 kHz and amplified to a regen output power of 2.0 - 2.4 W by chirped pulse amplification. The regen beam is focused through a 2 m tube of Argon gas held at 15 psi above atmospheric pressure, compressed with 6 bounces off of a chirped mirror pair (Layertec, -40 fs^2 group delay dispersion), and then refocused through the Argon tube again to achieve spectral broadening. The beam is collimated, compressed with 6 additional bounces off a duplicate chirped mirror pair, and then amplitude shaped and compressed with a Spatial Light Modulator (SLM)-based Multiphoton Intrapulse Interference Phase Scan (MIIPS) compressor (Biophotonics, Inc). If a bluer spectrum is desired ($<$ 750 nm), a short-pass filter is introduced into the beam path prior to the MIIPS.

The beam is split by a 50/50 beamsplitter into two separate beams, referred to as beam 1/2 and beam 3/4. Beam 1/2 travels over a motorized Aerotech delay stage which is used to control the waiting time delay. Beam 1/2 is also focused through an optical chopper which is used for scatter removal during data acquisition. Both beams are then directed into the 2D instrument.

2.1.1 GRAPES Instrumentation

All of the 2DES data presented in this thesis were collected using GRadient Assisted Photon Echo Spectroscopy (GRAPES) which uses geometrically tilted pulses to spatially encode the coherence time delay. [1] Figure 2.1 shows the beam paths through the GRAPE instrument. Beam 1/2 passes through an angled 1 mm piece of compensating glass to match the

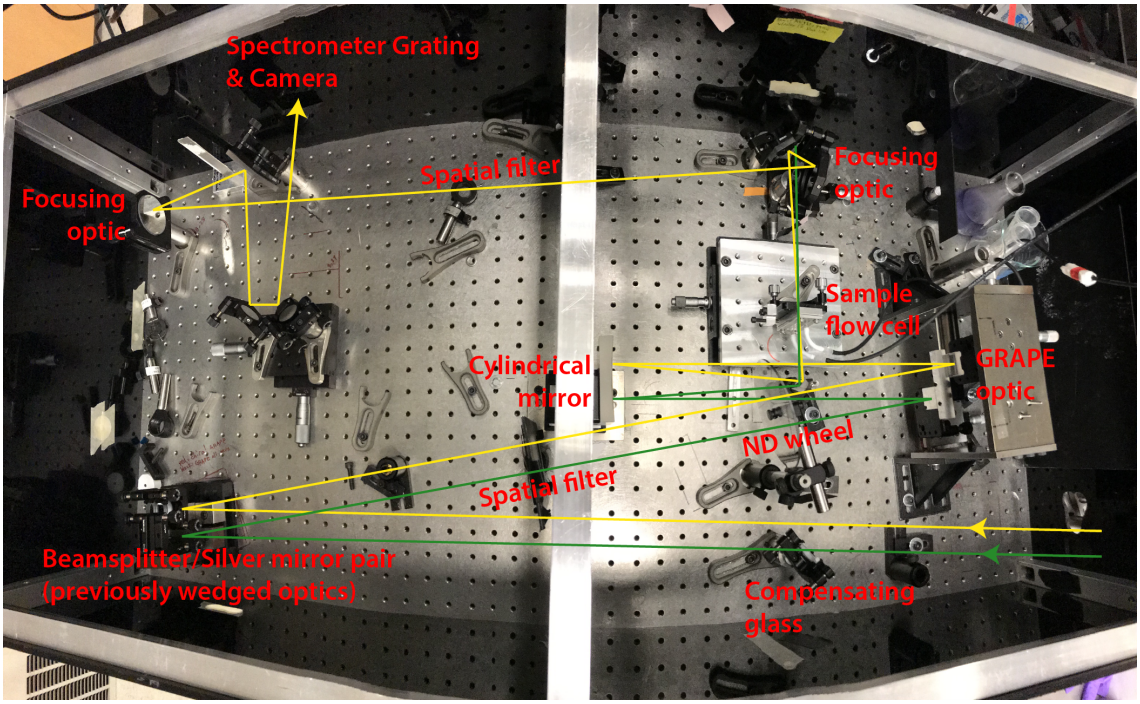

Figure 2.1: Photograph of the GRAPES instrument. The path of beam 1 is shown in green and the path of beam 4 is shown in yellow, propagating all the way into the spectrometer slit. Arrows indicate the direction of propagation.

compression to beam 3/4 which previously passed through a beamsplitter. Beam 1/2 is then split into beam 1 and beam 2 and beam 3/4 is split into beam 3 and beam 4 using a beamsplitter/silver mirror pair. Beams 1 and 4 are reflections off of the back surface of the beamsplitter and beams 2 and 3 pass through the beamsplitter, reflect off of the silver mirror, and then pass back through the beamsplitter. Each beam passes through the same amount of glass in the beamsplitter to retain compression of the pulses. Higher order reflections are blocked by a spatial filter. After the spatial filter, beam 4 passes through a neutral density wheel so that it can be attenuated as needed for each experiment. All four beams then reflect off of the GRAPE optic, shown in Figure 2.2, producing a distorted BoxCARS geometry.

On the GRAPE optic, beams 1 and 4 reflect off angled optics to impart a spatial geometric tilt over the height of the beam. The tilt is equal and opposite for the two beams. Beam 4 is attenuated by taking a Fresnel reflection off a glass optic to be used as the local oscillator for

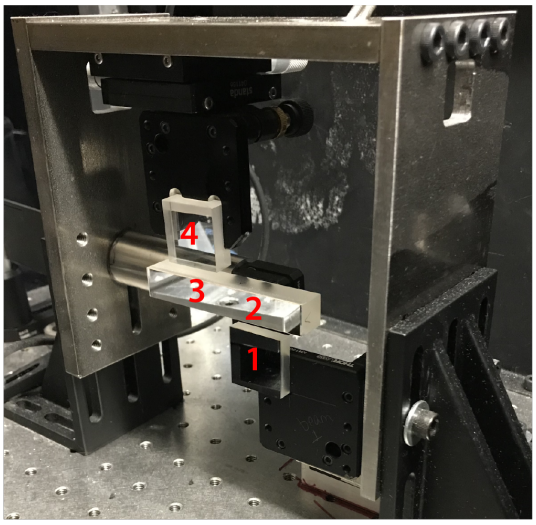

Figure 2.2: Photograph of the GRAPE optic. Beams 2 and 3 reflect off of the same 3" × 0.5" silver mirror and travel parallel to the laser table from the GRAPE optic to the cylindrical mirror. Beam 1 reflects off the lower angled silver mirror and is steered upward so that it overlaps in the vertical with beams 2 and 3 at the sample position. Beam 4 is a Fresnel reflection off of the upper angled optic and is steered downward so that it overlaps in the vertical with beams 1, 2, and 3 at the sample position.

heterodyne detection. All four beams are focused to overlap as a vertical line at the sample by a cylindrical mirror (Lattice Optics, f = 250 mm) so that they focus only in the horizontal dimension. Due to the geometric tilt between beam 1 and beam 2, there is a variable time delay between the two pulses over the height of the beam with a crossing point near the middle of the vertical dimension. This variable time delay is the spatial encoding of the coherence time delay. The sample flow cell can be mounted either parallel or perpendicular to the beam height. A perpendicular mount allows sample to flow across the beam waist, minimizing repeat laser exposure of any given chromophore. The flow cell tubing is directed through a peristaltic pump so that liquid samples can be continuously flowed through the cell from a larger sample reservoir during an experiment.

The phase-matched 2D signal ($k_s = -k_1 + k_2 + k_3$) co-propagates with the local oscillator from the sample into the camera, passing through a spatial filter to block beams 1, 2, and 3 and to minimize scatter. The signal is frequency resolved by an Andor Shamrock spectrometer and then heterodyne detected on an Andor Neo 5.5 sCMOS 2D array camera.

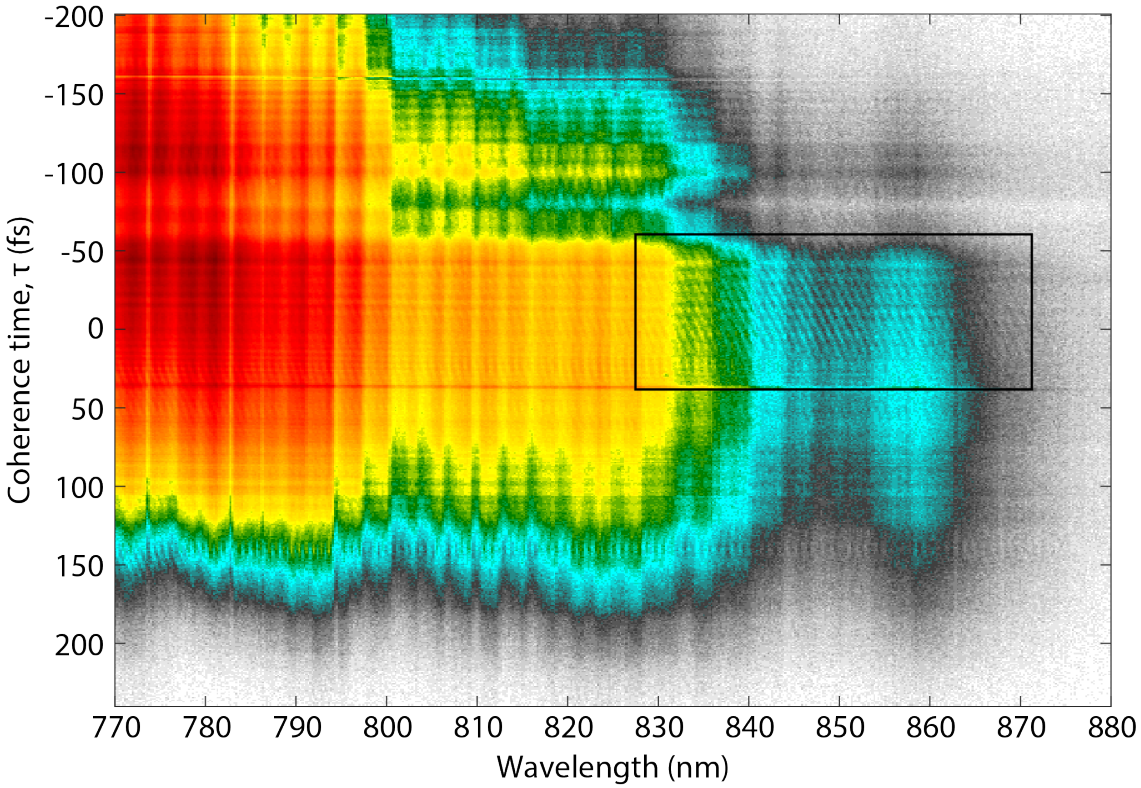

Figure 2.3: Raw 2D camera image of heterodyned signal from LH2-only membranes collected on the Phantom Miro M310 CMOS camera. Detection wavelength is resolved along the x axis and coherence time, τ is recorded along the y axis. In this experiment, the τ gradient was 0.875 fs/pixel, giving a coherence time range of -201 - 239 fs over the range of 504 pixels. Most of the light on the camera is the LO that transmitted through the sample. The weak diagonal interferogram of the heterodyned B850 signal is visible within the black box. The signal intensity is maximal around the τ=0 line of pixels. The B800 heterodyned signal is too weak to distinguish by eye in this image.

Earlier datasets were collected on a Phantom Miro M310 CMOS 2D array camera, shown in Figure 2.3. The x dimension of the camera corresponds to detection energy resolved in wavelength, and the y dimension corresponds to coherence time.

We use a divide-by circuit to down-select the TTL signal from the regen output to sync to the optical chopper and camera in order to average over many laser shots in a single camera frame. In the absence of the circuit, the 5 kHz regen output signal is used to trigger the optical chopper at a frequency of 2.5 kHz and the camera at a frequency of 5 kHz. Each camera frame would alternate between collecting heterodyned signal with beams 1, 2, 3, and 4 coincident on the sample or heterodyned scatter from beams 3 and 4. Because beam 3

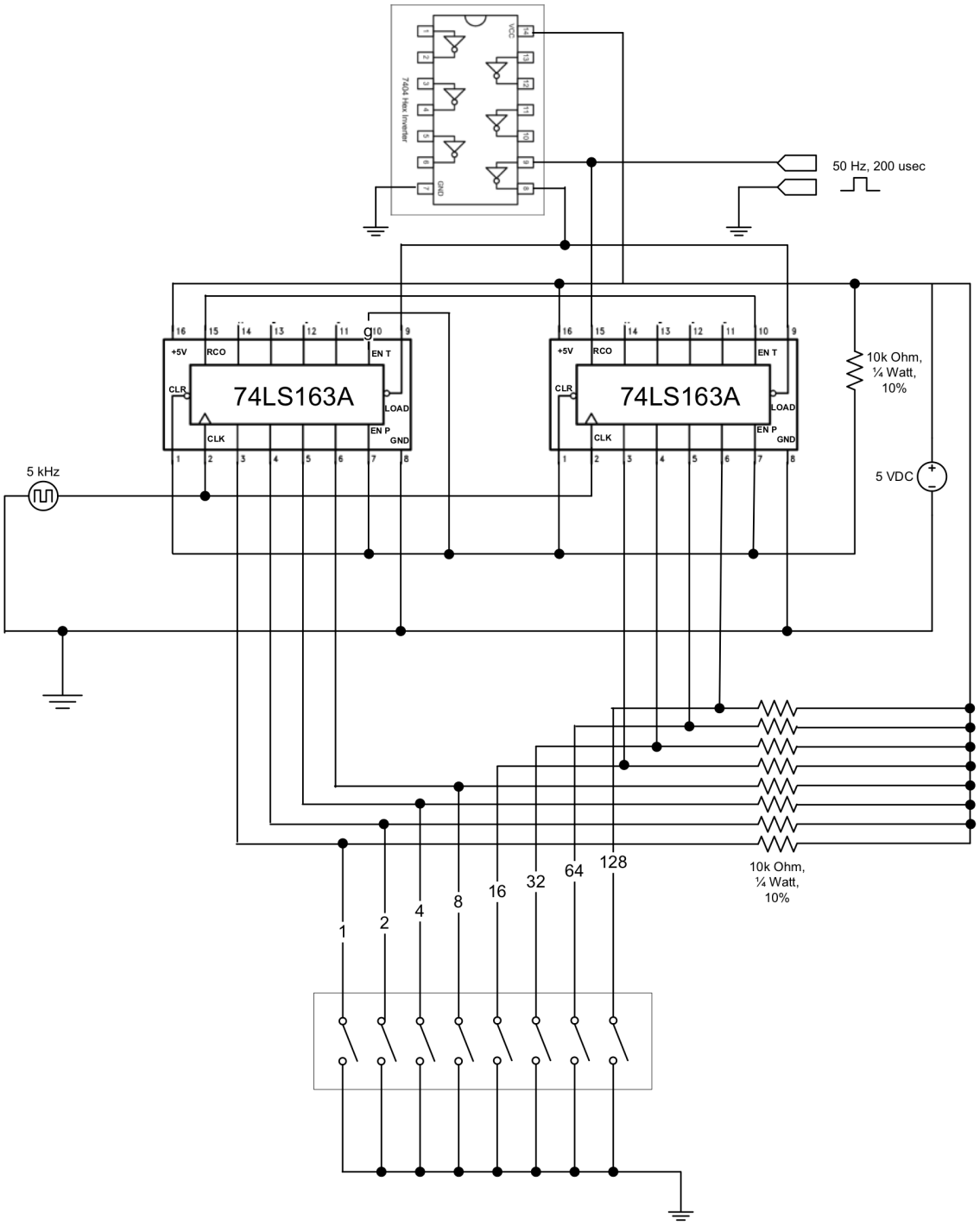

Figure 2.4: Schematic of a divide-by circuit, designed by James Chamberlin, to average over many laser shots in a single camera frame. The circuit takes the regen TTL signal and divides it as programmed by the binary dip switch to send an input to the chopper and camera.

propagates most closely to beam 3 and the signal, most of the detected scatter contributions are due to scatter from beam 3. By chopping and subtracting consecutive camera frames which correspond to consecutive laser shots, we subtract off the beam 3 scatter. With the circuit in place, the 5 kHz regen output signal is downselected to a selected frequency, such as 50 Hz. In this case, the circuit outputs a 50 Hz signal that is used to trigger the optical chopper at 25 Hz and the camera at 50 Hz. Each camera frame alternates between averaging over 100 laser shots of heterodyned signal and 100 laser shots of beams 3-4 scatter. This averaging scheme serves to average out dynamic scatter that changes phase between laser shots. [2] Consecutive camera frames are subtracted to remove beam 3 scatter. The original schematic for this circuit, designed by James Chamberlin, is shown in Figure 2.4. The current circuit in use is based off of this plan, but incorporates 2 dip switches to enable more flexibility in selecting the number of averaged laser shots and the camera frame collection frequency.

2.1.2 GRAPES Data Processing

This section discusses recent improvements to the processing of GRAPES data. A thorough discussion of the full GRAPES processing can be found in Reference [2]. GRAPES was previously limited to collecting and producing only rephasing spectra without reconfiguring the spectrometer to change the phase-matched direction. A range of negative and positive coherence times was collected, but the negative coherence time portion of the dataset did not correspond to a single waiting time for a given camera frame. This misordering results because beam 1 is tilted relative to beams 2 and 3 as shown in Figure 2.5. At negative coherence times, beam 1 serves as the second interaction following beam 2. Therefore, waiting time is the time delay between beam 1 and beam 3, resulting in a variable waiting time over the range of negative coherence times. In the τ versus t domain, we applied a window in τ over positive coherence times (rephasing signal) with a steep window cutting off the signal close to the $\tau = 0$ line of pixels.

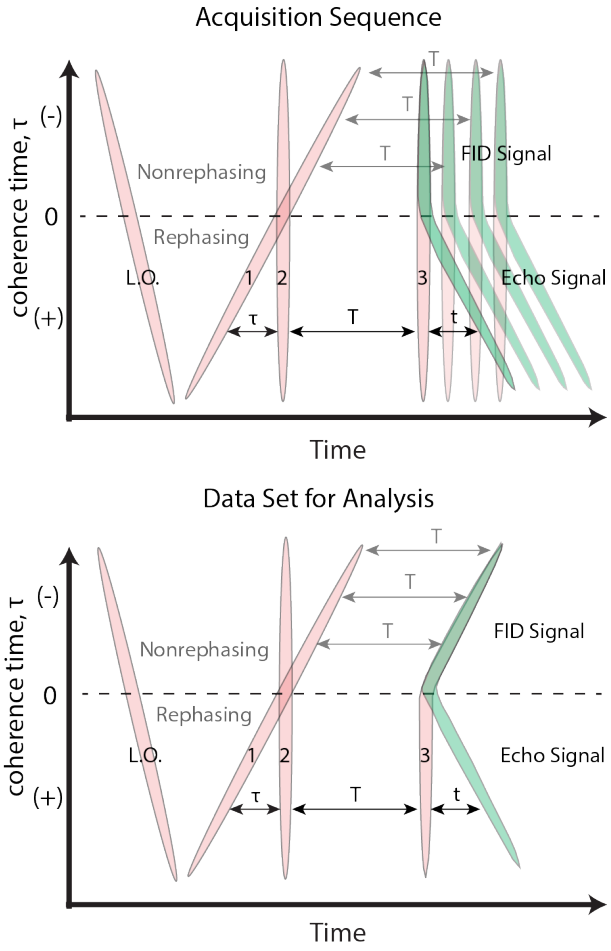

Figure 2.5: (top) The GRAPES acquisition pulse sequence for generating absorptive 2D spectra. Both rephasing photon echo signals [(+) τ] and nonrephasing free induction decay signals [(-) τ] are produced in the same phase-matched direction. (bottom) Reconstructed dataset for analysis by which the nonrephasing portion of the data has been reconstructed for a single constant waiting time, T. Reprinted from Reference [3], with the permission of AIP Publishing.

We recently introduced a data restructuring method to recover both rephasing and nonrephasing signals. [3] In the original implementation of this method, as presented in Reference [3], a single dataset was processed entirely as a rephasing dataset with no restructuring. In the τ versus t domain, a log curve window was applied in τ to window over the positive coherence times, although a small amount of negative coherence times (nonrephasing signals that had not been properly restructured) would be included. This analysis would produce a rephasing 2D spectrum. The entire raw dataset was then reprocessed with restructuring to correct the nonrephasing portion of the data. A similar window was applied in the coherence time versus detection time (τ versus t) domain to window over the negative coherence times, although a small amount of positive coherence times (rephasing signals that had been improperly restructured) would be included. The resulting nonrephasing and rephasing 2D spectra were phased separately by fitting to pump probe data, and then summed to produce an absorptive 2D spectrum. This process is illustrated in Figure 2.6.

The improvements to the data processing scheme (Figure 2.7) that I developed include a separation of the raw dataset into two distinct cubes, rephasing + $\tau = 0$ ($\tau \geq 0$) and nonrephasing ($\tau < 0$), and then restructuring only the nonrephasing portion of the dataset. After windowing in waiting time, T, the nonrephasing and rephasing cubes will have the same T spacing, although the nonrephasing cube will have fewer T values due to the restructuring. The rephasing cube is then truncated in waiting time to the length of the nonrephasing cube and the cubes are recombined into a single dataset in which each frame contains nonrephasing and rephasing signals for a given constant waiting time, T. In the coherence time versus detection time domain, a single wide log curve window is applied over τ to include both the rephasing and nonrephasing signals and then a Fourier transform over τ and t yields a single cube of data that can be phased to produce absorptive and dispersive 2D spectra. This revised data processing scheme was used to process fully absorptive spectra for Reference [5].

To determine the absolute phase of 2D spectra and separate absorptive and dispersive components, we fit a projection of the 2D spectrum across the excitation wavelength axis

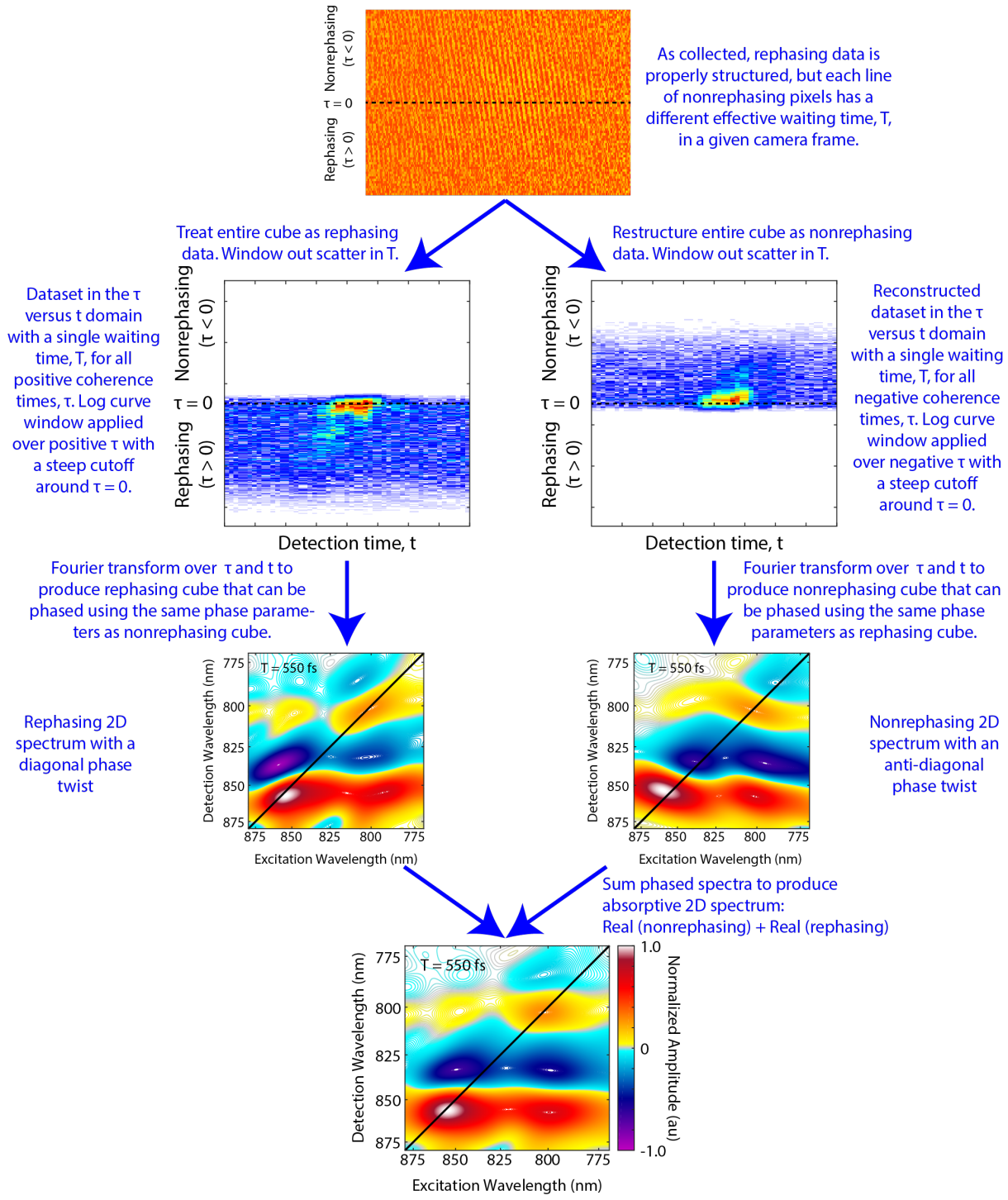

Figure 2.6: Schematic illustrating the original data processing of absorptive 2DES data from GRAPES. A complete dataset (top) is processed twice: once as a rephasing cube (left) and once as a nonrephasing cube (right) which is restructured. A τ window is applied over either positive (rephasing) or negative (nonrephasing) coherence times to produce rephasing and nonrephasing datasets which are phased by fitting to pump-probe using the same set of fit parameters. The real portions of the phased spectra are summed to generate a fully absorptive 2D spectrum (bottom).

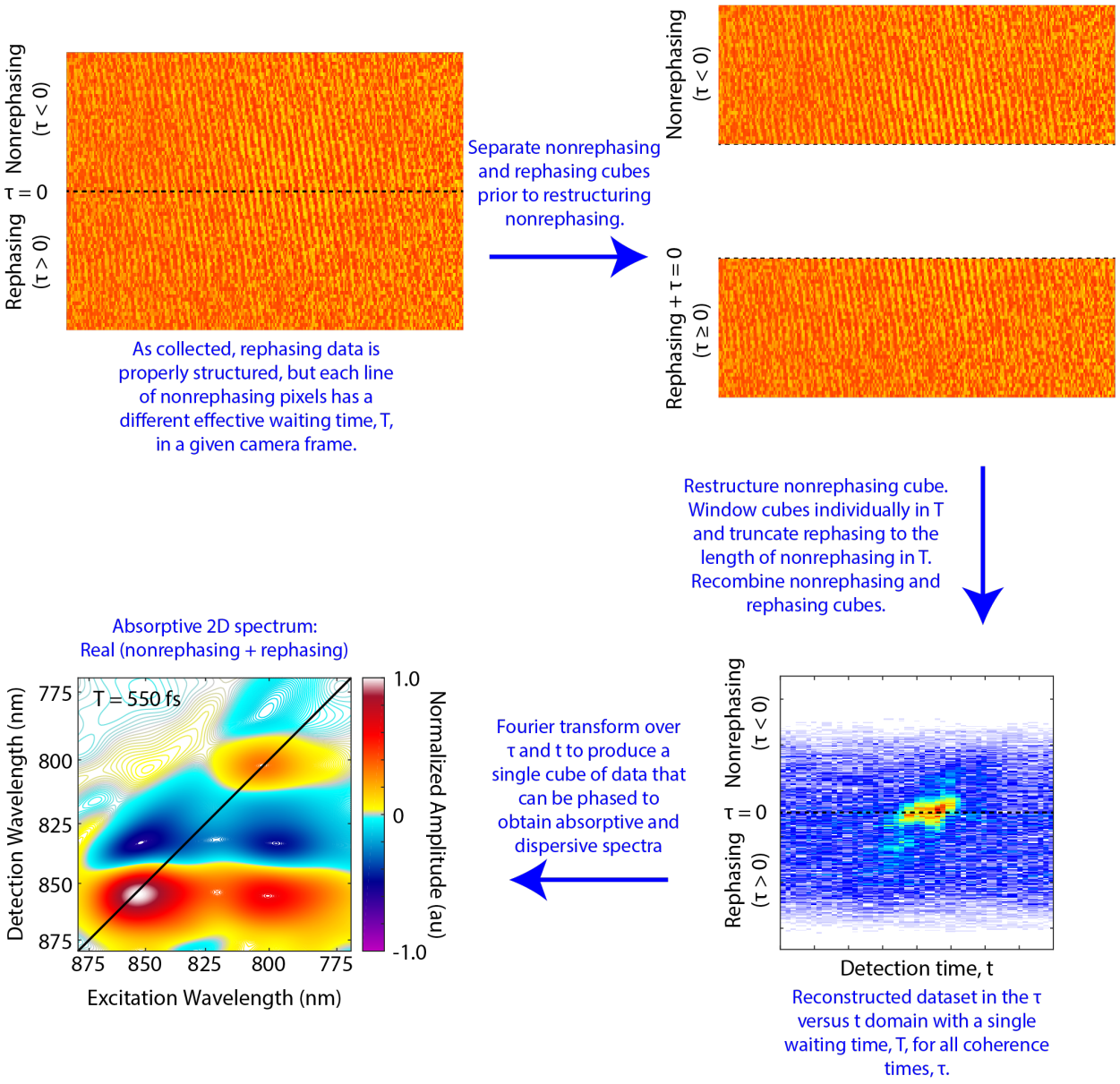

Figure 2.7: Schematic illustrating the revised data processing of absorptive 2DES data from GRAPES. Starting at the top left and proceeding clockwise, a complete dataset (top left) is separated into nonrephasing and rephasing cubes (top right). The nonrephasing cube is restructured for analysis so that the data is reconstructed for a single constant T. After windowing in T, the nonrephasing and rephasing cubes are recombined (bottom right) with a single waiting time for all coherence times. A single τ window is applied to produce a single processed dataset that can be phased to generate a fully absorptive 2D spectrum (bottom left).

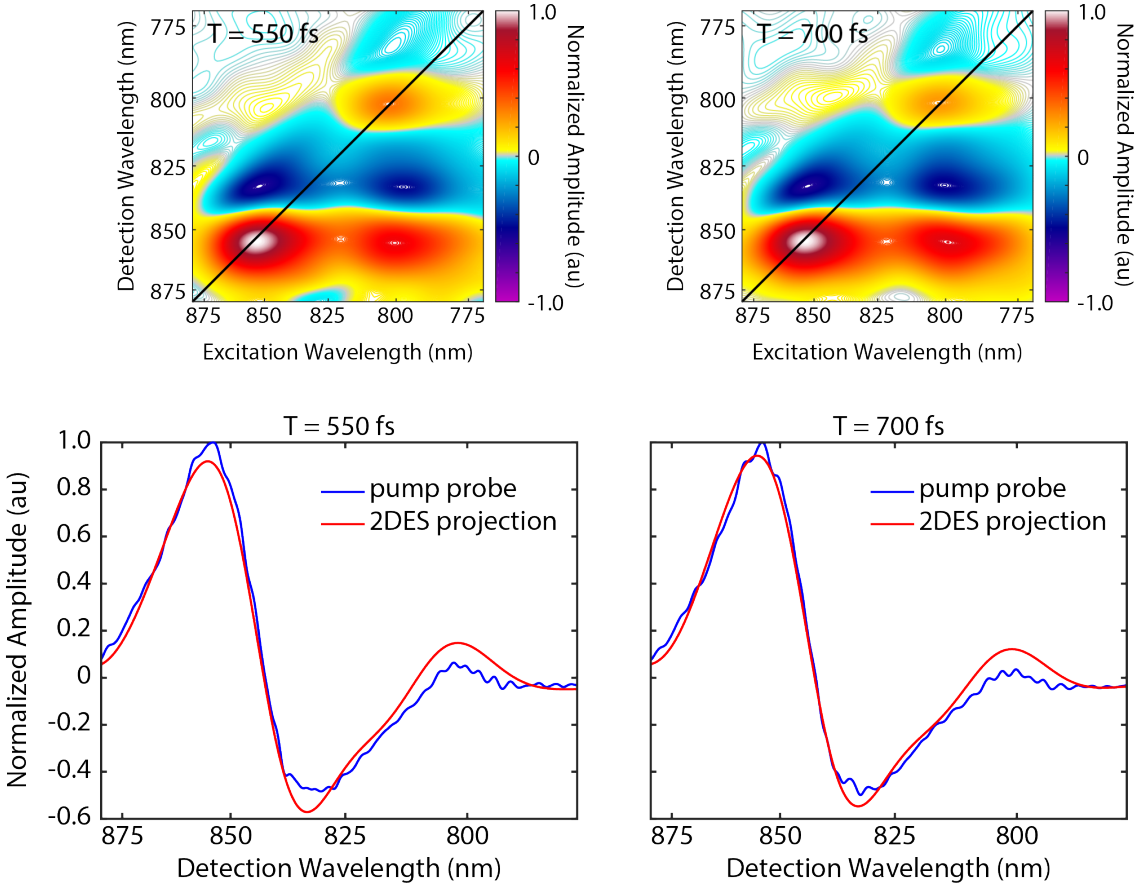

Figure 2.8: (top) Absorptive 2D spectra of LH2-only membranes at waiting times of 550 fs and 700 fs after applying phase parameters determined by fitting to separately acquired pump-probe by the projection slice theorem, following the convention of Brixner et al. [4] (bottom) Fits of a separately acquired pump probe spectrum (blue) to a projection of the 2D spectrum over the excitation wavelength axis (red) at the same waiting times of 550 fs and 700 fs.

to a separately acquired pump probe spectrum at the same waiting time, T, according to the projection slice theorem. [4] Rephasing and nonrephasing 2D spectra can be phased separately. or the summed rephasing and nonrephasing dataset can be phased together if the dataset was processed all together with a single Fourier transform over negative and positive coherence times. [6] Figure 2.8 shows the fit of LH2-only membranes data to the pump probe using the same phase parameters at two different waiting times. The same set of phase parameters was applied to all waiting times in the experiment.

2.2 Cell Culture and Sample Preparation Procedures

2.2.1 Cyanobacterial Cell Culture

Cultures of *Synechocystis* sp PCC 6803 were grown in BG-11 media. [7] A concentrated media stock was purchased from Sigma-Aldrich, but can also be prepared according to the recipe below. If using the recipe below, each stock solution should be passed through a 0.2 μm filter. These recipes were provided by Dr. Andrew Hitchcock from Prof. Neil Hunter's group at the University of Sheffield.

Autoclave commercially purchased BG-11 media, or that prepared according to Table 2.5. Add 1 M TES/KOH to a final concentration of 10 mM. If desired, add 1 M glucose to a final concentration of 5 mM. Glucose is needed for PSI-minus and PSII-minus mutant strains of *Synechocystis* sp, although the addition of glucose does make the culture more susceptible to contamination. Additionally, the PSI-minus strain must be grown under low light, $< 5\ \frac{\mu M}{m^2 s}$.

per 1 L of solution	
Boric acid	2.86 g
Manganese chloride	1.81 g
Zinc sulfate	0.22 g
Sodium molybdate	0.39 g
Copper sulfate	0.079 g
Cobaltous nitrate	0.049 g

Table 2.1: Trace minerals stock solution for BG-11 media

per 1 L of solution	
Sodium nitrate	149.6 g
Magnesium sulfate	7.49 g
Calcium chloride	3.60 g
Citric acid	0.60 g
EDTA (disodium salt)	0.10 g (0.56 mL of 0.5 M stock, pH 8.0)
Trace minerals stock (Table 2.1)	100 mL

Table 2.2: 100x BG-11 stock for BG-11 media

per 1 L of stock solution		
1000x Iron stock	Ferric ammonium citrate	6.0 g
1000x Phosphate stock	Dipotassium hydrophosphate	30.5 g
1000x Carbonate stock	Sodium carbonate	20.0 g

Table 2.3: Additional 1000x stock solutions for BG-11 media. Prepare each stock as a separate solution.

per 1 L of stock solution	
1 M Glucose stock	180.0 g
1 M TES/KOH	TES 229.2 g, adjust to pH 8.2 with KOH

Table 2.4: Supplementary stocks for BG-11 media. Prepare each stock as a separate solution. These solutions are also needed if preparing media from a commercially purchased BG-11 stock.

per 1 L of media	
100x BG-11 stock (Table 2.2)	10.0 mL
1000x Iron stock (Table 2.3)	1.0 mL
1000x Phosphate stock (Table 2.3)	1.0 mL
1000x Carbonate stock (Table 2.3)	1.0 mL

Table 2.5: BG-11 Liquid media

BG-11 agar plates can also be prepared from the stock solutions to streak cells according to Table 2.6 and then autoclaving. After melting, add 1 M TES/KOH to a final concentration

per 1 L of agar media	
100x BG-11 stock (Table 2.2)	10.0 mL
1000x Iron stock (Table 2.3)	1.0 mL
1000x Phosphate stock (Table 2.3)	1.0 mL
1000x Carbonate stock (Table 2.3)	1.0 mL
Bacto-agar	15.0 g
0.3% Sodium thiosulfate	3.0 g

Table 2.6: BG-11 Agar

of 10 mM and, if desired, 1 M glucose to a final concentration of 5 mM. Pour into petri dish plates and allow to cool and solidify before streaking cells onto the plate. Antibiotics are typically only added for growth on plates, not in liquid media. The PSII-minus mutant (ΔpsbB) is resistant to zeocin (20 μg/mL), the attenuated phycobilisome strain (ΔcpcBAC2C1) containing only the allophycocyanin core and no phycocyanin rods is resistant to erythromycin (50 μg/mL).

2.2.2 Cyanobacterial Membrane Preparation

The following procedure is based on recommendations from Dr. Andrew Hitchcock and Dr. Craig MacGregor-Chatwin from Prof. Neil Hunter's group at the University of Sheffield. During this procedure, samples should be kept cold and in low light.

Pellet cells by centrifugation. Wash and then resuspend the cell pellet in a minimal volume of FLAG buffer (Table 2.7). Mix the resuspended cells with an equal volume of 0.1 mm glass beads (if this procedure is being adapted for algae, use 0.5 mm glass beads). Chill the sample on ice. Homogenize cells using a bead homogenizer (Benchmark Scientific BeadBug^{TM} Microtube homogenizer): 8x 55 seconds on MAX speed with 1 minute on ice between each round of bead beating. Bead homogenization is shown in Figure 2.9

After homogenization, centrifuge the tube with a slow spin (4000 RPM, 2 min) to separate out the beads. Beads should settle to the bottom. Pipette off the supernatant leaving the beads in the tube. To recover maximal sample, wash the beads with a small volume of FLAG buffer and pipette off the supernatant. Isolate the membranes from the phycobilisomes by

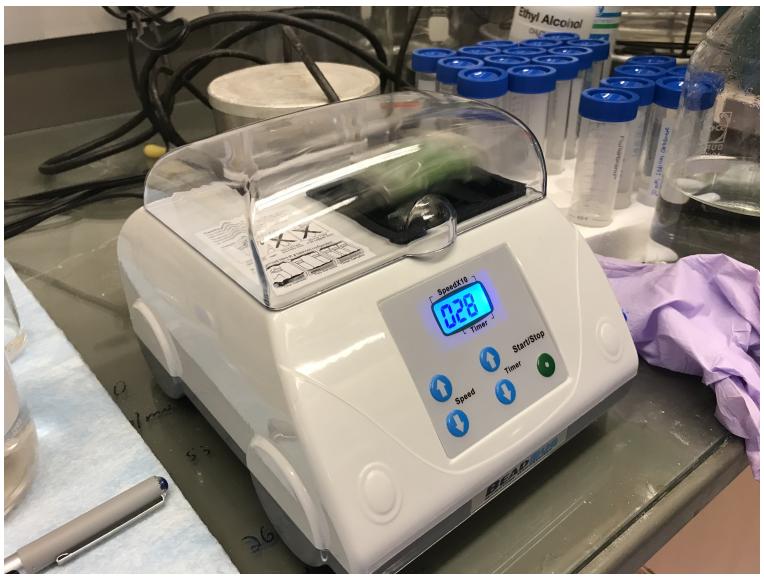

Figure 2.9: Photograph of bead homogenization of *Synechocystis* sp PCC 6803 to prepare membrane fragment samples.

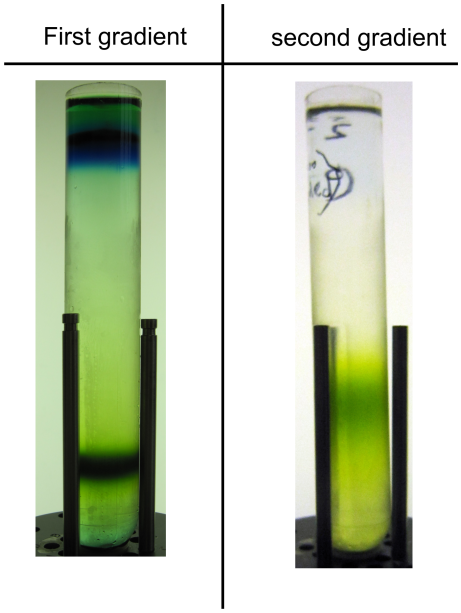

Figure 2.10: Photographs, courtesy of Dr. Craig MacGregor-Chatwin from Prof. Neil Hunter's group at the University of Sheffield, of *Synechocystis* sp membrane fragment bands following (left) one sucrose gradient and (right) a second sucrose gradient. In the first gradient, a dark blue band of phycobilisomes are visible at the top of the gradient. A dark green band of membrane fragments are visible toward the bottom of the tube. The second gradient has a single more dilute green band of membrane fragments.

Buffer component	Concentration
Sodium phosphate	25 mM, pH 7.4
Magnesium chloride	10 mM
Sodium chloride	50 mM
Glycerol	10% w/v
EDTA-free protease inhibitor (Roche)	1 tablet per 50 mL buffer

Table 2.7: FLAG buffer recipe for cyanobacterial membrane sample preparation.

centrifuging the supernatant from the bead homogenization (23000 RPM, 20 min) to pellet the membranes and cell debris. The supernatant should be intensely blue following this centrifugation due to the phycobilisomes and the pellet should be very green due to the membranes. The phycobilisome supernatant can be pipetted off and stored at -80 °C. The phycobilisomes require a high phosphate buffer concentration (> 0.75 M) to remain intact and energetically coupled. [8, 9] The membrane pellet should be resuspended in FLAG buffer and then centrifuged at a slow speed to pellet cell debris. Pipette off the supernatant and adjust to the appropriate OD (1.5 in 1 mm sample cell at 680 nm for 2DES) and then store aliquots at -80 °C.

The membrane sample can additionally be purified on 1-2 sucrose gradients and then concentrated if needed (Figure 2.10). The resulting sample will contain 35-45% w/w sucrose which will also act as a cryoprotectant.

2.2.3 Isolated LH2 Sample Preparation

LH2 was isolated based on a procedure adapted from Frank et al. [10] A detailed step-by-step isolation procedure as well as cell growth protocols are outlined in Dr. Peter Dahlberg's thesis. [2] *Rba. sphaeroides* cells were grown semi-aerobically at 32 °C in the dark or anaerobically at 32 °C under illumination. Cells were lysed using a French press at 14,000 PSI and centrifuged (12,000 RPM JA 30.50 Ti for 20 minutes at 4 °C) to remove unlysed cell debris. The supernatant was ultra centrifuged (50,000 RPM 50.2 Ti for 90 minutes) resulting in a pellet containing light harvesting complexes. The pellet was solubilized to OD 50

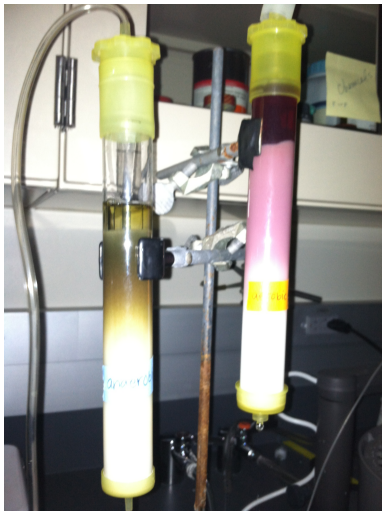

Figure 2.11: Photograph of anion exchange column purification step of LH2 isolation. Anaerobic LH2 is being purified on left column and is green in color. Semi-aerobic LH2 is being purified on the right column and is pink in color.

cm^{-1} at 850 nm in 0.6% Lauryldimethylamine-oxide (LDAO) 10 mM Tris-HCl and then run through a continuous 0.6 – 1.2 M sucrose gradient in an ultra centrifuge (50,000 RPM at 4 °C) overnight. The lower red band was removed and dialysed into 5 mM imidazole 10 mM Tris-HCl 0.06% LDAO at pH 7.5. The LDAO in dialysed sample was increased by an additional 0.06% and then separated on Ni-NTA column to remove Histidine-tagged reaction center. The LH2 fraction eluted from the column under 5 mM imidazole 10 mM Tris-HCl 0.06% LDAO at pH 7.5. The LH2 fraction was then purified by a DEAE-Sephacel anion exchange column eluting with 0-320 mM NaCl 20 mM Tris-HCl 0.1% LDAO at pH 8.0. Figure 2.11 shows a photograph of LH2 from anaerobically and semi-aerobically grown cells being purified on an anion exchange column. The purified isolated LH2 sample was buffer exchanged into 20 mM Tris-HCl 0.06% LDAO at pH 7.5 to 0.3 OD at 800 nm in a 200 μm quartz sample cell.

2.2.4 Rba. sphaeroides Membrane Preparation

Membrane fragments from the purple bacterium *Rba. sphaeroides* were prepared by the same initial lysing and centrifugation steps in the LH2 isolation procedure. This procedure

is detailed by Dahlberg et al. [11, 12] *Rba. sphaeroides* cultures were grown at 32 °C either anaerobically under illumination or semi-aerobically in the dark with agitation. Cells were pelleted and then resuspended in a smaller volume and homogenized. Cells were ruptured by French press at 14,000 PSI. The resulting sample was centrifuged at 12,000 RPM (JA 30.50 Ti) for 20 min to pellet cell debris and unlysed cells. The supernatant was collected and diluted to an OD of 1.5 in 1 mm path length at 800 nm.

REFERENCES

[1] E. Harel, A. F. Fidler, and G. S. Engel. Real-time mapping of electronic structure with single-shot two-dimensional electronic spectroscopy. *Proc. Natl. Acad. Sci. USA*, 107(38):16444–16447, 2010.

[2] P. D. Dahlberg. *Energy Transfer Events in Photosynthesis Observed in vivo Using Nonlinear Ultrafast Spectroscopies*. Thesis, University of Chicago, 2016.

[3] S. H. Sohail, P. D. Dahlberg, M. A. Allodi, S. C. Massey, P.-C. Ting, E. C. Martin, C. N. Hunter, and G. S. Engel. Communication: Broad manifold of excitonic states in light-harvesting complex 1 promotes efficient unidirectional energy transfer *in vivo*. *J. Chem. Phys.*, 147:131101, 2017.

[4] T. Brixner, T. Mancal, I. V. Stiopkin, and G. R. Fleming. Phase-stabilized two-dimensional electronic spectroscopy. *J. Chem. Phys.*, 121:4221–4236, 2004.

[5] S. C. Massey, P. C. Ting, S. H. Yeh, P. D. Dahlberg, S. H. Sohail, M. A. Allodi, E. C. Martin, S. Kais, C. N. Hunter, and G. S. Engel. Orientational dynamics of transition dipoles and exciton relaxation in LH2 from ultrafast two-dimensional anisotropy. *J. Phys. Chem. Lett.*, 10:270–277, 2019.

[6] V. P. Singh, A. F. Fidler, B. S. Rolczynski, and G. S. Engel. Independent phasing of rephasing and non-rephasing 2D electronic spectra. *J. Chem. Phys.*, 139(8):084201, 2013.

[7] R. Rippka, J. Deruelles, J. B. Waterbury, M. Herdman, and R. Y. Stanier. Generic assignments, strain histories and properties of pure cultures of cyanobacteria. *J. Gen. Microbiol.*, 111:1–61, 1979.

[8] M. Gwizdala, A. Wilson, and D. Kirilovsky. In vitro reconstitution of the cyanobacterial photoprotective mechanism mediated by the orange carotenoid protein in *Synechocystis* PCC 6803. *The Plant Cell*, 23(7):2631–2643, 2011.

[9] L. Bar-Eyal, A. Shperberg-Avni, Y. Paltiel, N. Keren, and N. Adir. Light harvesting in cyanobacteria: The phycobilisomes. In R. Croce, R. van Grondelle, H. van Amerongen, and I. H. van Stokkum, editors, *Light Harvesting in Photosynthesis*, book section 5. CRC Press, Boca Raton, FL, 2018.

[10] H. A. Frank, B. W. Chadwick, J. J. Oh, D. Gust, T. A. Moore, P. A. Liddell, A. L. Moore, L. R. Makings, and R. J. Cogdell. Triplet-triplet energy transfer in B800-B850 light-harvesting complexes of photosynthetic bacteria and synthetic carotenoporphyrin molecules investigated by electron spin resonance. *Biochim. Biophys. Acta*, 892:253–263, 1987.

[11] P. D. Dahlberg, P.-C. Ting, S. C. Massey, E. C. Martin, C. N. Hunter, and G. S. Engel. Electronic structure and dynamics of higher-lying excited states in light harvesting complex 1 from *Rhodobacter sphaeroides*. *J. Phys. Chem. A*, 120:4124–4130, 2016.

[12] P. D. Dahlberg, P.-C. Ting, S. C. Massey, M. A. Allodi, E. C. Martin, C. N. Hunter, and G. S. Engel. Mapping the ultrafast flow of harvested solar energy in living photosynthetic cells. *Nat. Commun.*, 8:988–994, 2017.

CHAPTER 3

ORIENTATIONAL DYNAMICS OF TRANSITION DIPOLES AND EXCITON RELAXATION IN LH2 FROM ULTRAFAST TWO-DIMENSIONAL ANISOTROPY

Light-harvesting complexes in photosynthetic organisms display fast and efficient energy transfer dynamics, which depend critically on the electronic structure of the coupled chromophores within the complexes and their interactions with their environment. We present ultrafast anisotropy dynamics, resolved in both time and frequency, of the transmembrane light-harvesting complex LH2 from *Rhodobacter sphaeroides* in its native membrane environment using polarization-controlled two-dimensional electronic spectroscopy. Time-dependent anisotropy obtained from both experiment and modified Redfield simulation reveals an orientational preference for excited state absorption and an ultrafast equilibration within the B850 band in LH2. This ultrafast equilibration is favorable for subsequent energy transfer toward the reaction center. Our results also show a dynamic difference in excited state absorption anisotropy between the directly excited B850 population and the population that is initially excited at 800 nm, suggesting absorption from B850 states to higher-lying excited states following energy transfer from B850*. These results give insight into the ultrafast dynamics of bacterial light harvesting and the excited state energy landscape of LH2 in the native membrane environment.

3.1 Background on LH2 Light Harvesting

Transmembrane pigment–protein complexes harvest light from the sun and transfer energy to the reaction center (RC) with high quantum efficiency. [2] In purple bacteria, the peripheral antenna, light-harvesting complex 2 (LH2), contains 27 bacteriochlorophyll *a* (BChl

a) arranged in two distinct rings termed B800 and B850 according to their wavelengths of maximum absorption (Figure 1a inset). [3] This dense packing of chromophores within a protein scaffold is common to light-harvesting complexes and results in a complicated electronic structure with a manifold of excitonic states. Energy migrates through LH2 from B800 to B850 on a 700-800 fs timescale [4–6] and undergoes ultrafast intra-B850 band energy transfer from higher-lying B850* excited states in 60-200 fs. [7] LH2 in *Rhodobacter sphaeroides* (*Rba. sphaeroides*) absorbs solar energy and transfers excitations to energetically-downstream light-harvesting complex 1 (LH1) and then to the RC to initiate photochemistry. [2, 8, 9] After absorption, excitations in LH2 undergo exciton relaxation, during which their transition dipoles can reorient. This reorientation is constrained by the two-dimensional ring structure of LH2. [7, 10, 11] Exciton localization and the time–dependence of transition dipole orientations will produce transient anisotropy, which can be readily measured with polarization–dependent experiments. Generalized Förster theory suggests that the degree of excitation delocalization within B800 and B850 influences the energy transfer and relaxation processes. [12] This delocalization has been probed by pump-probe anisotropy, photon echo peak shift, and superradiance experiments. [13–17]

3.2 Polarization Control in Nonlinear Spectroscopy

Two-dimensional electronic spectroscopy (2DES) [18–20] provides information not accessible in pump-probe experiments by providing frequency resolution in both the excitation and detection domains while maintaining ultrafast time resolution. By controlling the polarization of the laser pulses, we can observe transient anisotropic dynamics of pigment-protein complexes. Anisotropy in multidimensional spectroscopy has been used to monitor the orientational dynamics of transition dipoles in hydrogen bonding networks in water both experimentally [21–23] and theoretically. [24] Recently, the approach revealed excitonic hopping on carbon nanotube thin films [25], enabled spectral feature assignment in chlorophylls [26], and showed vibrational relaxation and energy transfer in an explosive. [27] Other polar-

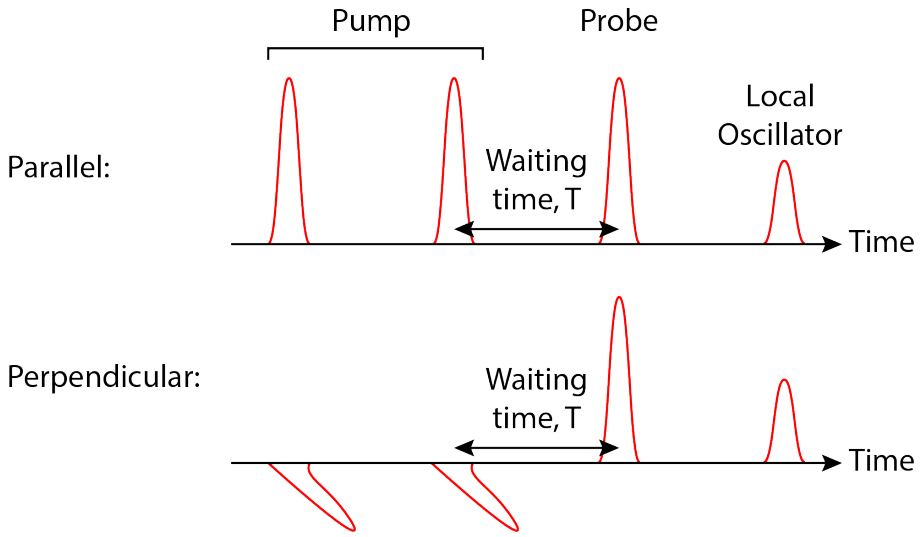

Figure 3.1: Pulse sequence polarizations for anisotropy experiments. (Top) all-parallel, $\langle ZZZZ \rangle$, and (bottom) perpendicular excitation, $\langle XXZZ \rangle$.

ization–dependent third-order spectroscopy experiments have been utilized to suppress and amplify selected pathways [28–31] and to probe changes in transition dipoles such as quantum coherences in LH2. [32]

3.3 Two-Dimensional Anisotropy of LH2

We extend the application of two-dimensional anisotropy spectroscopy to study the anisotropic dynamics of LH2. We follow the dynamics of transition dipole reorientation in this light-harvesting complex to improve our understanding of the excited state energy landscape. We are able to reproduce the temporal trends in our 2D anisotropy spectra using modified Redfield theory. In 2DES, three time-ordered ultrafast pulses interact with the sample resulting in a third-order polarization that generates a stimulated emission (SE)/ground state bleach (GSB)/excited state absorption (ESA) signal in a phase-matched direction. Two-dimensional spectra correlate excitation wavelengths (λ_{exc}) with detection wavelengths (λ_{det}) of SE/GSB/ESA at a given waiting time, T. [20] 2DES spectra are collected using the GRadient Assisted Photon Echo Spectroscopy (GRAPES) apparatus which spatially encodes the time delay between pulses 1 and 2, coherence time, τ. [33] The all-parallel,

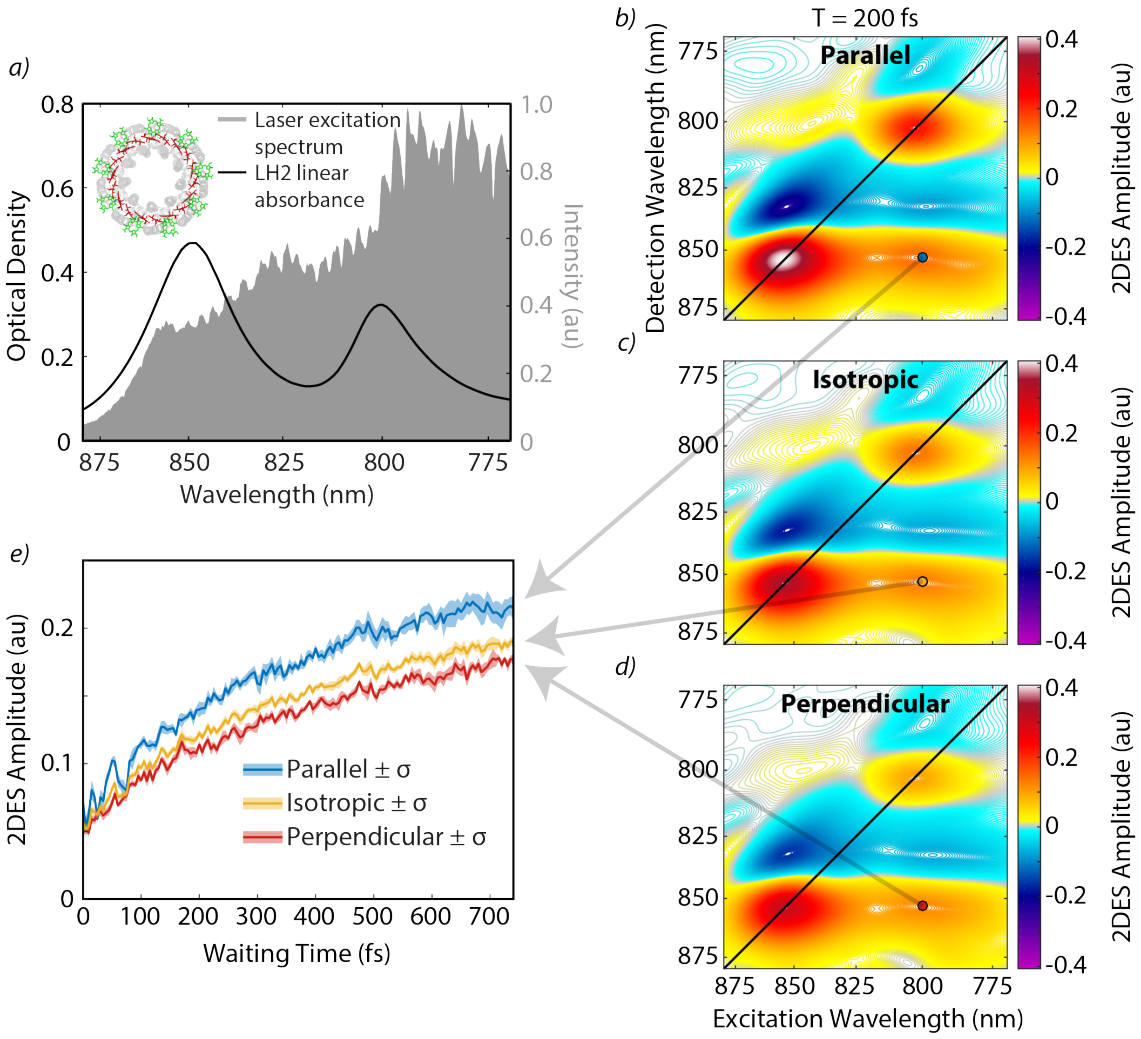

Figure 3.2: (a) Linear absorbance of LH2-only membranes in a 200 μm path length and the laser excitation spectrum (gray shaded area) used in two-dimensional electronic spectroscopy (2DES) experiments. The laser spectrum is broad enough to interrogate both the B800 and B850 bands. Inset shows the crystal structure of LH2 from *Rhodoblastus acidophilus* (PDB ID: 1NKZ). [3] B800 and B850 rings of BChl *a* are shown in green and red, respectively, with phytyl tails removed for visual clarity. (b, c, d) Absorptive 2DES spectra of LH2-only membranes at a waiting time of 200 fs for (b) all–parallel $\langle ZZZZ \rangle$, (c) isotropic, and (d) perpendicular $\langle XXZZ \rangle$ polarization sequences. (e) Waiting time traces shown as an average of six scans from the stimulated emission/ground state bleach crosspeak feature ($\lambda_{exc} = 800$ nm, $\lambda_{det} = 853$ nm) for all–parallel (blue) and perpendicular (red) experiments and the calculated isotropic (yellow) response. Shaded area indicates ± the standard error of the mean (σ) from six scans.

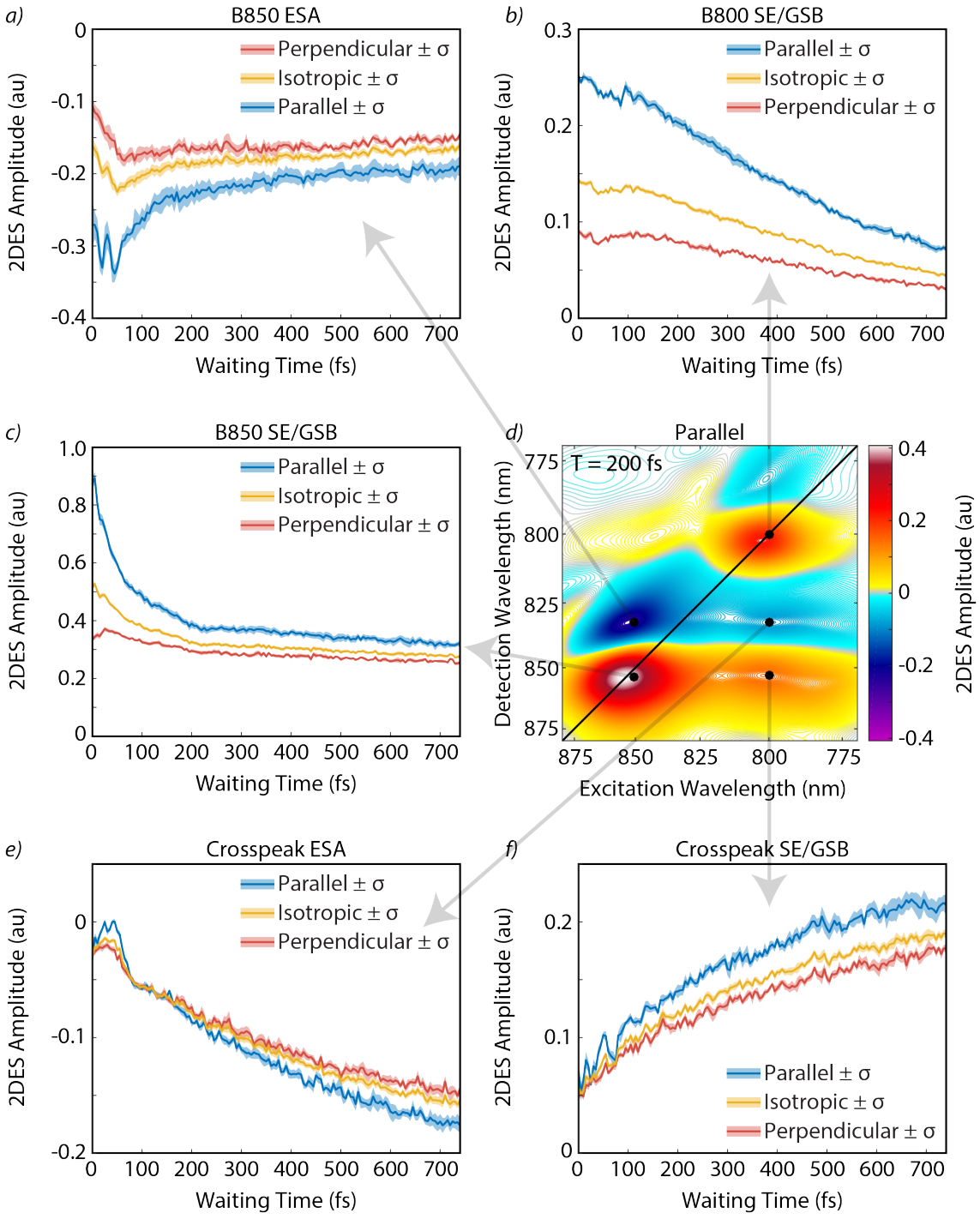

Figure 3.3: Waiting time traces of 2DES from an average of six scans for all–parallel, perpendicular experiments, and the isotropic signal from the a) B850 diagonal ESA ($\lambda_{exc} = 850$ nm, $\lambda_{det} = 832$ nm), b) B800 diagonal ($\lambda_{exc} = 800$ nm, $\lambda_{det} = 800$ nm), c) B850 diagonal SE/GSB ($\lambda_{exc} = 850$ nm, $\lambda_{det} = 854$ nm), e) crosspeak ESA ($\lambda_{exc} = 800$ nm, $\lambda_{det} = 832$ nm), and f) crosspeak SE/GSB ($\lambda_{exc} = 800$ nm, $\lambda_{det} = 853$ nm) features. Shaded area indicates ± the standard error of the mean (σ) from six scans. d) Absorptive parallel 2DES spectrum from waiting time T = 200 fs showing the spectral locations of each waiting time trace.

$\langle ZZZZ \rangle$, and perpendicular excitation, $\langle XXZZ \rangle$, pulse sequence polarizations (Figure 3.1 are acquired separately using an achromatic half-wave plate to rotate the polarization of pulses 1 and 2 by 90°.

For this anisotropy study, LH2 in its native membrane environment was prepared from an LH2-only mutant of *Rba. sphaeroides*. [34] Details on the preparation of membrane fragments can be found in Section 3.6.1. The laser excitation spectrum used for 2DES experiments covered the Q_y absorbance peaks of both B800 and B850 (Figure 3.2a). Parallel and perpendicular 2DES spectra in Figure 3.2b and 3.2d reveal similar spectral features with a positive SE/GSB diagonal peak at 800 nm corresponding to B800, a strong diagonal B850 feature with contributions from SE/GSB (positive) just below the diagonal near 850 nm and ESA (negative) just above the diagonal near 850 nm. The growth of the crosspeak in the lower right quadrant is observed as energy transfers from B800 to B850 with both SE/GSB and ESA components. These features are consistent with previous 2DES studies on isolated LH2 and live cells of *Rba. sphaeroides*. [34–36] Additional waiting time traces from the B800, B850, and lower crosspeak features are shown in Figure 3.3.

3.4 Simulated Anisotropy from Modified Redfield Theory

To construct the Hamiltonian and simulate 2D electronic and anisotropy spectra using modified Redfield theory, we need the geometric orientation of transition dipoles and the couplings between them. A high-resolution crystal structure is not available for LH2 from *Rba. sphaeroides*. Cryo-electron microscopy of LH2 in *Rba. sphaeroides* demonstrates C9 symmetry of its molecular aggregation. [37] Due to the lack of high-resolution crystal structures, the positions of transition dipole moments of BChls are adopted from a high-resolution crystal structure of LH2 from *Rbl. acidophilus* (PDB ID: 1NKZ) with the same nine-fold symmetry, as shown in Figure 1a. [3] A previous study showed that the circular dichroism spectra (CD) of LH2 complexes from various purple bacteria primarily fall into two categories: *molischianum*-like or *acidophilus*-like, and *Rba. sphaeroides* is considered to be in the former

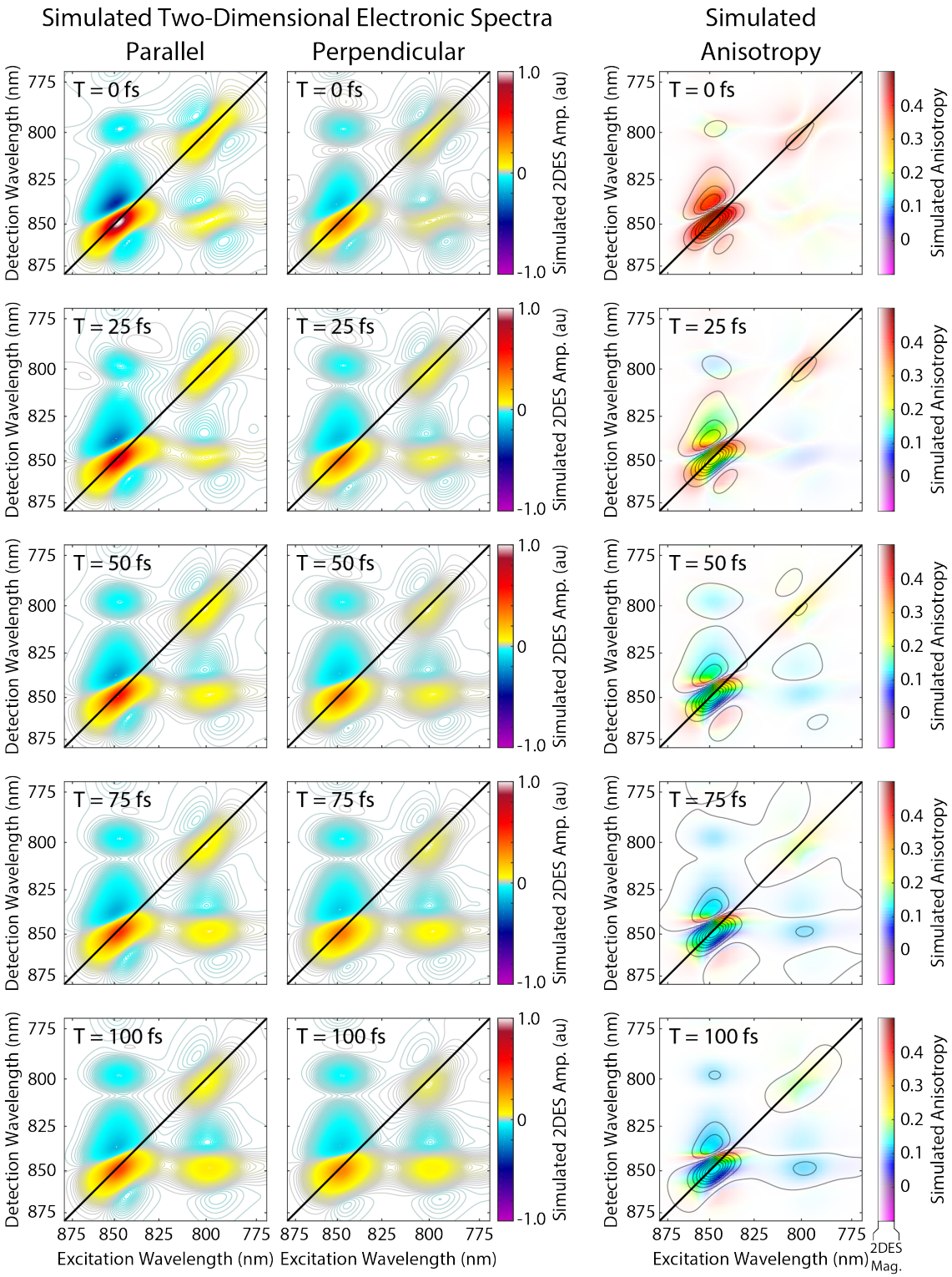

Figure 3.4: Simulated waiting time series of 2DES parallel (left column), perpendicular (center column), and anisotropy (right column) spectra at waiting times of 0, 25, 50, 75, and 100 fs (top to bottom).

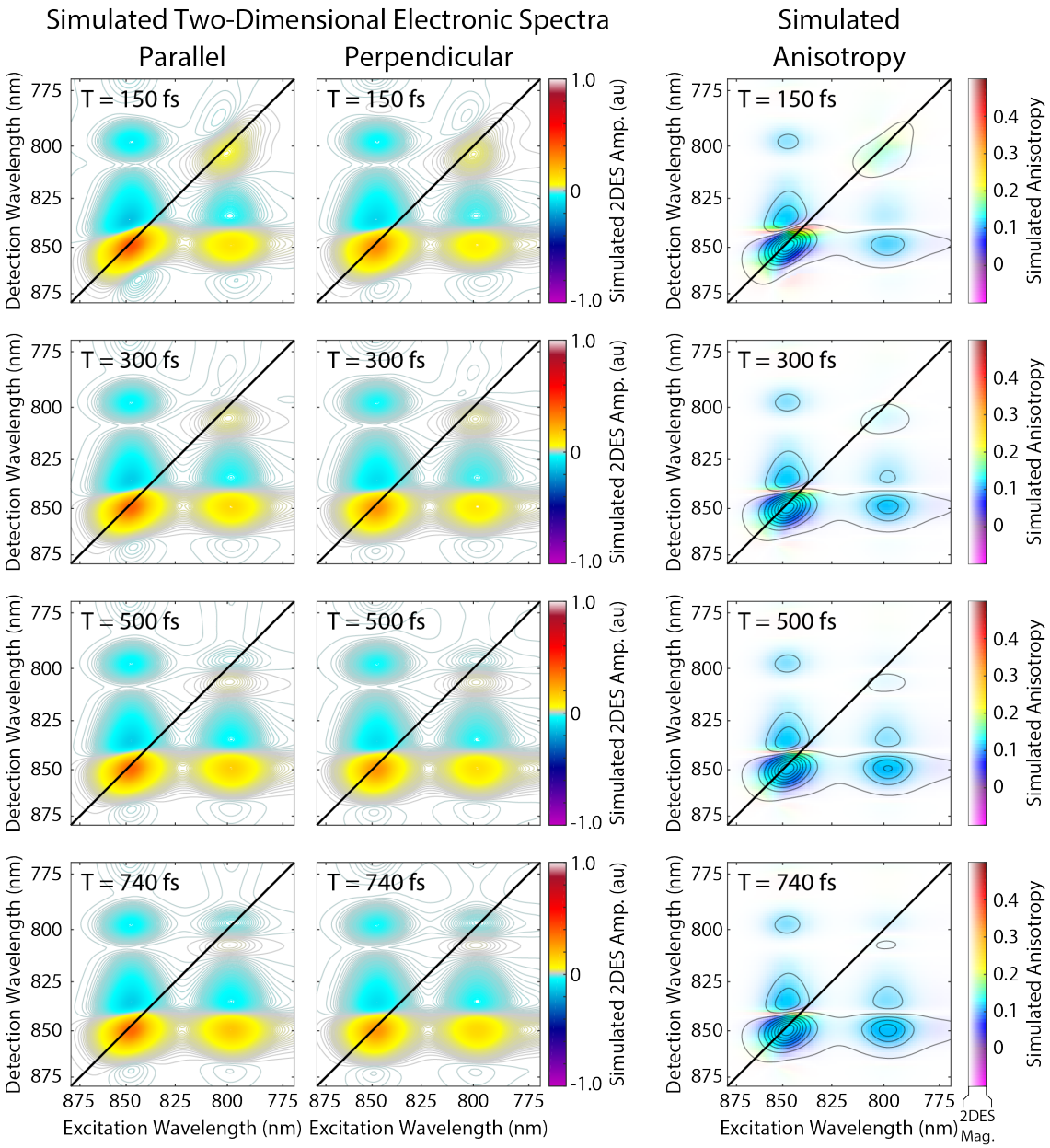

Figure 3.5: Simulated waiting time series of 2DES parallel (left column), perpendicular (center column), and anisotropy (right column) spectra at waiting times of 150, 300, 500, and 740 fs (top to bottom).

category. [38] Because CD spectroscopy is sensitive to the orientations of transition dipole moments, we adopted the orientations of the BChl Q_y transition dipoles from the crystal structure of LH2 from *Rsp. molischianum* (PDB ID: 1LGH [39]) and separately applied rotations on B800, B850α, and B850β transition dipole moments as in Georgakopoulou et al. to better align with the reported features in CD spectra of LH2 from *Rba. sphaeroides* and maintain a nine-fold symmetry. [38, 40] The detailed information of the model parameters and all simulated 2D electronic and anisotropy spectra are provided in Figures 3.4-3.5.

3.5 Anisotropy Dynamics of Spectral Features

The time-dependent anisotropy signal *r(T)* for each (λ_{exc}, λ_{det}) point on the 2DES spectrum was calculated by combining the parallel ($I_{\parallel}$) and perpendicular ($I_{\perp}$) absorptive time-dependent signals in the following equation:

$$r(T) = \frac{I_{\parallel}(T) - I_{\perp}(T)}{I_{\parallel}(T) + 2I_{\perp}(T)} \tag{3.1}$$

A waiting time series of 2DES anisotropy spectra (Figure 3.6a) reveals correlations between the transition dipoles at the excitation wavelength and those at the detection wavelength at several waiting times. Anisotropy spectra at additional waiting times are shown in Figure 3.15. An alternative representation of anisotropy spectra at early waiting times is shown in Figure 3.16. Waiting time traces (Figure 3.6b) show time-dependent anisotropic dynamics from various features in the spectra. These results are reproducible over multiple experimental runs, as shown in Figures 3.18-3.20. Anisotropy values are summarized in an illustrative table in Figure 3.7.

The measured anisotropy of the B850 SE/GSB feature (trace C in Figure 3.6b) reveals a fast 60 $\pm$ 3 fs decay of the anisotropy signal, starting at 0.35 and decaying to approximately 0.1. The anisotropy of the B800 main diagonal peak (trace A in Figure 3.6b) starts close to 0.4 and decays on a $\sim$400 fs timescale. These results agree with published transient absorp-

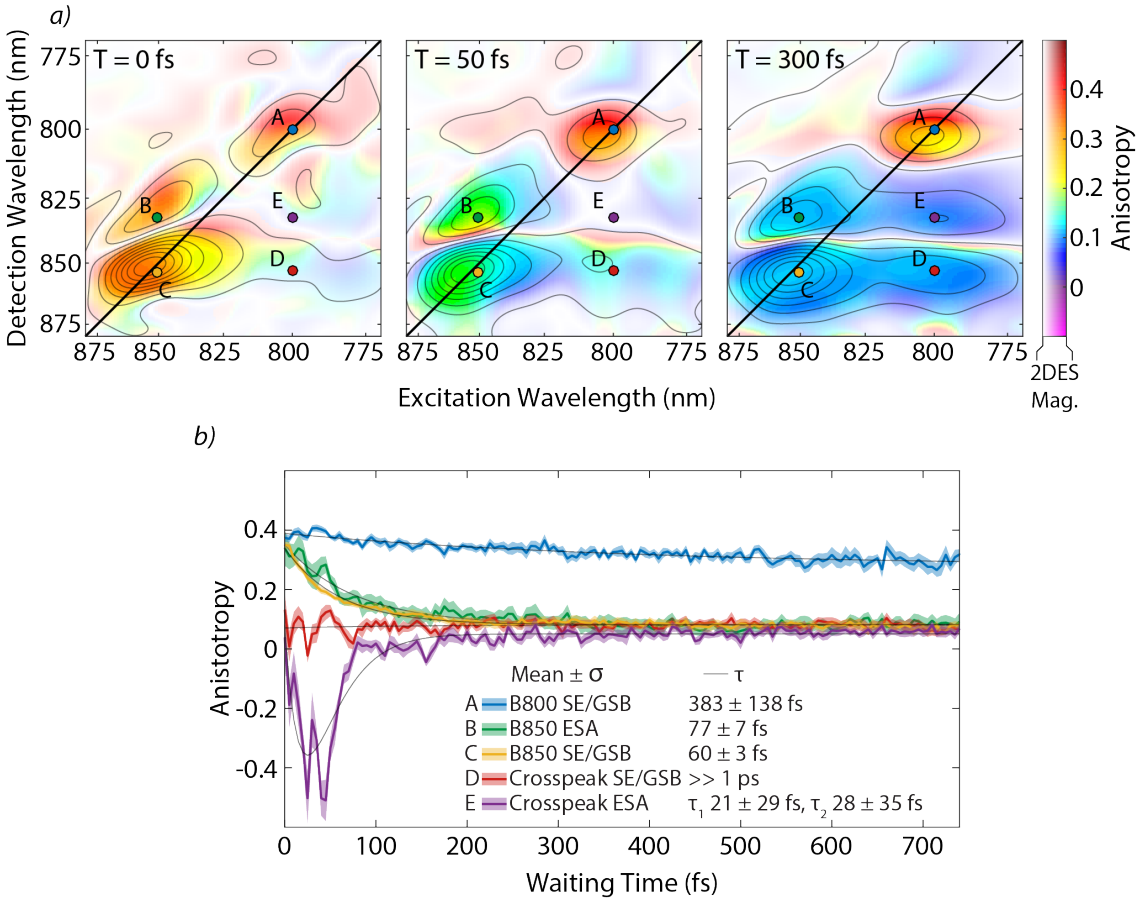

Figure 3.6: (a) Waiting time series of 2DES anisotropy in LH2-only membranes at 0 fs, 50 fs, and 300 fs. Color saturation level and gray contours indicate the all-parallel 2DES signal magnitude at the corresponding waiting time. Colored dots indicate points corresponding to the waiting time traces in (b). (b) Waiting time traces of anisotropy from the B800 diagonal SE/GSB (λ_{exc} = 800 nm, λ_{det} = 800 nm [A, blue]), B850 diagonal ESA (λ_{exc} = 850 nm, λ_{det} = 832 nm [B, green]), B850 diagonal SE/GSB (λ_{exc} = 850 nm, λ_{det} = 854 nm [C, yellow]), crosspeak SE/GSB (λ_{exc} = 800 nm, λ_{det} = 853 nm [D, red]), and crosspeak ESA (λ_{exc} = 800 nm, λ_{det} = 832 nm [E, purple]). Shaded area indicates ± standard error of the mean (σ) from six scans. The gray traces indicate the monoexponential fit to traces A-D and the biexponential fit to trace E.

tion anisotropy experiments. [7, 11, 41] The rapid anisotropy decay of the B850 SE/GSB corresponds to an ultrafast reorientation of the B850 transition dipoles. [15, 42] Simulated anisotropy spectra (Figure 3.10a) and waiting time trace (trace C in Figure 3.10b) reproduce these dynamics. Novoderezhkin et al. attribute the 300-400 fs B800 anisotropy decay to one-exciton coherence dynamics; [7] however, our data do not cover sufficiently long waiting times to observe the picosecond timescale inter-chromophore hopping in the B800 ring. [7, 11] In our simulations, the B800 anisotropy decay (trace A in Figure 3.10b) is faster than the experimental anisotropy decay of this feature. We are unable to definitively assign this difference, but the faster decay seen in simulation may be due to coherence dynamics which is not included in the model.

In addition to B800 (A) and B850 (C) diagonal SE/GSB signals, we also observe the anisotropy dynamics of the B850 diagonal ESA (trace B in Figure 3.6b) feature which was inaccessible in prior experiments. The B850 diagonal ESA feature (B) shows an initial anisotropy of 0.34 at T = 0 fs. An anisotropy value of 0.34 indicates preferential alignment of ESA with the initial excitation transition dipole. This result indicates that once the system has been polarized along a given axis, the system is more polarizable along that axis than along any other axis. The anisotropy rapidly decays to approximately 0.1 with a 77 $\pm$ 7 fs lifetime due to ultrafast reorientation and randomization of transition dipoles on B850, similar to that observed in the diagonal B850 SE/GSB (C) feature. This result is also in agreement with simulation (trace B in Figure 3.10b), which shows a rapid anisotropy decay from a value of 0.42.

The crosspeak SE/GSB (trace D in Figure 3.6b) has an approximately constant anisotropy across the measured waiting times. This crosspeak corresponds to SE/GSB from the B850 ring following energy transfer from B800 and B850*, which occur on respective timescales of 700-800 fs and 60-200 fs. [7] The anisotropy dynamics show some oscillatory structure at T $<$ 100 fs, which may result from energy transfer from B850* to B850, but this signal is less clear than the crosspeak ESA (E) anisotropy dynamics due to overlap with strong cou-

Transition dipole orientation for pump interactions	Transition dipole orientation for probe interactions (SE/GSB/ESA)	Anisotropy
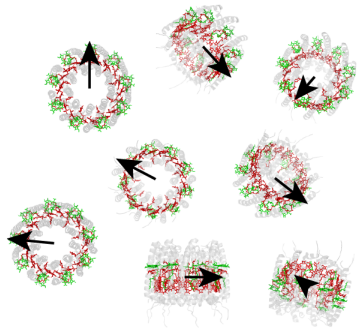	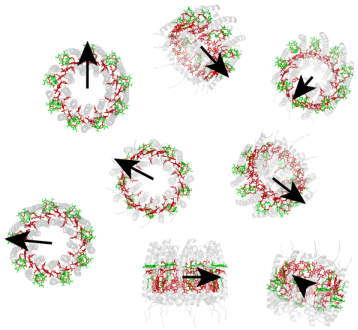	= 0.4 Transition dipole for probe interaction is aligned with transition dipole for pump interaction in an ensemble of randomly oriented complexes
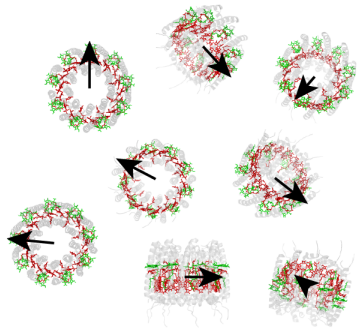	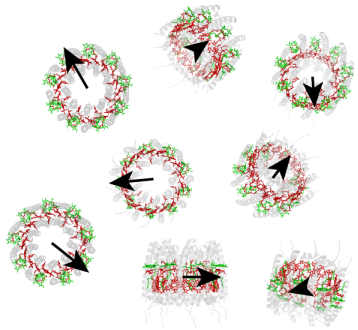	Decays from 0.4 to 0.1 Transition dipole randomly reorients during the waiting time, T, but is constrained to point in the plane of the ring
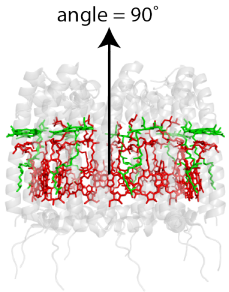	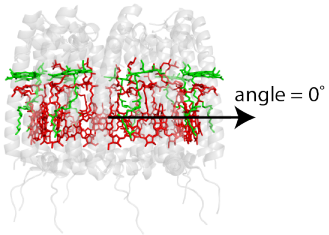	Negative Energy transfer during waiting time between out-of-plane and in-plane states; > 45˚ reorientation of transition dipole such that $\perp$ > $\parallel$

Figure 3.7: Illustrative table of anisotropy values (right column) corresponding to pump (left column) and probe (center column) transition dipole orientations.

plings in the spectral region of the crosspeak SE/GSB (D). Energy transfer from an initially localized B800 state into the B850 ring results in an immediately random orientation of the transition dipole in the plane of the ring, indicating transfer into a delocalized B850 state, as evidenced by the constant ∼0.1 anisotropy value of the crosspeak SE/GSB (D). If the system retained memory of the initial B800 transition dipole orientation following energy transfer before reorienting, we would expect the anisotropy dynamics of the crosspeak SE/GSB (D) to resemble the anisotropy of the B850 SE/GSB (C) and ESA (B) features with an ultrafast decay from ∼0.4.

A waiting time anisotropy trace from the lower crosspeak ESA (trace E in Figure 3.6b) shows an initial ultrafast growth of a negative anisotropy signal, followed by an ultrafast decay of this negative anisotropy to approach a constant anisotropy value of ∼0.1 at T > 100 fs. This anisotropy is distinctly different from the dynamics of the lower crosspeak SE/GSB (D), which is flat across the range of waiting times, and additionally different from the B850 SE/GSB (C) and ESA (B) anisotropies, which only decay. While the B850 diagonal ESA (B) and the B850 diagonal SE/GSB (C) features show identical dynamics, the crosspeak ESA (E) and SE/GSB (D) are fundamentally different from one another. We are unable to assign the oscillations in the anisotropies at early waiting times (T < 100 fs) and would require additional measurements to confirm and assign these dynamics. At early waiting times (T < 50 fs), the growth of a negative anisotropy of the crosspeak ESA (E) may correspond to ESA from B850 to higher-lying excited states following energy transfer from B850*. B850* states are higher-lying states in the B850 manifold that spectrally overlap with B800 and additionally relax to B850 on the 60-200 fs timescale. [7] Calculated energies of the B850* states at different realizations of the static disorder are shown in Figure 3.8. This timescale of energy transfer from B850* to B850 corresponds to the ultrafast rise of the negative anisotropy signal. Dynamics corresponding to these B850* states will overlap spectrally with the B800 diagonal and crosspeak features, as opposed to the B850 diagonal features. At later waiting times, this ESA signal originating from B850* would be overwhelmed by ESA

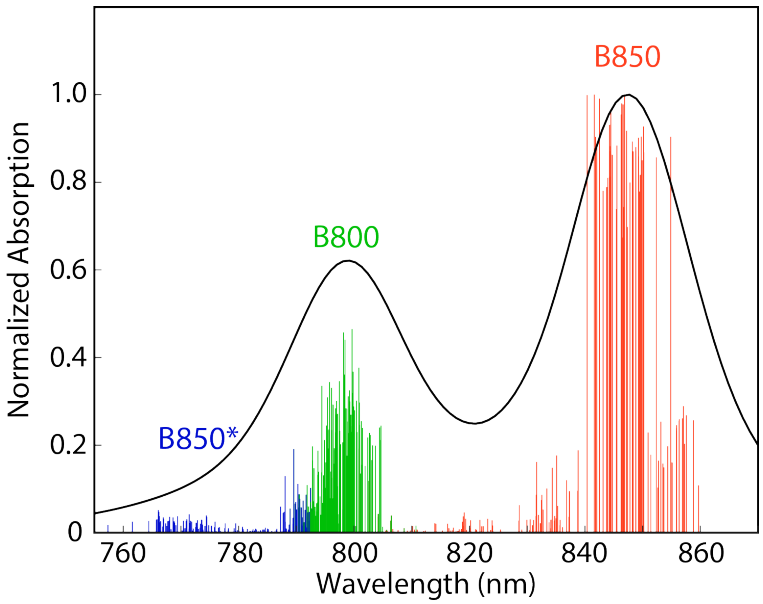

Figure 3.8: Energies of calculated exciton transition dipole moments for 20 realizations of static disorder. Each stick shows the energy of a given k state for a given realization of static disorder. The height of each stick is the square of the transition dipole magnitude normalized to conserve oscillator strength for the given realization of static disorder. States 1 – 9 (red) are the lower-lying B850 states, states 10-18 (green) are mostly localized on the B800 chromophores, and states 19-27 (blue) correspond to the higher-lying B850 states known as B850*. The black trace shows the normalized calculated linear absorption spectrum averaged over 20 realizations of static disorder.

from B850 following energy transfer from B800, which supports why the negative anisotropy only persists for <100 fs.

ESA from B850 to higher-lying excited states following energy transfer from B850* may correspond to energy transfer to or from a state with out-of-plane character to give rise to an anisotropy of < 0.1 at early times. In fluorescence experiments, a negative anisotropy value arises from relaxation or energy transfer to a state with the transition dipole oriented 45-135° from the initially excited state; transfer or relaxation between states with orthogonal transition dipoles yields an anisotropy value of -0.2. [43, 44] Nonlinear anisotropy experiments are sensitive to differences in transition dipole orientation between different electronic states in ESA signals in addition to reporting on changes in orientation due to relaxation and energy transfer. [44] The anisotropy measurement of an ESA feature correlates the initial excitation transition dipole moment orientation (in this case, B850*) with the transition dipole moment

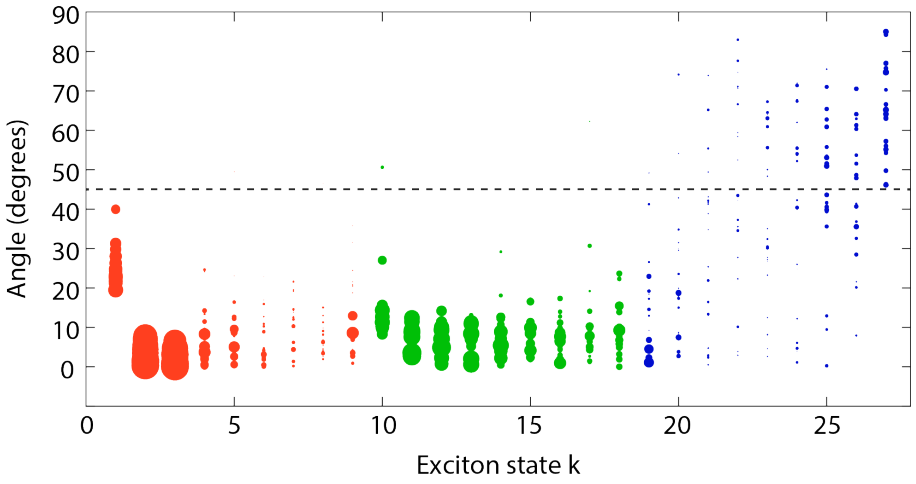

Figure 3.9: Characterization of the out-of-plane character of calculated exciton transition dipole moments for 20 realizations of static disorder. For each k state, each filled dot shows the angle of the transition dipole moment relative to the plane of the LH2 ring for a given realization of static disorder. The diameter of the dot is scaled by the magnitude of the transition dipole moment. States 1 – 9 (red) are the lower-lying B850 states, states 10-18 (green) are mostly localized on the B800 chromophores, and states 19-27 (blue) correspond to the higher-lying B850 states known as B850*. The B850* states show significantly more out-of-plane character than the B850 and B800 states.

orientation of the ESA transition (in this case, B850 to a higher-lying excited state). In the case of a two-dimensional ring structure, like LH2, the anisotropy could correspond to ESA to and from a state in which the transition dipole is coplanar to the ring following energy transfer from a state in which the transition dipole is orthogonal to the plane of the ring (or vice versa). The B850* transition dipoles have significant out-of-plane character, and in many instances of static disorder are oriented $> 45°$ from the plane of the LH2 ring (Figure 3.9). Energy transfer from an out-of-plane B850* state to B850 states parallel to the plane of the ring, and then subsequent ESA to higher-lying excited states parallel to the plane of the ring would be in agreement with these negative anisotropy signals. At longer times (T $>$ 100 fs), the anisotropy of the crosspeak ESA feature is close to 0.1 indicating that the transition dipole moment orientation is randomly distributed but constrained to be coplanar to the ring. [13, 15, 41, 45]

The B850 SE/GSB feature also shows a trend of anisotropy decay constants across the

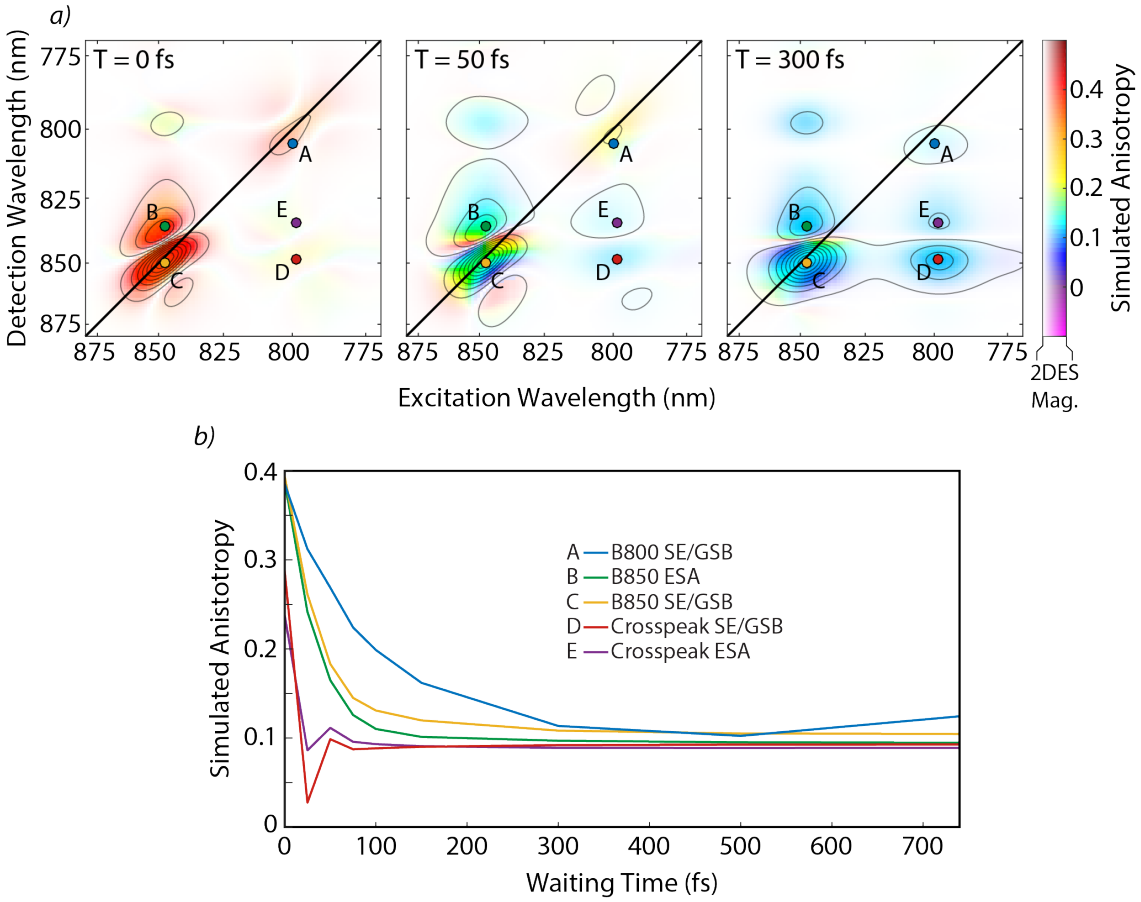

Figure 3.10: (a) Simulated waiting time series of 2DES anisotropy in LH2 at 0 fs, 50 fs, and 300 fs. Color saturation level and gray contours indicate the simulated all-parallel 2DES signal magnitude at the corresponding waiting time. Colored dots indicate points corresponding to the waiting time traces in (b). (b) Waiting time traces of simulated anisotropy from the B800 diagonal SE/GSB ($\lambda_{exc} = 800$ nm, $\lambda_{det} = 805$ nm [A, blue]), B850 diagonal ESA ($\lambda_{exc} = 847$ nm, $\lambda_{det} = 836$ nm [B, green]), B850 diagonal SE/GSB ($\lambda_{exc} = 847$ nm, $\lambda_{det} = 850$ nm [C, yellow]), crosspeak SE/GSB ($\lambda_{exc} = 799$ nm, $\lambda_{det} = 849$ nm [D, red]), and crosspeak ESA ($\lambda_{exc} = 799$ nm, $\lambda_{det} = 834$ nm [E, purple]).

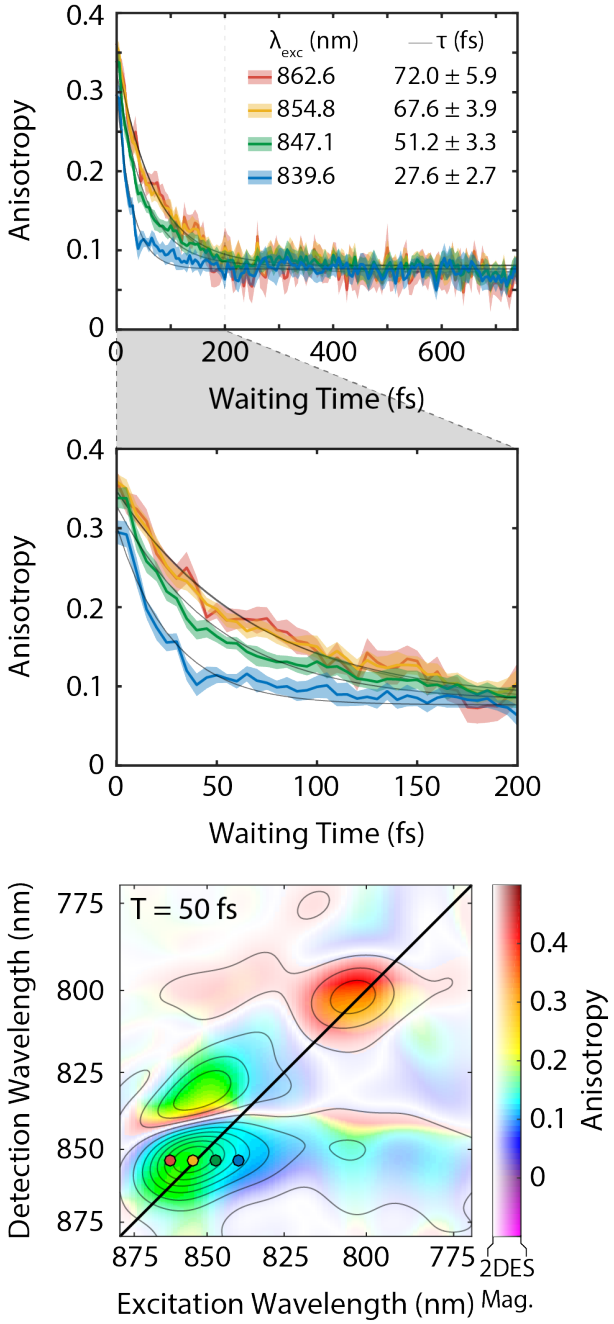

Figure 3.11: Waiting time traces of anisotropy from the SE/GSB B850 feature at varying λ_{exc} values and $\lambda_{det} = 854$ nm. Shaded area indicates ± the standard error of the mean (σ) from six scans. Gray traces show the monoexponential fit to each waiting time trace. The middle panel zooms in on the first 200 fs. Colored dots on the 2D anisotropy spectrum from T = 50 fs show the spectral locations of the corresponding waiting time traces.

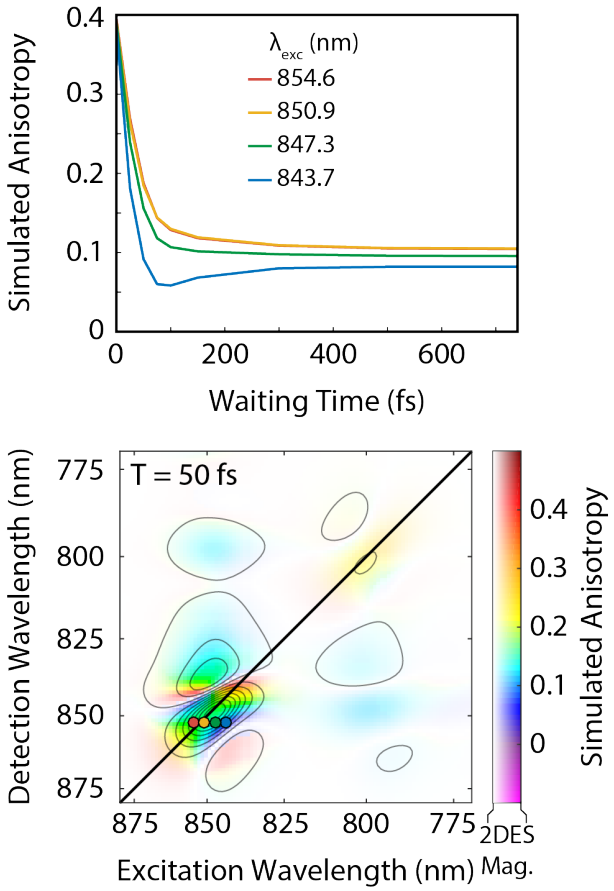

Figure 3.12: Simulated waiting time traces of anisotropy from the SE/GSB B850 feature at varying λ_{exc} values and λ_{det} = 852 nm. Colored dots on the simulated 2D anisotropy spectrum from T = 50 fs show the spectral locations of the corresponding waiting time traces.

excitation wavelength axis (λ_{exc}) (Figure 3.11). A series of points from the same detection wavelength (854 nm) after being excited at varying wavelengths across the B850 band reveal that those excited on the blue edge show a faster anisotropy decay. An excitation wavelength of 839.6 nm yields an anisotropy decay constant of 27.6 ± 2.7 fs, whereas an excitation wavelength of 862.6 nm yields an anisotropy decay constant of 72.0 ± 5.9 fs. This trend of faster anisotropy decay at bluer excitation wavelengths moving across the B850 SE/GSB band is reproduced in our simulation (Figure 3.12). In pump-probe anisotropy experiments, Nagarajan et al. showed a faster anisotropy decay with 827 nm excitation than with 850 nm excitation, but they did not see a continuous trend across excitation wavelength. [13] These higher energy excitons relax quickly, resulting in a faster loss of transition dipole orientation and more rapid anisotropy decay than excitons on the red edge of the band. Segatta et al. calculated an increasing relaxation rate with increasing energy in LH2 B850 excitons using TD-DFT/MMPol at cryogenic temperature. [46] The rapid relaxation of higher energy excitons in the B850 band limits back transfer to favor downstream energy transfer to LH1 and the RC. Similar directional behavior has been observed in LH1 *in vivo*. [47]

3.6 Experimental Methods

The principles and experimental setup of 2DES have been detailed elsewhere. [20] The data in this chapter were acquired using GRAPES. [33] The pulse used in this experiment was generated by a 5 kHz regenerative amplifier seeded by a Ti:sapphire oscillator (Coherent Inc.). The pulse was then passed through 2 m of argon gas (15 psi above atmospheric) and an SLM-based pulse shaper (Biophotonics Inc.) to obtain sub-25 fs pulses. Polarization rotation was achieved using a broadband achromatic half-wave plate (Union Optic cemented, achromatic, zero order, 500-900 nm). Wave plate bandwidth performance is characterized in Figure 3.13. Integrated power across the beam at the time of the experiment showed suppression > 113:1. 2DES correlates absorption frequency with signal frequency as a function of a time delay between pulses 2 and 3, waiting time T, which was continuously scanned

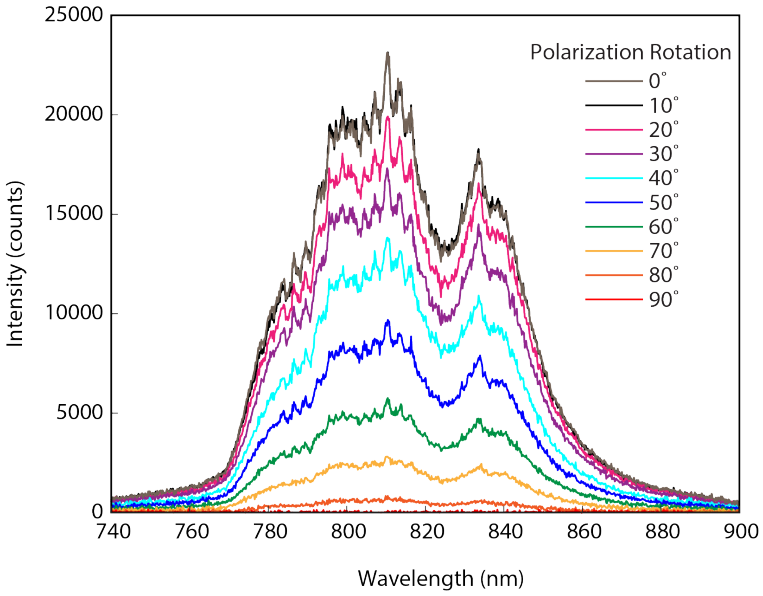

Figure 3.13: Characterization of wave plate bandwidth performance showing polarization flatness across wavelength. Polarization was rotated in 5° increments of the achromatic half-wave plate (10° polarization rotation). The beam was then detected using a spectrometer after passing through a Glan-Thompson polarizer.

by a mechanical translation stage at a speed of 1.5 μm/sec. The signal was heterodyned with an attenuated local oscillator pulse and spectrally resolved with an Andor Shamrock spectrometer, followed by detection on a high-speed CMOS 2D array camera (Phantom Miro M310) at a collection rate of 50 Hz. Absorptive spectra were produced by reconstructing the nonrephasing component of the data according to Sohail et al. [47] The absolute phase of the 2D spectra was determined by fitting to separately acquired pump-probe spectra according to the projection-slice theorem. [20, 48] All parallel and perpendicular 2D spectra were normalized to the global maximum of the averaged parallel spectra.

Data runs were acquired in rapid succession, collecting three parallel polarization sequence runs, six perpendicular polarization sequence runs, and then three additional parallel polarization sequence runs for each sample. Each run was phased separately by fitting to transient absorption data according to the projection slice theorem. The average of the six iterations of each polarization sequence was then obtained. Error calculated from the average of 6 runs was propagated through in the anisotropy calculations. Coherence times were

sampled from -250 – 250 fs in 0.9 fs steps. Waiting times were sampled from -200 to 740 fs in 0.2 fs steps while continuously scanning the delay stage at 1.5 μm/s. Data were collected as two-dimensional images of coherence time versus rephasing wavelength. A cubic spline interpolation was performed to achieve axes of coherence time versus rephasing frequency. A Welch window was applied in the waiting time domain to window out the optical frequency. An FFT was performed to achieve axes of coherence time versus rephasing time. Apodization was performed in the coherence and rephasing time domains. The signal was shifted to 0 rephasing and coherence time. A 2DFFT was performed to achieve axes of coherence frequency versus rephasing frequency.

3.6.1 Sample Preparation of LH2-only Membranes

An LH2-only mutant of *Rba. sphaeroides* with deletion of the *pufBALMX* genes was constructed using the method delineated by Mothersole et al. [49] LH2-only membrane fragments were prepared as described by Dahlberg et al. [34, 50] For convenience, that procedure is reproduced here. LH2-only cells were grown in the dark at 30 °C under semi-aerobic conditions. Membrane fragments containing LH2 were obtained from whole cells by partial lysis of cell membranes using a French Press at 14,000 PSI. Larger cellular fragments were pelleted and removed by centrifugation of the lysate at 12,000 rpm (JA 30.STI) for 20 minutes. The supernatant was collected and analyzed in a 200 μm quartz cuvette (Starna Cells Inc.) after dilution to an optical density of 0.3 at 800 nm.

3.7 Monoexponential and Biexponential Fits

Monoexponential fits to the data used the model $Ae^{-t/\tau} + c$ where the amplitude (A), time constant (τ), and offset (c) were simultaneously fit to the data. Biexponential fits followed a model for consecutive reactions A→B→C with rate constant k_1 describing the rate of A→B and k_2 describing the rate of B→C with associated lifetimes τ_1 and τ_2 where

$[B(t)] = \frac{k_1}{k_2 - k_1}[A(0)](e^{-k_1 t} - e^{-k_2 t})$. [51] Using this model, biexponential fits to the data (Figure 3.6) followed $\frac{1/\tau_1}{1/\tau_2 - 1/\tau_1}(A_1 e^{-t/\tau_1} - A_2 e^{-t/\tau_2}) + c$ where the amplitudes (A_1 and A_2), time constants (τ_1 and τ_2), and offset (c) were simultaneously fit to the data.

3.8 Modified Redfield Simulation Parameters

Each BChl in LH2 is modeled as a two-level system that describes its $S_0 \rightarrow S_1$ (Q_y) transition, and the assembly of all BChls can be described by the Frenkel exciton Hamiltonian in the site representation:

$$H = \Sigma_i E_i \mid i\rangle\langle i \mid + \Sigma_{ij} V_{ij} \mid i\rangle\langle j \mid \tag{3.2}$$

where E_i is the Q_y excited-state energy of the i-th BChl, and V_{ij} is the excitonic coupling between the i-th and j-th BChls. Except the interaction between the nearest neighbor BChls of B850 ring, all the coupling between the BChls are calculated using the point dipole approximation:

$$V_{ij} = J\frac{\hat{d}_i \cdot \hat{d}_j - 3(\hat{d}_i \cdot \hat{r}_{ij})(\hat{d}_j \cdot \hat{r}_{ij})}{\mid r_{ij} \mid^3} \tag{3.3}$$

where $\hat{d}_i$ and $\hat{d}_j$ respectively represent the unit vectors of the i-th and j-th BChl transition dipole moment and $\hat{r}_{ij}$ is the unit vector of the connecting vector pointing from the magnesium of BChl i to the magnesium of BChl j. The prefactor in the coupling term J is assigned to be 205553 Å^3 cm^{-1}, which corresponds to an experimental dipole transition moment of 6.39 D. Adopted from a previous study using *ab initio* calculation [52], the intradimer and interdimer resonant coupling between the neighboring BChls of B850 are set to 320 and 255 cm^{-1}, respectively. The site energies of B800, B850α, and B850β are set to 12562, 12550, and 12350 cm^{-1}, respectively. These parameters provide reasonable agreement of the simulated linear absorption spectrum to the experimental measurement. Simulated and experimental linear absorption and circular dichroism (CD) spectra are shown in Figure

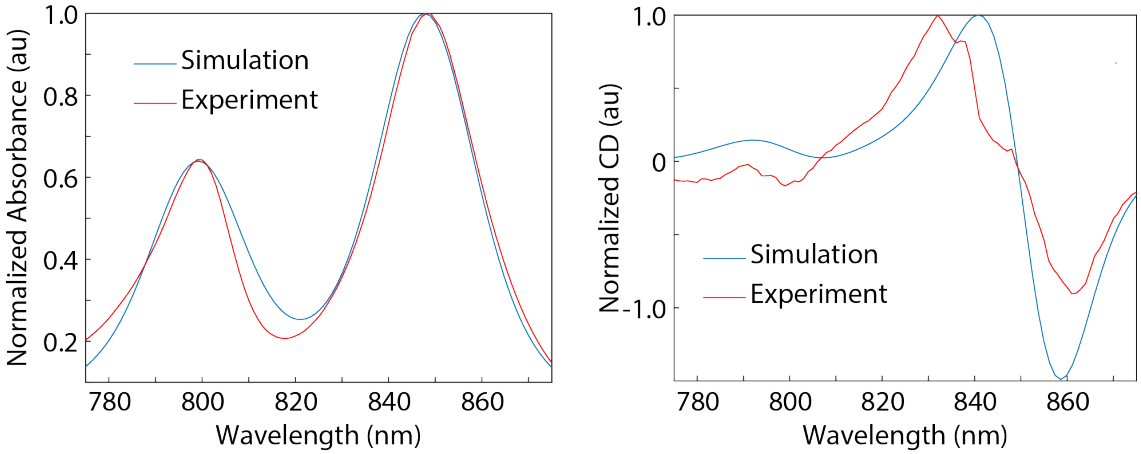

Figure 3.14: Simulated and experimental (left) Linear absorbance and (right) CD spectra of LH2 corresponding to the simulation parameters used in modified Redfield calculations. Experimental CD spectrum is of isolated LH2 from semi-aerobically grown *Rba. sphaeroides*. Experimental linear absorbance spectrum is of LH2-only membranes.

3.14.

To simulate linear and 2D spectra of LH2, we implemented modified Redfield theory to include simultaneously the excitation energy transfer dynamics of weakly-coupled B800 BChls, strongly-coupled B850 BChls, and non-negligible coupling between the B800 and B850 BChls. In modified Redfield theory, the diagonal part of the electron-phonon coupling is treated in a non-perturbative fashion, and therefore it generates more accurate relaxation rates and line shapes by including multiphonon effects. [53] The theoretical details of simulating linear absorption, circular dichroism, and the 2D spectra using modified Redfield theory can be found in Ref. [54–56].

The spectral line shapes are largely dictated by the form of spectral density, which characterizes the coupling between different electronic states and phonon modes. In the present study we model the spectral density as overdamped Brownian oscillators [57] with the form written as:

$$C(\omega) = \frac{2\lambda\omega\gamma}{\omega^2 + \gamma^2} \tag{3.4}$$

where γ is the bath relaxation rate and $\hbar\lambda$ is the reorganization energy. The shape of

spectral density is assumed to be identical for both B800 and B850 BChls but with different electron-vibrational coupling strength, featured by the use of distinct reorganization energies for the B800 (λ_{800}) and B850 (λ_{850}) BChls. The inhomogeneous broadening effect is included through introducing static disorder to the site energies of B800 and B850 BChls, which is done by adding a normally distributed random number to the site energy of each B800 and B850 chromophore with assigned standard deviations σ_{800} and σ_{850}, respectively. Generally, it is assumed that B800 and B850 have different amount of static disorder as well. [58, 59] The resulting simulated spectra are obtained by averaging over spectral signal calculated under different realizations of static disorder. These four parameters (λ_{800}, λ_{850}, σ_{800}, and σ_{850}) are selected by generating the simulated linear absorption spectra and the 2D absorptive map (with all-parallel polarization pulse sequence) at zero waiting time that reasonably agrees with the corresponding experimental spectra. The ensemble spectra are averaged over 300 realizations of the static disorder. In the current study, we use reorganization energies $\hbar\lambda_{800}$ and $\hbar\lambda_{800}$ as 80 and 230 cm^{-1}, respectively. The static disorder parameters σ_{800} and σ_{850} are set to 60 and 130 cm^{-1}, respectively.

3.9 Supporting Figures

The following figures include spectra collected at additional waiting times (Figure 3.15) and an alternative representation of the data without saturation scaling based on the 2DES signal magnitude (Figure 3.16). We show the excitation wavelength-dependent anisotropy dynamics of the B850 ESA feature in Figure 3.17. We present data from a secondary dataset collected on a different day in Figures 3.18 - 3.20 which show similar trends to the primary dataset.

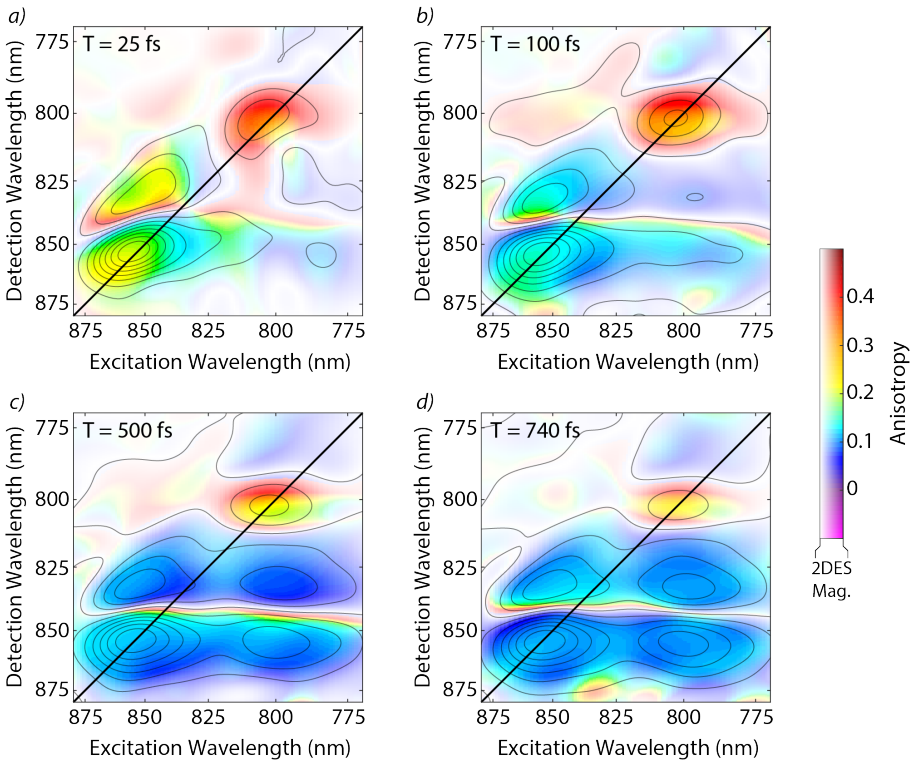

Figure 3.15: Waiting time series of 2DES anisotropy spectra at waiting times of a) 25 fs, b) 100 fs, c) 500 fs, and d) 740 fs. Color saturation level and gray contours indicate the all-parallel 2DES signal magnitude at the corresponding waiting time.

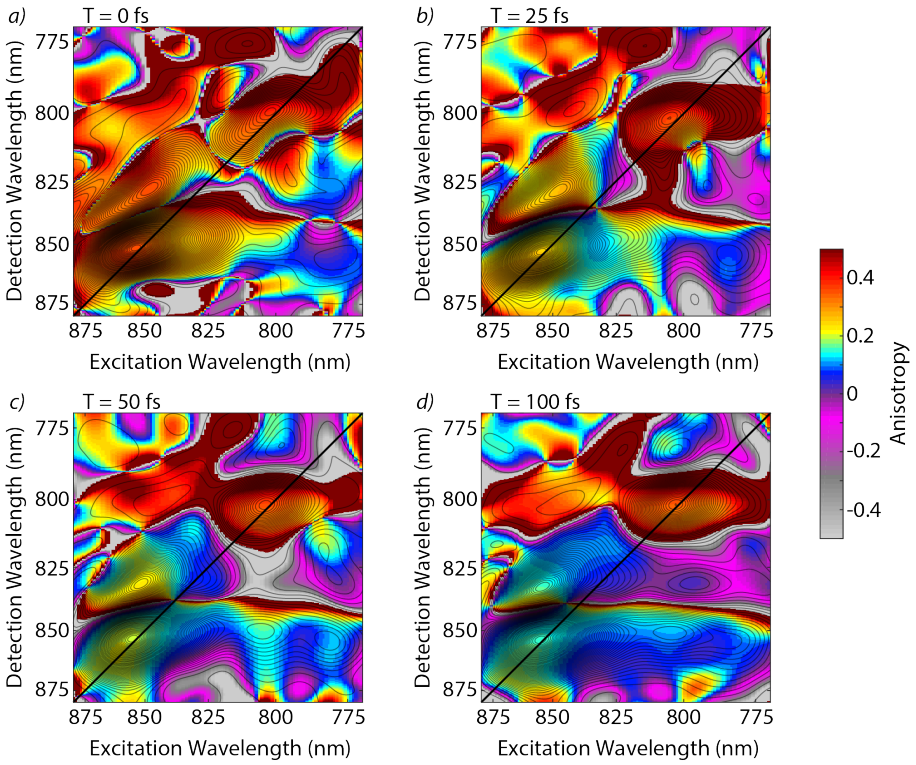

Figure 3.16: An alternative representation of the waiting time series of 2DES anisotropy spectra at waiting times of a) 0 fs, b) 25 fs, c) 50 fs, and d) 100 fs with an expanded colormap range. 100 gray contours indicate the all-parallel 2DES signal magnitude at the corresponding waiting time. No saturation scaling based on the all-parallel 2DES magnitude has been applied to these spectra.

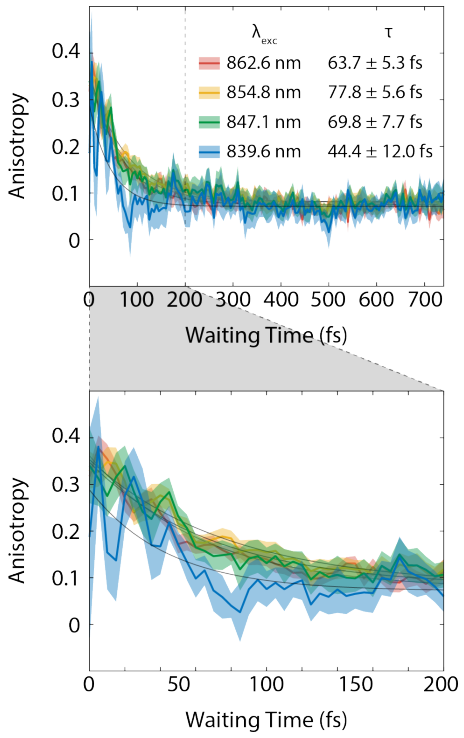

Figure 3.17: Waiting time traces of anisotropy from the ESA B850 feature at varying λ_{exc} values and $\lambda_{det} = 832$ nm. Shaded area indicates $\pm$ the standard error of the mean (σ) from six scans. Gray traces show the monoexponential fit to each waiting time trace. The bottom panel zooms in on the first 200 fs.

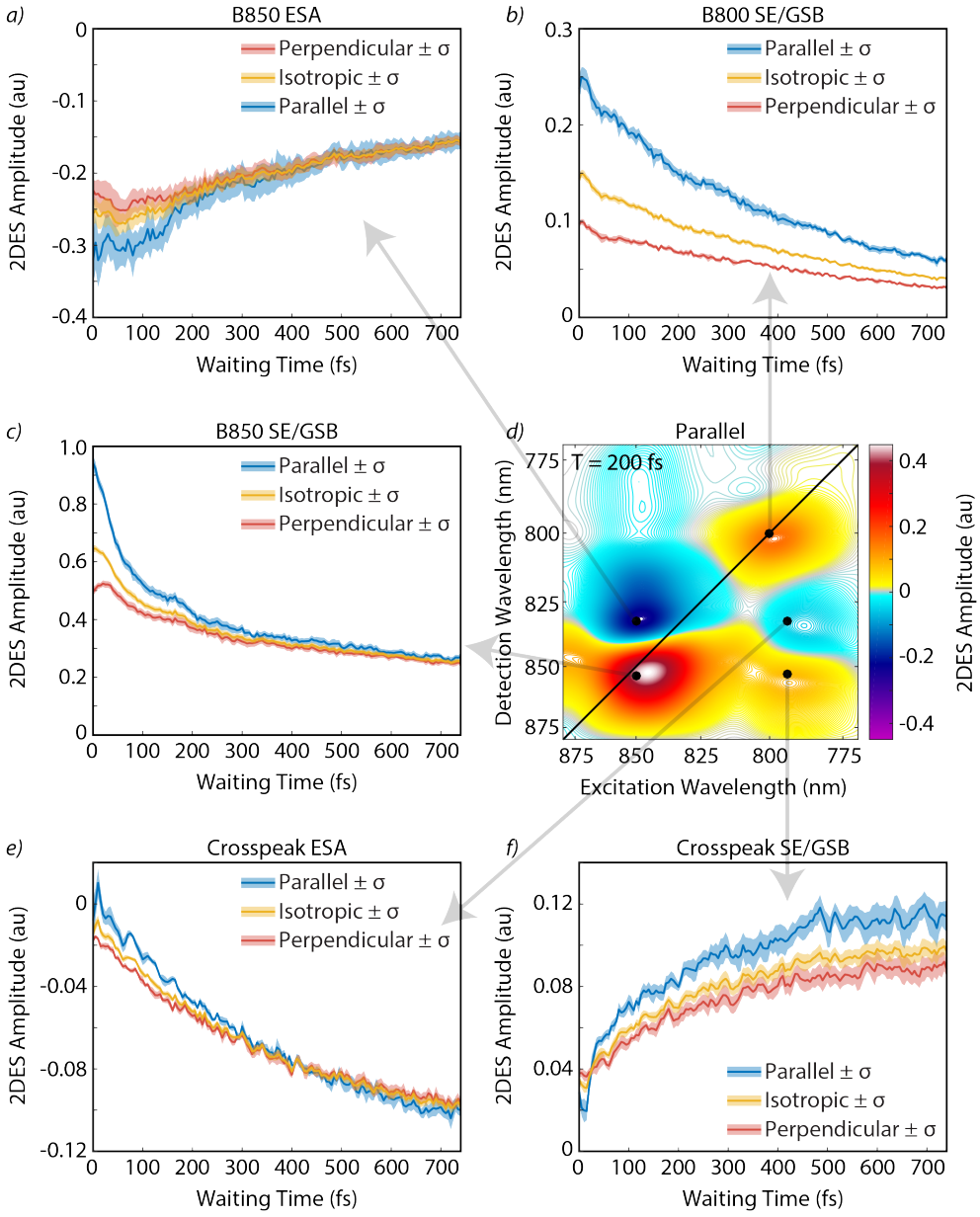

Figure 3.18: Waiting time traces of 2DES from a secondary data set collected on a different day. These data were collected at a higher power and with decreased polarization purity. Traces are from an average of six scans for all–parallel, perpendicular experiments, and the isotropic signal from the a) B850 diagonal ESA (λ_{exc} = 850 nm, λ_{det} = 832 nm), b) B800 diagonal (λ_{exc} = 800 nm, λ_{det} = 800 nm), c) B850 diagonal SE/GSB (λ_{exc} = 850 nm, λ_{det} = 854 nm), e) crosspeak ESA (λ_{exc} = 794 nm, λ_{det} = 832 nm), and f) crosspeak SE/GSB (λ_{exc} = 794 nm, λ_{det} = 853 nm) features. Shaded area indicates ± the standard error of the mean (σ) from six scans. d) Absorptive parallel 2DES spectrum from waiting time T = 200 fs showing the spectral locations of each waiting time trace.

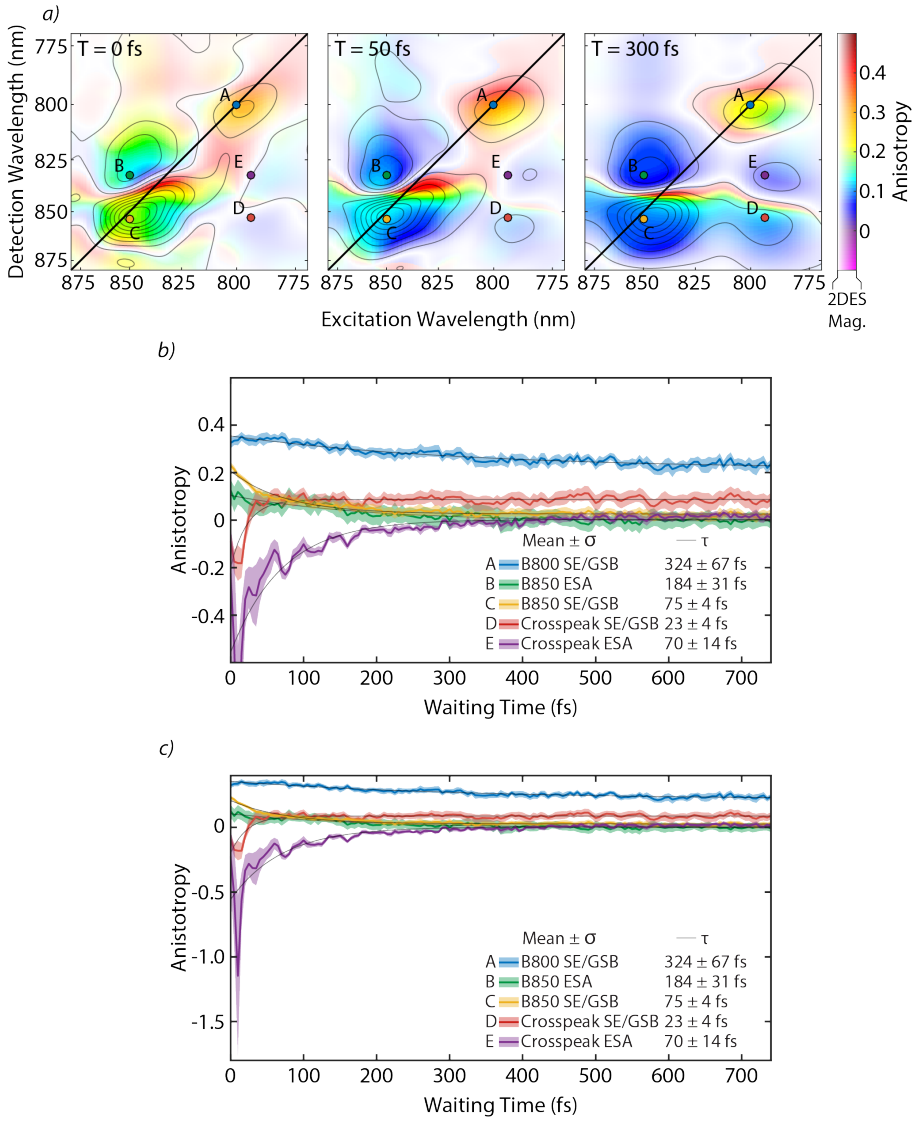

Figure 3.19: a) 2DES anisotropy waiting time series of LH2-only membranes from a secondary data set collected on a different day (same data set as shown in Figure S2). These data were collected at a higher power and with decreased polarization purity, but show similar trends in anisotropic dynamics. Spectra are shown at 0 fs, 50 fs, and 300 fs. Color saturation level and gray contours indicate the all-parallel 2DES signal magnitude at the corresponding waiting time. Colored dots indicate points corresponding to the waiting time traces in (b) and (c). b) Waiting time traces of anisotropy from the B800 diagonal SE/GSB (λ_{exc} = 800 nm, λ_{det} = 800 nm (blue)), B850 diagonal ESA (λ_{exc} = 850 nm, λ_{det} = 832 nm (green)), B850 diagonal SE/GSB (λ_{exc} = 850 nm, λ_{det} = 854 nm (yellow)), crosspeak SE/GSB (λ_{exc} = 794 nm, λ_{det} = 853 nm (red)), and crosspeak ESA (λ_{exc} = 794 nm, λ_{det} = 832 nm (purple)). Shaded area indicates ± the standard error of the mean (σ) from six scans. Gray traces show the monoexponential fit to each waiting time trace. c) Same traces as shown in (b) but with extended y-axis.

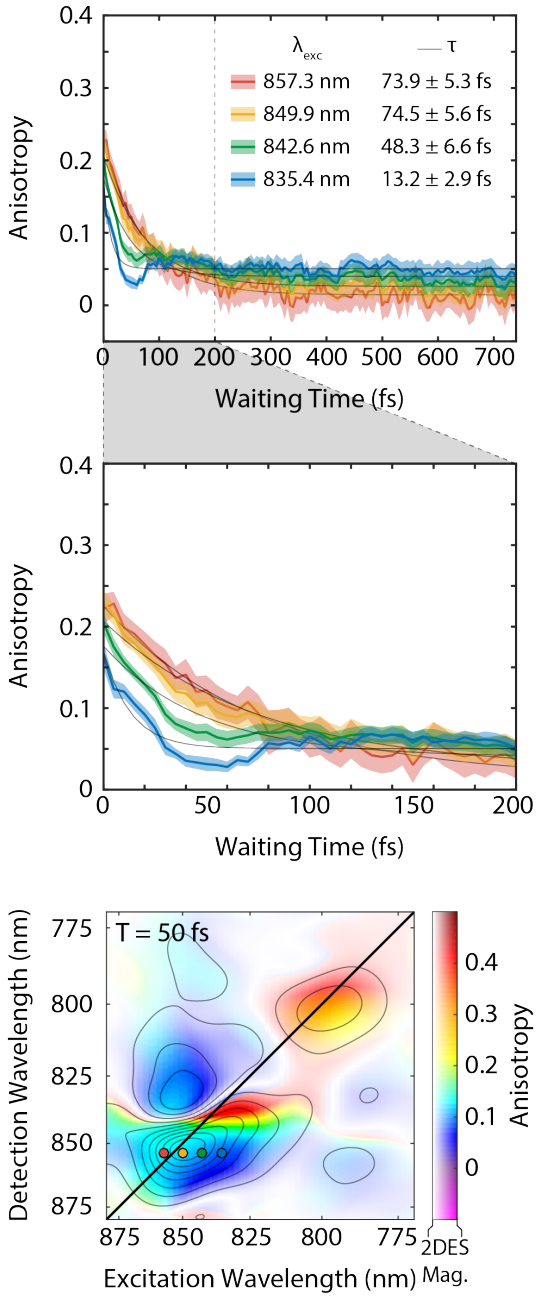

Figure 3.20: Waiting time traces of anisotropy from a secondary data set collected on a different day (same data set as shown in Figures 3.4 and 3.15) from the SE/GSB B850 feature varying λ_{exc} values at λ_{det} = 854 nm. These data were collected at a higher power and with decreased polarization purity, but show similar trends in anisotropic dynamics. Shaded area indicates ± the standard error of the mean (σ) from 6 scans. Gray traces show the monoexponential fit to each waiting time trace. The middle panel zooms in on the first 200 fs. Colored dots on the 2D spectrum from T = 50 fs show the spectral locations of the corresponding waiting time traces.

3.10 Conclusions

We have measured the first 2DES anisotropy spectra of membrane-bound LH2 from *Rba. sphaeroides*. We observed an orientational preference for ESA on the B850 ring and detected an ultrafast anisotropy decay of B850 ESA (B) that matches the magnitude and timescale of the ultrafast anisotropy decay of the previously established B850 SE/GSB (C). We also observed a negative anisotropy at early waiting times in the crosspeak ESA (E) which may be due to ESA following energy transfer to B850 from B850* states that overlap spectrally with the B800 ring. Our results show ultrafast relaxation of higher energy excitons within the B850 manifold which is favorable for directing excitons toward the RC. These data reveal dynamics underlying the B850 2DES peak that are uniquely accessible with anisotropy experiments. These experimental results agree with our simulated 2D anisotropy spectra. We believe this extension of anisotropy in 2DES will serve as a new paradigm of probing ultrafast orientational dynamics of transition dipoles and exciton dynamics on systems with confined geometry.

REFERENCES

[1] S. C. Massey, P. C. Ting, S. H. Yeh, P. D. Dahlberg, S. H. Sohail, M. A. Allodi, E. C. Martin, S. Kais, C. N. Hunter, and G. S. Engel. Orientational dynamics of transition dipoles and exciton relaxation in LH2 from ultrafast two-dimensional anisotropy. *J. Phys. Chem. Lett.*, 10:270–277, 2019.

[2] R. E. Blankenship. *Molecular Mechanisms of Photosynthesis*. John Wiley & Sons, Ltd, Chichester, West Sussex, 2nd edition, 2014.

[3] M. Z. Papiz, S. M. Prince, T. Howard, R. J. Cogdell, and N. W. Isaacs. The structure and thermal motion of the B800–850 LH2 complex from *Rps. acidophila* at 2.0Å resolution and 100K: New structural features and functionally relevant motions. *J. Mol. Biol.*, 326:1523–1538, 2003.

[4] S. Hess, E. Akesson, R. J. Cogdell, T. Pullerits, and V. Sundstrom. Energy transfer in spectrally inhomogeneous light-harvesting pigment-protein complexes of purple bacteria. *Biophys. J.*, 69:2211–2225, 1995.

[5] T. H. Joo, Y. W. Jia, J. Y. Yu, D. M. Jonas, and G. R. Fleming. Dynamics in isolated bacterial light harvesting antenna (LH2) of *Rhodobacter sphaeroides* at room temperature. *J. Phys. Chem.*, 100:2399–2409, 1996.

[6] S. Hess, M. Chachisvilis, K. Timpmann, M. R. Jones, G. J. S. Fowler, C. N. Hunter, and V. Sundstrom. Temporally and spectrally resolved subpicosecond energy transfer within the peripheral antenna complex (LH2) and from LH2 to the core antenna complex in photosynthetic purple bacteria. *Proc. Natl. Acad. Sci. U.S.A.*, 92:12333–12337, 1995.

[7] V. Novoderezhkin, M. Wendling, and R. van Grondelle. Intra- and interband transfers in the B800-B850 antenna of *Rhodospirillum molischianum*: Redfield theory modeling of polarized pump-probe kinetics. *J. Phys. Chem. B*, 107:11534–11548, 2003.

[8] M. L. Cartron, J. D. Olsen, M. Sener, P. J. Jackson, A. A. Brindley, P. Qian, M. J. Dickman, G. J. Leggett, K. Schulten, and C. N. Hunter. Integration of energy and electron transfer processes in the photosynthetic membrane of *Rhodobacter sphaeroides*. *Biochim. Biophys. Acta*, 1837:1769–1780, 2014.

[9] M. Sener, J. Strumpfer, A. Singharoy, C. N. Hunter, and K. Schulten. Overall energy conversion efficiency of a photosynthetic vesicle. *Elife*, 5, 2016.

[10] S. Hess, F. Feldchtein, A. Babin, I. Nurgaleev, T. Pullerits, A. Sergeev, and V. Sundstrom. Femtosecond energy transfer within the LH2 peripheral antenna of the photosynthetic purple bacteria *Rhodobacter sphaeroides* and *Rhodopseudomonas palustris* LL. *Chem. Phys. Lett.*, 216:247–257, 1993.

[11] J. T. M. Kennis, A. M. Streltsov, S. I. E. Vulto, T. J. Aartsma, T. Nozawa, and J. Amesz. Femtosecond dynamics in isolated LH2 complexes of various species of purple bacteria. *J. Phys. Chem. B*, 101:7827–7834, 1997.

[12] A. F. Fidler, V. P. Singh, P. D. Long, P. D. Dahlberg, and G. S. Engel. Dynamic localization of electronic excitation in photosynthetic complexes revealed with chiral two-dimensional spectroscopy. *Nat. Commun.*, 5:3286–3291, 2014.

[13] V. Nagarajan, E. T. Johnson, J. C. Williams, and W. W. Parson. Femtosecond pump-probe spectroscopy of the B850 antenna complex of *Rhodobacter sphaeroides* at room temperature. *J. Phys. Chem. B*, 103:2297–2309, 1999.

[14] M. Chachisvilis, O. Kuhn, T. Pullerits, and V. Sundstrom. Excitons in photosynthetic purple bacteria: Wavelike motion or incoherent hopping? *J. Phys. Chem. B*, 101:7275–7283, 1997.

[15] T. Pullerits, M. Chachisvilis, and V. Sundstrom. Exciton delocalization length in the B850 antenna of *Rhodobacter sphaeroides*. *J. Phys. Chem.*, 100:10787–10792, 1996.

[16] L. D. Book, A. E. Ostafin, N. Ponomarenko, J. R. Norris, and N. F. Scherer. Exciton delocalization and initial dephasing dynamics of purple bacterial LH2. *J. Phys. Chem. B*, 104:8295–8307, 2000.

[17] R. Monshouwer, M. Abrahamsson, F. van Mourik, and R. van Grondelle. Superradiance and exciton delocalization in bacterial photosynthetic light-harvesting systems. *J. Phys. Chem. B*, 101:7241–7248, 1997.

[18] J. D. Hybl, A. W. Albrecht, S. M. Gallagher Faeder, and D. M. Jonas. Two-dimensional electronic spectroscopy. *Chem. Phys. Lett.*, 297:307–313, 1998.

[19] M. L. Cowan, J. P. Ogilvie, and R. J. D. Miller. Two-dimensional spectroscopy using diffractive optics based phased-locked photon echoes. *Chem. Phys. Lett.*, 386:184–189, 2004.

[20] T. Brixner, T. Mancal, I. V. Stiopkin, and G. R. Fleming. Phase-stabilized two-dimensional electronic spectroscopy. *J. Chem. Phys.*, 121:4221–4236, 2004.

[21] K. Ramasesha, S. T. Roberts, R. A. Nicodemus, A. Mandal, and A. Tokmakoff. Ultrafast 2D IR anisotropy of water reveals reorientation during hydrogen-bond switching. *J. Chem. Phys.*, 135:054509, 2011.

[22] M. Ji, M. Odelius, and K. J. Gaffney. Large angular jump mechanism observed for hydrogen bond exchange in aqueous perchlorate solution. *Science*, 328:1003–1005, 2010.

[23] M. Ji and K. J. Gaffney. Orientational relaxation dynamics in aqueous ionic solution: Polarization-selective two-dimensional infrared study of angular jump-exchange dynamics in aqueous 6M $NaClO_4$. *J. Chem. Phys.*, 134:044516, 2011.

[24] Y. Ni and J. L. Skinner. Ultrafast pump-probe and 2DIR anisotropy and temperature-dependent dynamics of liquid water within the E3B model. *J. Chem. Phys.*, 141:024509, 2014.

[25] R. D. Mehlenbacher, J. Wang, N. M. Kearns, M. J. Shea, J. T. Flach, T. J. McDonough, M. Y. Wu, M. S. Arnold, and M. T. Zanni. Ultrafast exciton hopping observed in bare semiconducting carbon nanotube thin films with two-dimensional white-light spectroscopy. *J. Phys. Chem. Lett.*, 7:2024–2031, 2016.

[26] N. H. Lewis and G. R. Fleming. Two-dimensional electronic-vibrational spectroscopy of chlorophyll *a* and *b*. *J. Phys. Chem. Lett.*, 7:831–837, 2016.

[27] J. S. Ostrander, R. Knepper, A. S. Tappan, J. J. Kay, M. T. Zanni, and D. A. Farrow. Energy transfer between coherently delocalized states in thin films of the explosive pentaerythritol tetranitrate (PETN) revealed by two-dimensional infrared spectroscopy. *J. Phys. Chem. B*, 121:1352–1361, 2017.

[28] R. D. Mehlenbacher, T. J. McDonough, N. M. Kearns, M. J. Shea, Y. Joo, P. Gopalan, M. S. Arnold, and M. T. Zanni. Polarization-controlled two-dimensional white-light spectroscopy of semiconducting carbon nanotube thin films. *J. Phys. Chem. C*, 120:17069–17080, 2016.

[29] M. T. Zanni, N. H. Ge, Y. S. Kim, and R. M. Hochstrasser. Two-dimensional IR spectroscopy can be designed to eliminate the diagonal peaks and expose only the crosspeaks needed for structure determination. *Proc. Natl. Acad. Sci. U.S.A.*, 98:11265–11270, 2001.

[30] E. L. Read, G. S. Engel, T. R. Calhoun, T. Mancal, T. K. Ahn, R. E. Blankenship, and G. R. Fleming. Cross-peak-specific two-dimensional electronic spectroscopy. *Proc. Natl. Acad. Sci. U.S.A.*, 104:14203–14208, 2007.

[31] P. Hamm and S. Woutersen. Structure determination of trialanine in water using polarization sensitive two-dimensional vibrational spectroscopy. *J. Phys. Chem. B*, 104:11316–11320, 2000.

[32] V. P. Singh, M. Westberg, C. Wang, P. D. Dahlberg, T. Gellen, A. T. Gardiner, R. J. Cogdell, and G. S. Engel. Towards quantification of vibronic coupling in photosynthetic antenna complexes. *J. Chem. Phys.*, 142:212446, 2015.

[33] E. Harel, A. F. Fidler, and G. S. Engel. Single-shot gradient-assisted photon echo electronic spectroscopy. *J. Phys. Chem. A*, 115:3787–3796, 2011.

[34] P. D. Dahlberg, P.-C. Ting, S. C. Massey, M. A. Allodi, E. C. Martin, C. N. Hunter, and G. S. Engel. Mapping the ultrafast flow of harvested solar energy in living photosynthetic cells. *Nat. Commun.*, 8:988–994, 2017.

[35] A. F. Fidler, V. P. Singh, P. D. Long, P. D. Dahlberg, and G. S. Engel. Probing energy transfer events in the light harvesting complex 2 (LH2) of *Rhodobacter sphaeroides* with two-dimensional spectroscopy. *J. Chem. Phys.*, 139:155101–155108, 2013.

[36] M. Ferretti, R. Hendrikx, E. Romero, J. Southall, R. J. Cogdell, V. I. Novoderezhkin, G. D. Scholes, and R. van Grondelle. Dark states in the light-harvesting complex 2 revealed by two-dimensional electronic spectroscopy. *Sci. Rep.*, 6:20834–20842, 2016.

[37] T. Walz, S. J. Jamieson, C. M. Bowers, P. A. Bullough, and C. N. Hunter. Projection structures of three photosynthetic complexes from *Rhodobacter sphaeroides*: LH2 at 6 Å, LH1 and RC-LH1 at 25 Å. *J. Mol. Biol.*, 282:833–845, 1998.

[38] S. Georgakopoulou, R. N. Frese, E. Johnson, C. Koolhaas, R. J. Cogdell, R. van Grondelle, and G. van der Zwan. Absorption and CD spectroscopy and modeling of various LH2 complexes from purple bacteria. *Biophys. J.*, 82:2184–2197, 2002.

[39] J. Koepke, X. Hu, C. Muenke, K. Schulten, and H. Michel. The crystal structure of the light-harvesting complex II (B800-850) from *Rhodospirillum molischianum*. *Structure*, 4:581–597, 1996.

[40] M. Ratsep, R. Muru, and A. Freiberg. High temperature limit of photosynthetic excitons. *Nat. Commun.*, 9:99, 2018.

[41] R. Jimenez, S. N. Dikshit, S. E. Bradforth, and G. R. Fleming. Electronic excitation transfer in the LH2 complex of *Rhodobacter sphaeroides*. *J. Phys. Chem.*, 100:6825–6834, 1996.

[42] V. Nagarajan, R. G. Alden, J. C. Williams, and W. W. Parson. Ultrafast exciton relaxation in the B850 antenna complex of *Rhodobacter sphaeroides*. *Proc. Natl. Acad. Sci. U.S.A.*, 93:13774–13779, 1996.

[43] J. R. Lakowicz. *Principles of Fluorescence Anisotropy*. Springer, New York, NY, 3rd edition, 2006.

[44] K. Wynne and R. M. Hochstrasser. Coherence effects in the anisotropy of optical experiments. *Chem. Phys.*, 171:179–188, 1993.

[45] Yun-Peng Wang, Lu-Chao Du, Gang-Bei Zhu, Zhuan Wang, and Yu-Xiang Weng. Synchronous measurement of ultrafast anisotropy decay of the B850 in bacterial LH2 complex. *Chin. Phys. Lett.*, 32:023101, 2015.

[46] F. Segatta, L. Cupellini, S. Jurinovich, S. Mukamel, M. Dapor, S. Taioli, M. Garavelli, and B. Mennucci. A quantum chemical interpretation of two-dimensional electronic spectroscopy of light-harvesting complexes. *J. Am. Chem. Soc.*, 139:7558–7567, 2017.

[47] S. H. Sohail, P. D. Dahlberg, M. A. Allodi, S. C. Massey, P.-C. Ting, E. C. Martin, C. N. Hunter, and G. S. Engel. Communication: Broad manifold of excitonic states in light-harvesting complex 1 promotes efficient unidirectional energy transfer *in vivo*. *J. Chem. Phys.*, 147:131101, 2017.

[48] V. P. Singh, A. F. Fidler, B. S. Rolczynski, and G. S. Engel. Independent phasing of rephasing and non-rephasing 2D electronic spectra. *J. Chem. Phys.*, 139(8):084201, 2013.

[49] D. J. Mothersole, P. J. Jackson, C. Vasilev, J. D. Tucker, A. A. Brindley, M. J. Dickman, and C. N. Hunter. PucC and LhaA direct efficient assembly of the light-harvesting complexes in *Rhodobacter sphaeroides*. *Mol. Microbiol.*, 99:307–327, 2016.

[50] P. D. Dahlberg, P.-C. Ting, S. C. Massey, E. C. Martin, C. N. Hunter, and G. S. Engel. Electronic structure and dynamics of higher-lying excited states in light harvesting complex 1 from *Rhodobacter sphaeroides*. *J. Phys. Chem. A*, 120:4124–4130, 2016.

[51] P. L. Houston. *Chemical Kinetics and Reaction Dynamics*. Dover Publications, Inc., Mineola, NY, 2001.

[52] G. D. Scholes, I. R. Gould, R. J. Cogdell, and G. R. Fleming. Ab initio molecular orbital calculations of electronic couplings in the LH2 bacterial light-harvesting complex of *Rps. acidophila*. *J. Phys. Chem. B*, 103:2453–2553, 1999.

[53] V. Novoderezhkin and R. van Grondelle. Physical origins and models of energy transfer in photosynthetic light harvesting. *Phys. Chem. Chem. Phys.*, 12:7352–7365, 2010.

[54] V. I. Novoderezhkin, E. G. Andrizhiyevskaya, J. P. Dekker, and R. van Grondelle. Pathways and timescales of primary charge separation in the photosystem II reaction center as revealed by a simultaneous fit of time-resolved fluorescence and transient absorption. *Biophys. J.*, 89:1464–1481, 2005.

[55] M. Yang and G. R. Fleming. Influence of phonons on exciton transfer dynamics: comparison of the Redfield, Forster, and modified Redfield equations. *Chem. Phys.*, 275:355–372, 2002.

[56] W. M. Zhang, T. Meier, V. Chernyak, and S. Mukamel. Exciton-migration and three-pulse femtosecond optical spectroscopies of photosynthetic antenna complexes. *The Journal of Chemical Physics*, 108:7763–7774, 1998.

[57] S. Mukamel. *Principles of Nonlinear Optical Spectroscopy.* Oxford University Press: New York, Oxford, 1995.

[58] O. Rancova and D. Abramavicius. Static and dynamic disorder in bacterial light-harvesting complex LH2: A 2DES simulation study. *J. Phys. Chem. B*, 118:7533–7540, 2014.

[59] G. D. Scholes and G. R. Fleming. On the mechanism of light harvesting in photosynthetic purple bacteria: B800 to B850 energy transfer. *J. Phys. Chem. B*, 104:1854–1868, 2000.

CHAPTER 4

ROLE OF CAROTENOIDS IN LH2 ENERGY TRANSFER PATHWAYS

The carotenoid S_1 state has been implicated in photosynthetic energy transfer and photoprotection, but the full scope of its role in energy transfer is not well understood. In the bacterial light-harvesting complex 2, anaerobically grown cultures of *Rhodobacter sphaeroides* incorporate the carotenoid spheroidene, while semi-aerobically grown cultures incorporate spheroidenone. This alteration of the carotenoid increases the conjugation length and lowers the energy of the S_2 and S_1 states. I hypothesized that the adaptation would sufficiently lower the energy level of the S_1 state below the bacteriochlorophyll Q_y state to reverse the flow of energy between the S_1 and Q_y states, introducing an energy-quenching pathway in LH2 from semi-aerobically grown cells. However, the results of this experiment show consistent Q_y lifetimes between complexes isolated from anaerobically and semi-aerobically grown cells.

4.1 A Carotenoid Switch in LH2

In the peripheral light harvesting complex 2 (LH2) from *Rhodobacter sphaeroides* (*Rba. sphaeroides*), carotenoid molecules span and connect the B800 and B850 rings of bacteriochlorophyll (BChl). Each of the nine subunits consists of an α/β peptide heterodimer, three bacteriochlorophyll *a* (BChl), and one carotenoid. [1] The carotenoids lie 3.4 – 3.7 Å from both BChl rings, allowing for exciton coupling and energy transfer between the carotenoid and its adjacent BChls. [2] Excitons can relax from the carotenoid S_2 state to the dark S_1 via rapid internal conversion or transfer to the BChl Q_x or Q_y state on the femtosecond timescale. Energy transfers from the spheroidene S_2 state to the BChl Q_y with 57% efficiency and from the spheroidene S_1 state to the BChl Q_y with 82% efficiency. [3, 4] Carotenoids also support the structural integrity of the LH2 complex. The B800 ring of BChl is unable

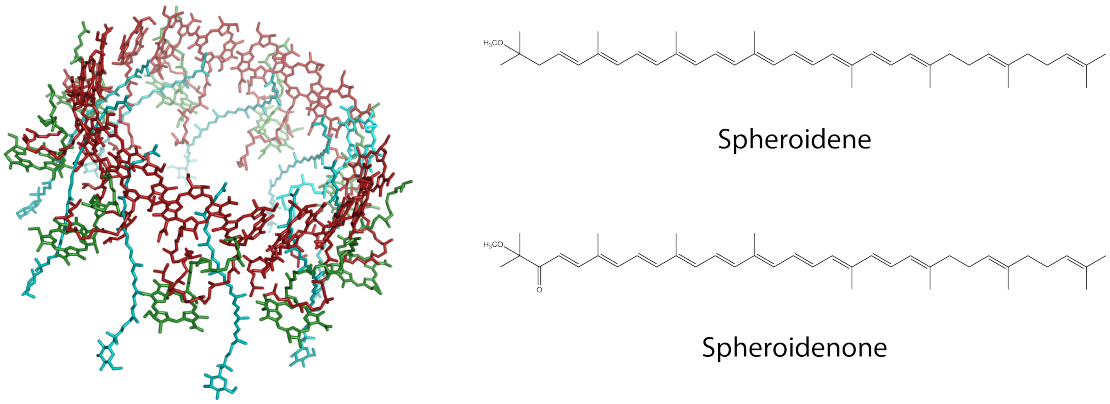

Figure 4.1: (left) The crystal structure of LH2 from *Rhodopseudomonas acidophila* (PDB ID: 1NKZ). [9] Carotenoids (blue) span the B800 (green) and B850 (red) rings of BChl *a*. (right) Molecular structures of the carotenoids (top) spheroidene incorporated in LH2 from *Rba. sphaeroides* under anaerobic growth conditions and (bottom) spheroidenone incorporated under semi-aerobic growth conditions.

to form in a carotenoidless LH2 mutant of *Rba. sphaeroides*. [5]

Additionally, carotenoids act as photoprotective quenchers for singlet oxygen and triplet BChl to prevent damage by reactive oxygen species. [6, 7] This class of molecules regulates energy transfer in higher plants through the Xanthophyll cycle. Under high illumination, a molecular switch from the carotenoid violaxanthin to zeaxanthin results in a reversible energy quenching pathway. [8]

In semi-aerobically grown *Rba. sphaeroides* (25 μM O_2), LH2 incorporates spheroidenone in place of sphaeroidene (Figure 4.1). Approximately 77% of the carotenoid molecules are replaced. [7] The addition of a keto group extends the effective conjugation length of the carotenoid, lowering the energies of its singlet excited states. [10–12] Figure 4.2 shows that the visually observed color of LH2 changes from green to purple with the change in carotenoid. A carotenoidless mutant of LH2 lacking both the carotenoids and the B800 ring of BChl is blue in color. Figure 4.2 also shows the linear absorbance spectra of each LH2 sample. The carotenoid S_2 absorbance red shifts with the change from spheroidene to spheroidenone and additionally lacks the sharp vibrational progression. The carotenoidless mutant does not

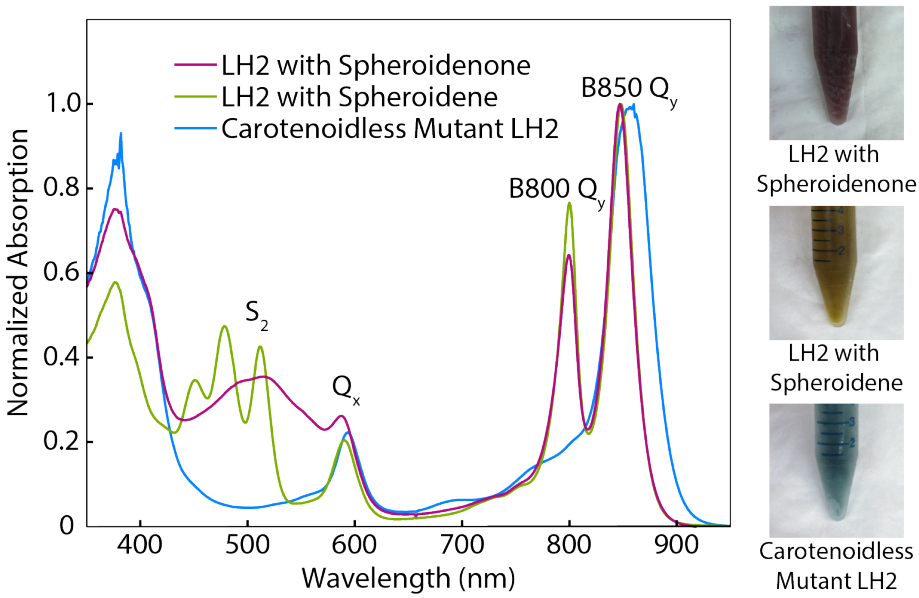

Figure 4.2: (left) Normalized linear absorbance spectra of LH2 isolated from (purple) semi-aerobically grown cells, (green) anaerobically grown cells, and (blue) a carotenoidless mutant strain. (right) Photographs of the corresponding LH2 samples isolated from (top) semi-aerobically grown cells, (middle) anaerobically grown cells, and (bottom) a carotenoidless mutant strain.

have absorbance peaks in the S_2 or B800 regions of the spectrum and has a broadened B850 absorbance feature.

I hypothesized that the carotenoid switch from spheroidene to spheroidenone would decrease the energy level of the S_1 state sufficiently to introduce an energy quenching pathway from Q_y to S_1. This quenching would decrease the Q_y lifetime of the B850 band, and possibly that of the B800 band as well. The Jablonski diagram in Figure 4.3 shows the hypothesized pathways following direct excitation of the B800 and B850 Q_y bands. The incorporation of spheroidenone into LH2 would result in some energy transfer from the Q_y to S_1 states, which would then nonradiatively relax down to the ground state.

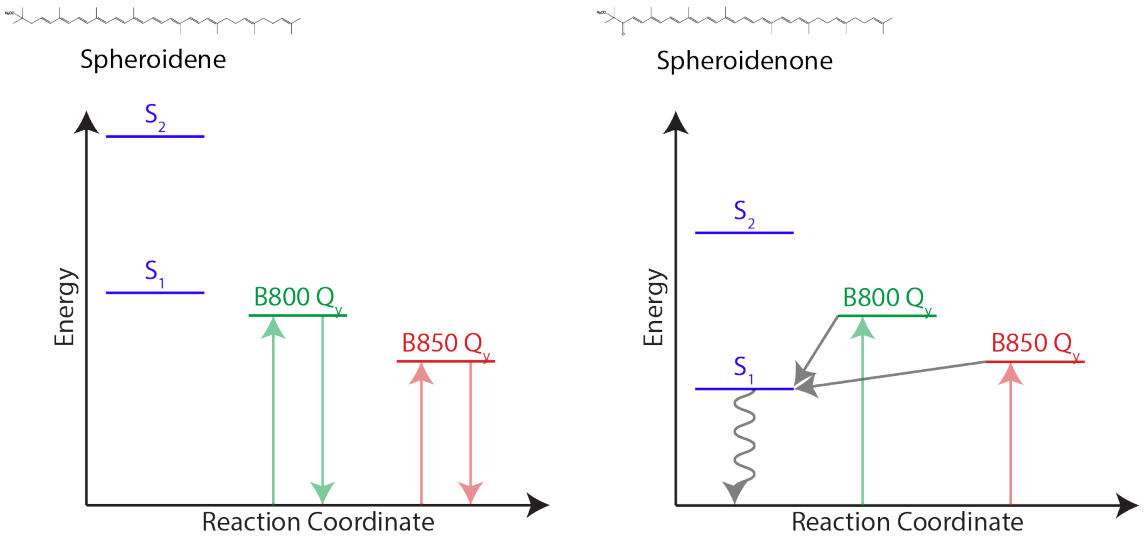

Figure 4.3: Jablonski diagrams showing hypothesized energy pathways for LH2 with (left) spheroidene from anaerobically grown cells or (right) spheroidenone from semi-aerobically grown cells.

4.2 Two-Dimensional Electronic Spectroscopy of Isolated LH2

We collected two-dimensional electronic spectra of anaerobic, semi-aerobic, and carotenoidless LH2, simultaneously exciting the B800 and B850 Q_y bands to observe the lifetimes and dynamics of these features. In short times datasets, waiting times ranged from -500 - 2750 fs, and in long times datasets, waiting times included 10 points evenly log spaced from 1 - 400 ps: 1, 2, 4, 7, 14, 28, 54, 106, 206, and 400 ps. Long times data collection involved a slow scan of 1000 frames centered around each waiting time point which were then averaged for that single time point. Absolute valued 2DES spectra and short and long times waiting time traces from each sample are presented in Figure 4.4. Anaerobic, semi-aerobic, and carotenoidless LH2 all show similar short times decay dynamics of the B850 feature. The carotenoidless mutant lacks the B800 diagonal feature and B800-B850 crosspeak since it does not assemble the B800 ring of chromophores.

The short waiting times (0 - 2750 fs) dynamics of anaerobic and semi-aerobic LH2 appear to be very similar. The longer decay constant in the short waiting times data is likely due to singlet-singlet annihilation, which is discussed in Chapter 5. We would expect more

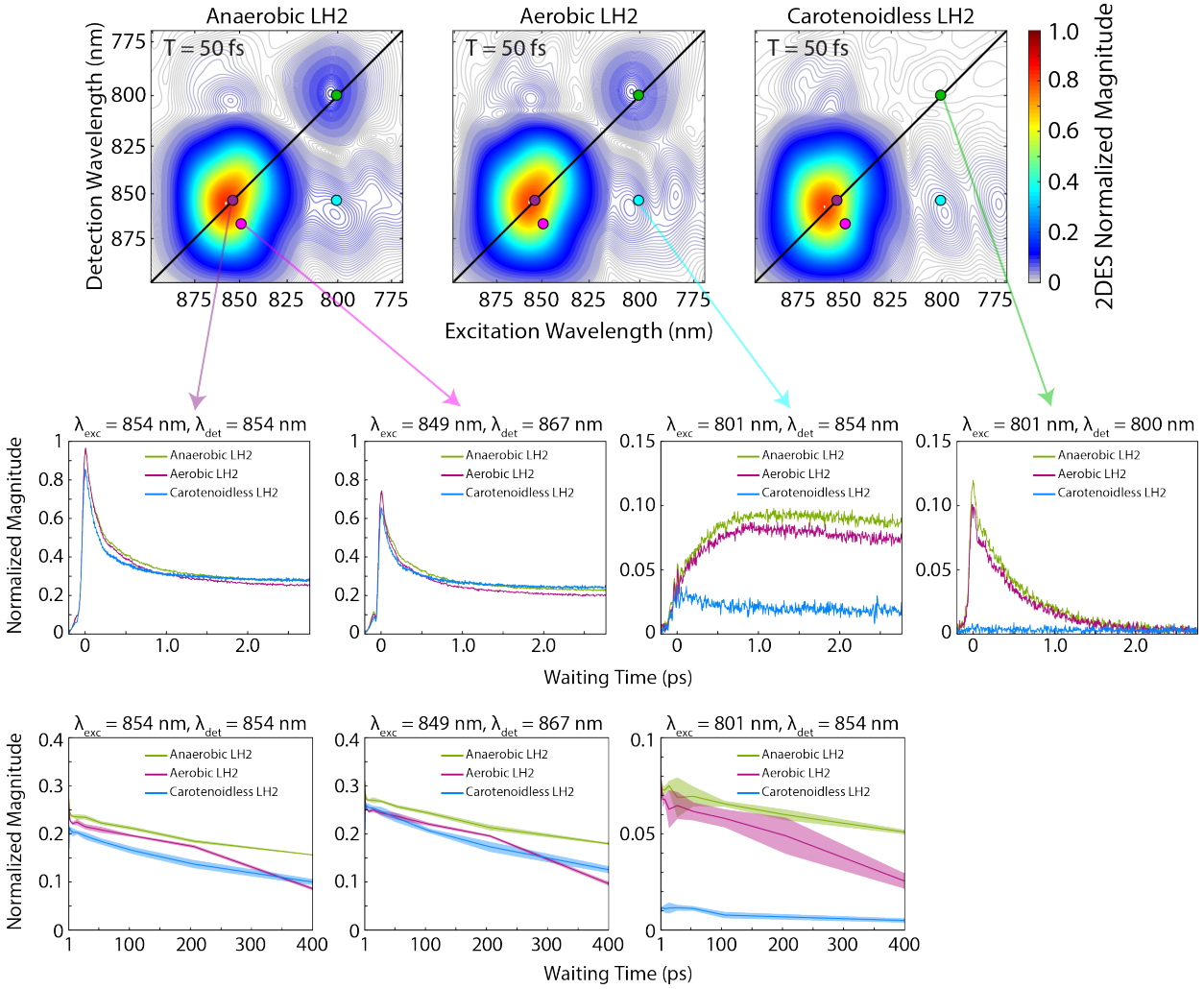

Figure 4.4: (top) Absolute valued 2DES spectra of isolated LH2 from (left) anaerobically grown cells, (center) semi-aerobically grown cells, and (right) carotenoidless mutant. (middle) Short times (0 - 2500 fs) and (bottom) Long times (1 - 400 ps) waiting time traces from the indicated points on the 2D spectrum: $\lambda_{exc} = 854$ nm, $\lambda_{det} = 854$ nm (purple), $\lambda_{exc} = 849$ nm, $\lambda_{det} = 867$ nm (pink), $\lambda_{exc} = 801$ nm, $\lambda_{det} = 854$ nm (cyan), and $\lambda_{exc} = 801$ nm, $\lambda_{det} = 800$ nm (green). Waiting time traces show the time dependence of the 2DES signal magnitude of isolated LH2 from anaerobically grown cells (green), semi-aerobically grown cells (purple), and carotenoidless mutant (blue). For long times waiting time traces, shaded area indicates ± the standard error of the mean (σ) from five scans.

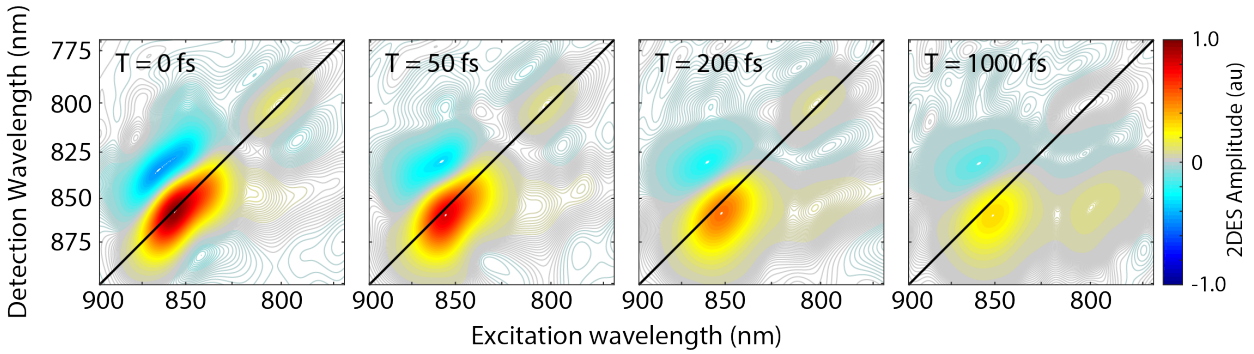

Figure 4.5: Rephasing 2DES spectra of isolated LH2 from anaerobically grown *Rba. sphaeroides* at waiting times of 0, 50, 200, and 1000 fs.

pronounced differences in the B850 lifetime on the tens to hundreds of picoseconds timescale if the spheroidenone S_1 state opened up an energy quenching pathway in semi-aerobic LH2. The waiting time dynamics of anaerobic and semi-aerobic LH2 appear to be very similar up to 200 ps. A deviation between the two samples is only apparent in the final waiting time data point of 400 ps.

A waiting time series of rephasing 2DES spectra of anaerobic LH2 is shown in Figure 4.5. These data were phased by fitting to separately acquired pump-probe spectra according to the projection slice theorem. A phase roll in the aerobic LH2 spectra over the course of the experiment prohibited accurate phasing of these data. These data were collected and processed before improvements were made to the GRAPES data acquisition and processing to produce fully absorptive 2DES spectra as discussed in Section 2.1.2. [13] As a result, the phased spectra show a diagonally elongated phase twist consistent with rephasing spectra.

4.3 Path Forward: Two-Color 2DES

The preliminary dataset presented here does not provide convincing evidence of an energy quenching pathway from BChl via the carotenoid S_1 state. These experiments could be improved upon in the current experimental setup with broader bandwidth, finer sampling of long waiting times, reduced power to eliminate annihilation effects, and processed to produce fully absorptive spectra. We have isolated LH2 samples from both anaerobic and semi-

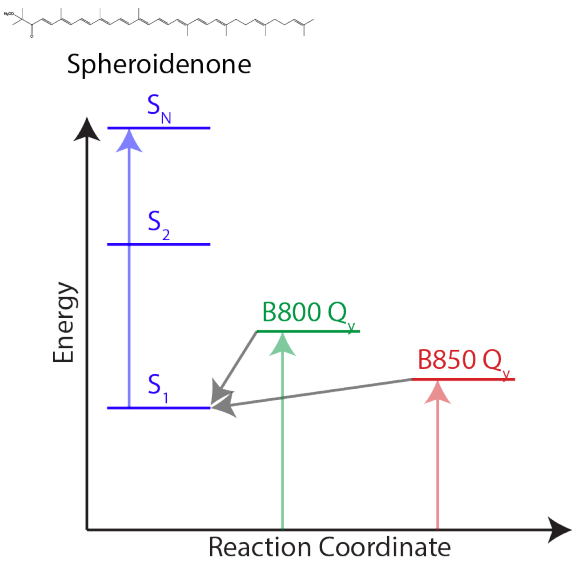

Figure 4.6: Jablonski diagram showing hypothesized energy pathways for LH2 with spheroidenone from semi-aerobically grown cells with a two-color 2DES experiment directly exciting the BChl Q_y bands and probing the spheroidenone S_1 to S_N transition.

aerobically grown cells. Other members of the Engel group are developing two-color pump-probe and 2DES experiments that would permit direct interrogation of the ESA transition from the carotenoid S_1 to S_N to probe energy transfer from the BChl Q_y to carotenoid S_1. Figure 4.6 shows a Jablonski diagram illustrating this energy path. The S_1 to S_N ESA energy gap is believed to be near 600 nm. Broadband excitation around 850 nm and detection around 600 nm resulting in an ESA pathway in semi-aerobic LH2 but not anaerobic LH2 would provide conclusive evidence of a quenching pathway introduced by the carotenoid switch.

REFERENCES

[1] V. Sundstrom and T. Pullerits. Photosynthetic light-harvesting: Reconciling dynamics and structure of purple bacterial LH2 reveals function of photosynthetic unit. *J. Phys. Chem. B*, 103:2327–2346, 1999.

[2] R. E. Blankenship. *Molecular Mechanisms of Photosynthesis*. John Wiley & Sons, Ltd, Chichester, West Sussex, 2nd edition, 2014.

[3] T. Polivka, T. Pullerits, H. A. Frank, R. J. Cogdell, and V. Sundstrom. Ultrafast formation of a carotenoid radical in LH2 antenna complexes of purple bacteria. *J. Phys. Chem. B*, 108:15398–15407, 2004.

[4] J. P. Zhang, R. Fujii, P. Qian, T. Inaba, T. Mizoguchi, Y. Koyama, K. Onaka, and Y. Watanabe. Mechanism of the carotenoid-to-bacteriochlorophyll energy transfer via the S1 state in the LH2 complexes from purple bacteria. *J. Phys. Chem. B*, 104:3683–3691, 2000.

[5] T. Polivka and V. Sundstrom. Ultrafast dynamics of carotenoid excited states - from solution to natural and artificial systems. *Chem. Rev.*, 104:2021–2071, 2004.

[6] H. A. Frank and R. J. Cogdell. The photochemistry and function of carotenoids in photosynthesis. In A. Young and G. Britton, editors, *Carotenoids in Photosynthesis*. Chapman and Hall, London, UK, 1993.

[7] J. Glaeser and G. Klug. Photo-oxidative stress in *Rhodobacter sphaeroides*: Protective role of carotenoids and expression of selected genes. *Microbiology*, 151:1927–1938, 2005.

[8] K. K. Niyogi and T. B. Truong. Evolution of flexible non-photochemical quenching mechanisms that regulate light harvesting in oxygenic photosynthesis. *Curr. Opin. Plant Biol.*, 16(3):307–314, 2013.

[9] M. Z. Papiz, S. M. Prince, T. Howard, R. J. Cogdell, and N. W. Isaacs. The structure and thermal motion of the B800–850 LH2 complex from *Rps. acidophila* at 2.0Å resolution and 100K: New structural features and functionally relevant motions. *J. Mol. Biol.*, 326:1523–1538, 2003.

[10] V. Slouf, P. Chabera, J. D. Olsen, E. C. Martin, P. Qian, C. N. Hunter, and T. Polivka. Photoprotection in a purple phototrophic bacterium mediated by oxygen-dependent alteration of carotenoid excited-state properties. *Proc. Natl. Acad. Sci. USA*, 109(22):8570–8575, 2012.

[11] D. Kosumi, S. Maruta, R. Fujii, M. Sugisaki, S. Takaichi, R. J. Cogdell, and H. Hashimoto. A regulation of energy flow in purple bacterial photosynthetic antennas. In *Ultrafast Phenomena*, 2014.

[12] S. Maruta, D. Kosumi, T. Horibe, R. Fujii, M. Sugisaki, R. J. Cogdell, and H. Hashimoto. The dependence of excitation energy transfer pathways on conjugation length of carotenoids in purple bacterial photosynthetic antennae. *Phys. Status Solidi B*, 248(2):403–407, 2011.

[13] S. H. Sohail, P. D. Dahlberg, M. A. Allodi, S. C. Massey, P.-C. Ting, E. C. Martin, C. N. Hunter, and G. S. Engel. Communication: Broad manifold of excitonic states in light-harvesting complex 1 promotes efficient unidirectional energy transfer *in vivo*. *J. Chem. Phys.*, 147:131101, 2017.

CHAPTER 5

POWER DEPENDENT DYNAMICS AND ANNIHILATION IN ISOLATED AND MEMBRANE-BOUND LH2

Photosynthetic organisms use extended networks of light-harvesting antennae to absorb solar energy. The energy then must be transferred through the antenna network from the site of absorption to the reaction center where electron transfer reactions occur. We previously mapped out the path of excitation energy transfer through these antenna networks *in vivo* in the purple bacterium *Rhodobacter sphaeroides*. [1] To recover the inter-complex hopping times, we exploited singlet-singlet annihilation dynamics at high excitation fluences. We initially believed that annihilation dynamics would only be observed in membrane fragments or whole cells because the light-harvesting complexes are held in close contact by the membrane environment, permitting excitations to migrate through the network and annihilate. However, power dependence studies of isolated light harvesting complex 2 (LH2) reveal annihilation in isolated complexes that have been purified and resuspended in detergent micelles. These dynamics reveal new insight into the isolated LH2 ultrafast dynamics literature.

5.1 Energy Transfer in *Rhodobacter sphaeroides*

5.1.1 Intra-Complex Energy Transfer

The light-harvesting apparatus in *Rhodobacter sphaeroides* (*Rba. sphaeroides*) consists of the peripheral antenna light-harvesting complex 2 (LH2), the core antenna light-harvesting complex 1 (LH1), and the reaction center (RC) which is associated with LH1. [2] Within LH2, there are two rings of bacteriochlorophyll *a* (BChl *a*) pigments, B800 and B850, with peak absorbances at 800 nm and 850 nm, respectively. [3] Both rings serve as primary light absorbers, and energy can additionally flow downhill from B800 to B850 on the 700-800 fs timescale. [4–6] LH1 is an S-shaped dimer aggregate of BChl with a peak absorbance at

875 nm. Each RC is encircled by an LH1 monomer. The RC special pair BChl have an absorbance peak at 870 nm.

5.1.2 Inter-Complex Energy Transfer

Energy moves between the antenna complexes on a picosecond timescale. Previous work conducted on *Rba. sphaeroides* membrane fragments revealed energy transfer from LH2 B850 to LH1 B875 in 3-5 ps at room temperature. [4, 7, 8] The uphill energy transfer step from LH1 to the RC occurred in 35 ps. [8, 9] In reference [1], we mapped out the timescales of energy transfer through the light-harvesting network as well as the number of energy transfer events to determine the fate of absorbed excitons. These energy transfer time constants, shown in Figure 1.2, are in reasonable agreement with the prior literature. We measured a hopping time of 4.8 ± 0.2 ps from LH2 to LH1 and 49 ± 3 ps from LH1 to the RC. We were additionally able to recover energy transfer times between isoenergetic complexes. LH2 to LH2 energy transfer takes place in 2.7 ± 0.1 ps and LH1 to LH1 energy transfer occurs in 4.7 ± 0.2 ps. [1]

At high excitation fluences, multiple excitations are produced in a given aggregate of light-harvesting complexes. Each excitation migrates through the two-dimensional membrane network of complexes with a complex-to-complex hopping time, τ_{hop}. When the excitations migrate to be within a given reaction radius, singlet-singlet annihilation reduces the number of excitations from 2 to 1. In a kinetic model assumed here, by which the size of the aggregate is larger than the diffusion length of excitations, the time-dependent number of excitations in the aggregate, $n(T)$ is given by Equation 5.1. [12]

$$n(T) = \frac{n_0 \exp(-T/\tau)}{1 + (n_0/2)\int_0^T \gamma(T')\exp(-T'/\tau)\mathrm{d}T'} \tag{5.1}$$

where n_0 is the initial number of excitations in the aggregate and γ is the time-dependent rate of singlet-singlet annihilation given by Equation 5.2. [10, 12] α is related to the fractal

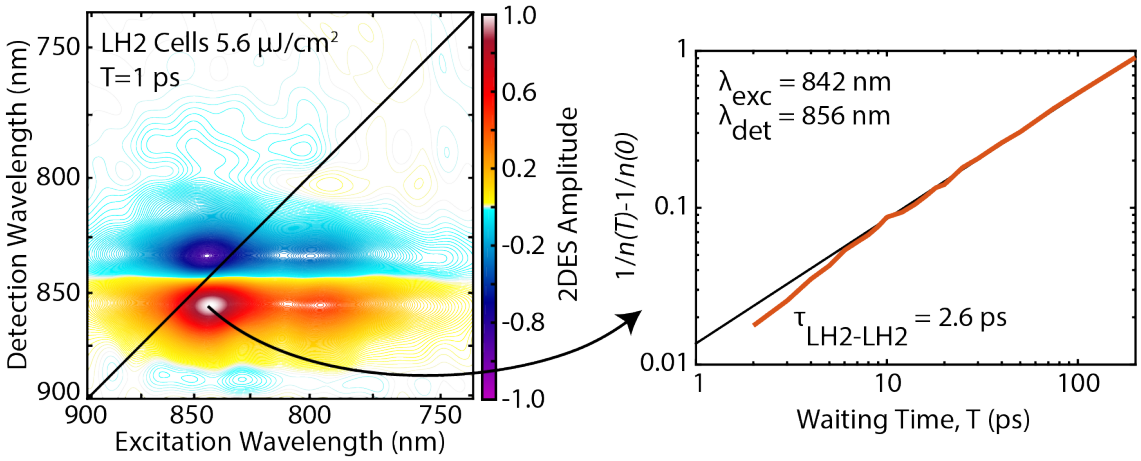

Figure 5.1: (left) Absorptive 2DES spectrum of LH2-only *Rba. sphaeroides* cells at waiting time 1 ps collected at 5.6 μJ/cm^2. (right) Log-scale plot of $\left(\frac{1}{n(T)} - \frac{1}{n(0)}\right)$ versus T where $n(T)$ is the 2DES signal at waiting time T from the spectral point $\lambda_{exc} = 842$ nm, $\lambda_{det} = 856$ nm, indicated by the black arrow. A linear fit at this point on the 2D spectrum gives an LH2-LH2 hopping time of 2.6 ps. Figure adapted from Reference [1] under the Creative Commons license https://creativecommons.org/licenses/by/4.0/legalcode.

dimension, d_s, by Equation 5.3.

$$\gamma(T) = \frac{\gamma_0}{T^\alpha} \tag{5.2}$$

$$\begin{aligned} \alpha &= 1 - \frac{d_s}{2} \qquad \text{if} \quad d_s < 2 \\ \alpha &= 0 \qquad\qquad\quad \text{if} \quad d_s \geq 2 \end{aligned} \tag{5.3}$$

where d_s describes the excitation diffusion path through a spectrally inhomogeneous two-dimensional photosynthetic membrane. [1, 10–12] A perfect two-dimensional lattice would yield $d_s = 2$ and $\alpha = 0$ due to a nonfractal structure, removing the time-dependence of the annihilation rate in Equation 5.2. [10] However, the introduction of spectral inhomogeneity introduces fractal structure affecting the path that excitations can travel through the membrane and yielding $d_s < 2$. [10] In this fractal structure model, excitations move only through the low-energy sites in the energetically inhomogeneous array. In Reference [1], we typically recovered values of ∼1.8 for d_s reflecting some degree of fractal structure. [1] The parameter

γ_0 is directly related to the inter-complex excitation hopping time, τ_{hop}, by Equation 5.4.

$$2\gamma_0^{-1} = 0.5Nf_d(N)\tau_{hop} \tag{5.4}$$

N is the number of connected complexes, and $f_d(N)$ is a packing factor. [11, 12] For *Rba. sphaeroides*, we assume the complex packing to fall between square lattice ($f_d = 0.8$) and hexagonal close packing ($f_d = 0.6$) giving $f_d = 0.7$. [1] Combining equations 5.1 and 5.2 for short-time kinetics, the 2DES signal at a given waiting time $n(T)$ is calculated from the annihilation rate by Equation 5.5. [12]

$$\log\left(\frac{1}{n(T)} - \frac{1}{n(0)}\right) = (1-\alpha)\log(T) + \log\left(\frac{\gamma_0/2}{1-\alpha}\right) \tag{5.5}$$

The 2DES signal $n(T)$ and $n(0)$ is scaled by the average number of excited complexes based on a given pump fluence. The parameter γ_0 and hopping time τ_{hop} can be recovered from any pump fluence in the annihilation regime. Figure 5.1 shows the linear fit of Equation 5.5 to the log-scale plot of 2DES signal from LH2-only cells used to fit the parameters α and γ_0 to determine the LH2-LH2 hopping time τ_{hop}.

5.2 Power Dependence of 2DES Signal in Isolated and Membrane-Bound LH2

Singlet-singlet annihilation results in power dependent 2DES dynamics. At higher fluences, there are a greater density of excitations. As those excitations migrate through the photosynthetic complex network, they risk meeting and annihilating, reducing the number of measured excitations from 2 to 1. Therefore, shorter lifetimes are observed at higher pulse powers in the presence of annihilation. Figure 5.2 shows power-dependent dynamics of the LH2 B850 feature at long waiting times (1 ps - 1 ns) of isolated LH2 and LH2-only membranes. These pump fluences correspond to excitation densities from 1 excitation per 81 LH2 (16 μW) to 1 excitation per 3.3 LH2 (394 μW). Both the isolated and membrane samples

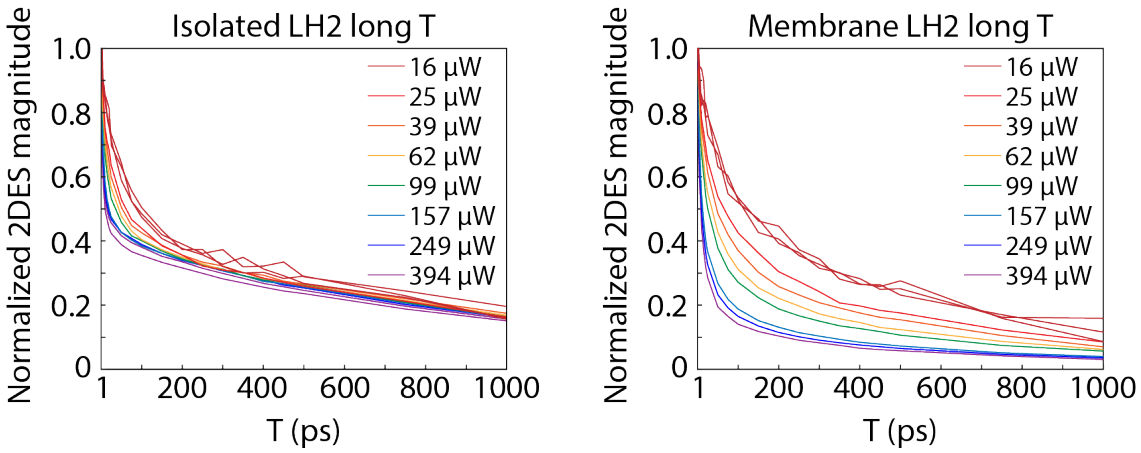

Figure 5.2: Long waiting times (1 ps - 1 ns) power dependent dynamics of the LH2 B850 signal in (left) isolated LH2 and (right) LH2-only membranes. Pulse powers range from 16 μW - 394 μW, corresponding to 1 in every 81 LH2 excited at the lowest power to 1 in every 3.3 LH2 excited at the highest power. Three replicates are shown for the 16 μW measurement. We observe shorter lifetimes with higher fluence in both samples.

show shorter lifetimes at higher power, though the effect in LH2-only membranes is much more pronounced. These dynamics are expected for LH2-only membranes as the complexes are held in close connectivity in the membrane environment. However, we find the isolated LH2 power dependent dynamics to be surprising since the purified complexes are suspended in detergent micelles. These results indicate that multiple LH2 complexes may be present in each micelle and are held in close enough proximity to permit hopping between complexes. In isolated LH2, the power dependent dynamics occur within the first 200 ps, whereas the power dependence in LH2-only membranes persists until 1 ns. This time dependence reflects the longer-range order of LH2 in the membrane environment. If only a few complexes are present in the detergent micelles, only a small number of inter-complex hops will be required to annihilate excess excitations. The fractal dimension and packing factor would vary in the isolated LH2 case because the complexes are not constrained to a two-dimensional membrane scaffold.

In addition to the long waiting times power dependent dynamics, we also observed power dependent dynamics indicative of annihilation at short times (Figure 5.3). Both isolated and membrane-bound LH2 samples show similar power dependent dynamics. At low excitation

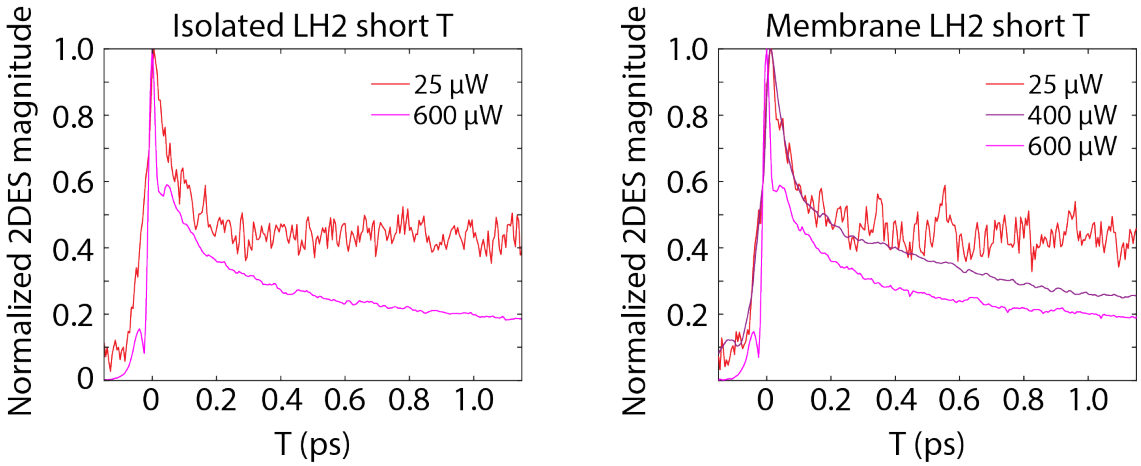

Figure 5.3: Short waiting times (0 - 1150 fs) power dependent dynamics of the LH2 B850 signal in (left) isolated LH2 at pulse powers of 25 μW (1 in every 52 LH2 excited) and 600 μW (1 in every 2.2 LH2 excited) and (right) LH2-only membranes at pulse powers of 25 μW (1 in every 52 LH2 excited), 400 μW (1 in every 3.3 LH2 excited), and 600 μW (1 in every 2.2 LH2 excited). The decay from 150-1150 fs in the higher fluences is absent in the lowest fluence.

power, the slow decay from 150-1000 fs disappears. These slow B850 decay dynamics have been reported previously in pump-probe and transient grating experiments [13–15] and attributed to solvation dynamics. [13] I propose that these power-dependent decay dynamics are due to singlet-singlet annihilation which may arise from intra-complex transfer in the event of excitations on both the B800 and B850 rings of the same LH2 complex.

5.3 Short Waiting Times Annihilation Dynamics

If the power dependent dynamics observed from 150-1000 fs are consistent with a kinetic model of singlet-singlet annihilation, the log-log plot of $\left(\frac{1}{n(T)} - \frac{1}{n(0)}\right)$ versus T should be linear. [1, 12] Figure 5.4 shows the log-log plots of B850 dynamics from absorptive 2DES spectra of isolated LH2 and LH2-only membranes. The red lines show a fit to Equation 5.6 to recover the parameters γ_0 and α, which is a different representation of Equation 5.5. [12]

$$\frac{1}{n(T)} - \frac{1}{n(0)} = \frac{\gamma_0/2}{1-\alpha} T^{1-\alpha} \tag{5.6}$$

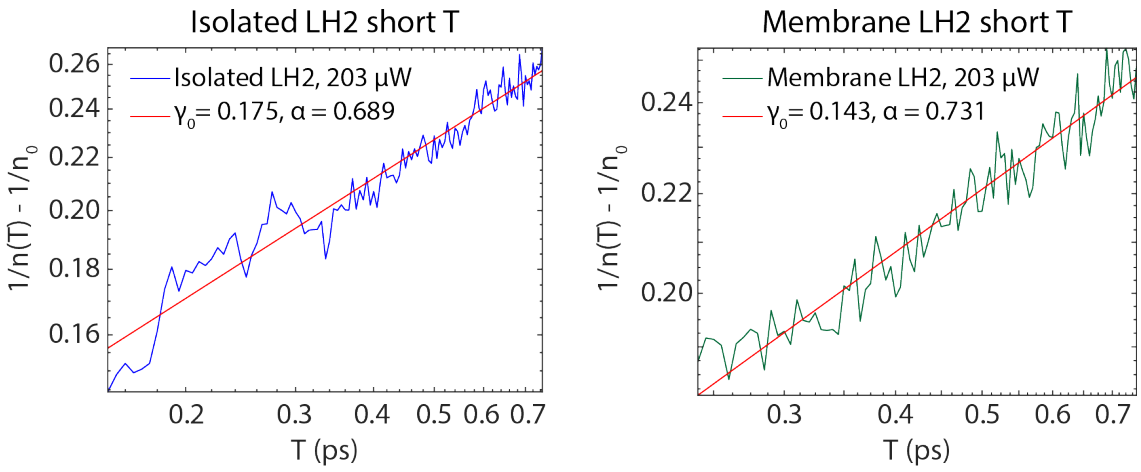

Figure 5.4: Short waiting times (150 - 740 fs) annihilation dynamics of the LH2 B850 signal in (left) isolated LH2 and (right) LH2-only membranes at a pulse power of 220 μW (1 in every 5.9 LH2 excited).

It should be noted that $n(0)$ is a function of the domain size, N, which in this case was set to $N = 50$. This domain size parameter can be set arbitrarily as it cancels out in calculating the hopping time, τ_{hop} according to Equation 5.4. The log-log plots shown in Figure 5.4 give a linear fit with similar annihilation rates and α parameters for both the isolated and membrane-bound LH2 samples. Assuming a packing factor $F_d(N) = 0.7$ following Reference [1], we recover hopping times of 650 fs in isolated LH2 and 800 fs in LH2-only membranes. These timescales are consistent with energy transfer from B800 to B850, suggesting annihilation due to intra-complex energy transfer between these two rings. However, the assignment of the packing factor $F_d(N)$ should be further analyzed to consider the appropriate description of the B800-B850 interaction. The assumption made here considers the two-dimensional packing of LH2 complexes in the photosynthetic membrane, which lies between a square lattice and hexagonal close packing, and may not be an appropriate descriptor of the intra-complex chromophore arrangement.

5.4 Conclusions

We observe power-dependent dynamics at short waiting times (150 - 1000 fs) in both isolated LH2 and LH2-only membranes that sheds new light on the the previously reported slow timescale decay of the B850 dynamics. We propose that these power-dependent dynamics are instead due to singlet-singlet annihilation arising from intra-complex energy transfer between the B800 and B850 rings of LH2. We additionally report slower power-dependent dynamics at long times which indicate inter-complex energy transfer between multiple isolated LH2 complexes in a detergent micelle. These observations have implications for modeling of LH2 excitonic dynamics, revising the earlier picture of the B850 dynamics.

REFERENCES

[1] P. D. Dahlberg, P.-C. Ting, S. C. Massey, M. A. Allodi, E. C. Martin, C. N. Hunter, and G. S. Engel. Mapping the ultrafast flow of harvested solar energy in living photosynthetic cells. *Nat. Commun.*, 8:988–994, 2017.

[2] R. E. Blankenship. *Molecular Mechanisms of Photosynthesis*. John Wiley & Sons, Ltd, Chichester, West Sussex, 2nd edition, 2014.

[3] M. Z. Papiz, S. M. Prince, T. Howard, R. J. Cogdell, and N. W. Isaacs. The structure and thermal motion of the B800–850 LH2 complex from *Rps. acidophila* at 2.0Å resolution and 100K: New structural features and functionally relevant motions. *J. Mol. Biol.*, 326:1523–1538, 2003.

[4] S. Hess, E. Akesson, R. J. Cogdell, T. Pullerits, and V. Sundstrom. Energy transfer in spectrally inhomogeneous light-harvesting pigment-protein complexes of purple bacteria. *Biophys. J.*, 69:2211–2225, 1995.

[5] T. H. Joo, Y. W. Jia, J. Y. Yu, D. M. Jonas, and G. R. Fleming. Dynamics in isolated bacterial light harvesting antenna (LH2) of *Rhodobacter sphaeroides* at room temperature. *J. Phys. Chem.*, 100:2399–2409, 1996.

[6] S. Hess, M. Chachisvilis, K. Timpmann, M. R. Jones, G. J. S. Fowler, C. N. Hunter, and V. Sundstrom. Temporally and spectrally resolved subpicosecond energy transfer within the peripheral antenna complex (LH2) and from LH2 to the core antenna complex in photosynthetic purple bacteria. *Proc. Natl. Acad. Sci. U.S.A.*, 92:12333–12337, 1995.

[7] V. Nagarajan and W. W. Parson. Excitation energy transfer between the B850 and B875 antenna complexes of *Rhodobacter sphaeroides*. *Biochemistry*, 36:2300–2306, 1997.

[8] V. Sundstrom, T. Pullerits, and R. van Grondelle. Photosynthetic light-harvesting: Reconciling dynamics and structure of purple bacterial LH2 reveals function of photosynthetic unit. *J. Phys. Chem. B*, 103:2327–2346, 1999.

[9] L. M. P. Beekman, F. van Mourik, M. R. Jones, H. M. Visser, C. N. Hunter, and R. van Grondelle. Trapping kinetics in mutants of the photosynthetic purple bacterium *Rhodobacter sphaeroides*: Influence of the charge separation rate and consequences for the rate-limiting step in the light-harvesting process. *Biochemistry*, 33:3143–3147, 1994.

[10] L. Valkunas, E. Akesson, T. Pullerits, and V. Sundstrom. Energy migration in the light-harvesting antenna of the photosynthetic bacterium *Rhodospirillum rubrum* studied by time-resolved excitation annihilation at 77 K. *Biophys. J.*, 70:2373–2379, 1996.

[11] H. van Amerongen, L. Valkunas, and R. van Grondelle. *Photosynthetic Excitons*. World Scientific Publishing Co. Pte. Ltd., Singapore, 2000.

[12] V. Barzda, V. Gulbinas, R. Kananavicius, V. Cervinskas, H. van Amerongen, R. van Grondelle, and L. Valkunas. Singlet-singlet annihilation kinetics in aggregates and trimers of LHCII. *Biophys. J.*, 80:2409–2421, 2001.

[13] L. D. Book, A. E. Ostafin, N. Ponomarenko, J. R. Norris, and N. F. Scherer. Exciton delocalization and initial dephasing dynamics of purple bacterial LH2. *J. Phys. Chem. B*, 104:8295–8307, 2000.

[14] M. Chachisvilis, O. Kuhn, T. Pullerits, and V. Sundstrom. Excitons in photosynthetic purple bacteria: Wavelike motion or incoherent hopping? *J. Phys. Chem. B*, 101:7275–7283, 1997.

[15] T. Pullerits, M. Chachisvilis, and V. Sundstrom. Exciton delocalization length in the B850 antenna of *Rhodobacter sphaeroides*. *J. Phys. Chem.*, 100:10787–10792, 1996.

CHAPTER 6

FOLLOWING ENERGY TRANSFER THROUGH CYANOBACTERIAL THYLAKOID MEMBRANES BY TWO-DIMENSIONAL ELECTRONIC SPECTROSCOPY

Cyanobacteria use light-harvesting antenna known as phycobilisomes to collect and funnel energy to the cyanobacterial photosystems where charge separation takes place. The phycobilisomes associate with both photosystem I (PSI) and photosystem II (PSII) and efficiently transfer energy to both photosystems. The cyanobacterial photosystems in the thylakoid membrane overlap spectrally with broad absorption peaks centered at 670 nm (PS II) and 680 nm (PS I). The light-harvesting machinery is made up of coupled pigments that are only slightly energetically distinct. This energetic funnel that allows for highly efficient energy transfer also frustrates analysis of live cells or intact membranes due to overlapping spectral features. We employ a series of mutant strains of *Synechocystis* sp that are null for either PSI or PSII along with the wild-type strain to disentangle the spectral contributions and dynamics of each fused antenna/reaction center complex in intact fragments of the thylakoid membrane. We also conduct a power dependence study to investigate inter-complex energy transfer between neighboring monomer units. Follow-up experiments will be necessary, using pump-probe to achieve higher excitation densities to observe annihilation by inter-complex energy transfer.

6.1 Energy Transfer in the Thylakoid Membrane

The cyanobacterial thylakoid membranes contain the fused antenna/reaction center complexes known as PSI and PSII. Peripheral light harvesting complexes, the PBS, sit atop the thylakoid membrane and funnel energy to both PSI and PSII. The PSI:PSII ratio ranges from 2:1 to 10:1. [1] Additionally, PSI monomers contain 96 Chl molecules while PSII monomers contain only 35 Chl molecules. [1–3]. As a result of the greater abundance of complexes and

higher Chl content per complex, PSI contributes much more strongly to the absorption in the 680 nm region of the spectrum.

PSI has an absorbance maximum at 680 nm and rapidly transfers energy to the P_{700} special pair Chl in the reaction center. However, P_{700} is not the lowest energy state in the PSI complex. PSI from *Synechocystis* sp PCC 6803 contains two sets of red Chl states with absorbance at 706 nm and 714 nm. [4, 5] The red Chl pools are believed to increase the absorption cross section with 280 cm^{-1} uphill energy transfer to P_{700}, on the order of kT. [5] This uphill energy transfer step is analogous to the 65 cm^{-1} uphill transfer from LH1 (875 nm) to the P_{870} RC in *Rhodobacter sphaeroides*. Experimental results from *Synechococcus elongatus* which have red Chl absorbance at 719 nm surprisingly show similar probability of charge separation with excitation wavelengths ranging up to 750 nm, an energy gap of 950 cm^{-1}. [6]

PSII has an absorbance maximum at 670 nm and funnels energy to its P_{680} reaction center, which contains four Chl a, two pheophytin a, and two β-carotene molecules. [2, 7] Subunit antennae of PSII CP47 and CP43 are the most proximal to P_{680}. [2, 8] It has been determined in 77 K experiments in *Thermosynechococcus vulcanus* (*T. vulcanus*) that CP43 is more strongly coupled to the PSII RC, while CP47 has a low-energy state that is more spatially separated from the PSII RC and may funnel excitations away from the PSII RC. [8] Two-dimensional electronic spectroscopy experiments on isolated PSII dimers from *T. vulcanus* at 77 K reveal three main diagonal features at 670 nm, 677 nm, and 683 nm with relaxation time constants as short as 60 fs. [9] This ultrafast energy transfer is a surprising result due to the relatively weak interchromophore couplings. The strongest couplings between Chl molecules in the CP43 and CP47 subunits are only 78 cm^{-1}. [8, 9] At room temperature, these rates would be even faster.

In the following experiments, we study the PSI and PSII energy transfer dynamics at physiological temperatures in the native membrane environment. The complexes are not only connected to other monomers from the same trimer or dimer, but may be energetically

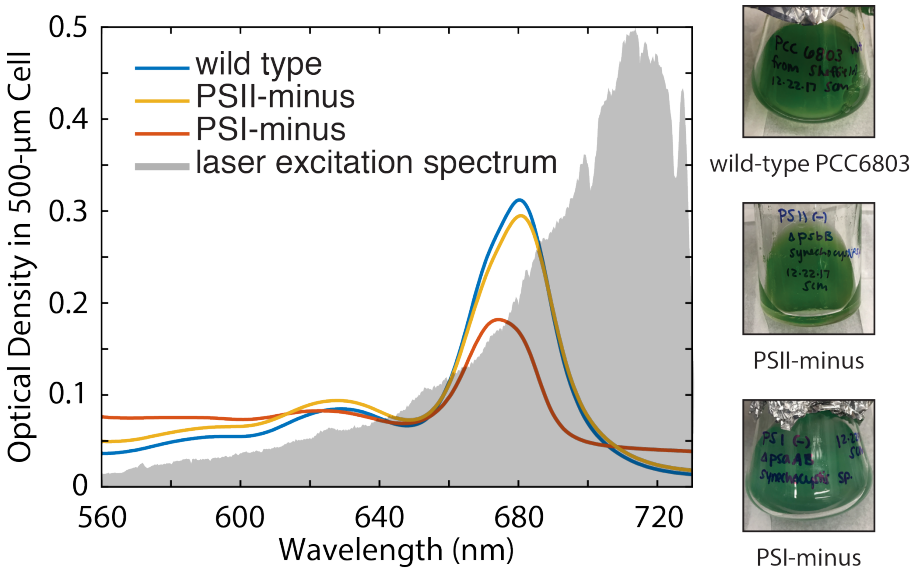

Figure 6.1: (left) Linear absorbance spectra of membrane fragments from wild-type (blue), PSII-minus (orange), and PSI-minus mutants (yellow) of *Synechocystis* sp PCC 6803 in a 500 μm path length and the laser excitation spectrum (gray shaded area) used in two-dimensional electronic spectroscopy (2DES) experiments. (right) Photographs of the corresponding *Synechocystis* sp cultures from (top) wild-type cells, (middle) PSII-minus cells, and (bottom) PSI-minus cells.

coupled to other nearby complexes in the thylakoid membrane. This disordered environment is more representative of the natural biological conditions than isolated complexes which have been purified and solubilized in detergents.

6.2 Disentangling Spectral Contributions of PSI and PSII

We use a wild-type sample along with mutant strains lacking one of the two photosystems to disentangle the spectral contributions of each complex. The strains used in this study are wild-type *Synechocystis* sp PCC 6803, a PSI-minus mutant (ΔpsaAB), and a PSII-minus mutant (ΔpsbB). Figure 6.1 shows the linear absorbance spectra of wild-type, PSI-minus, and PSII-minus *Synechocystis* sp membrane fragments, as well as the laser excitation spectrum used in 2DES experiments. Since the PBS fall off during the fragmentation process, we have also removed the spectral contributions of the PBS. The absorption maximum of the chlorophyll (Chl) Q_y band in wild-type *Synechocystis* sp PCC 6803 is centered at 680

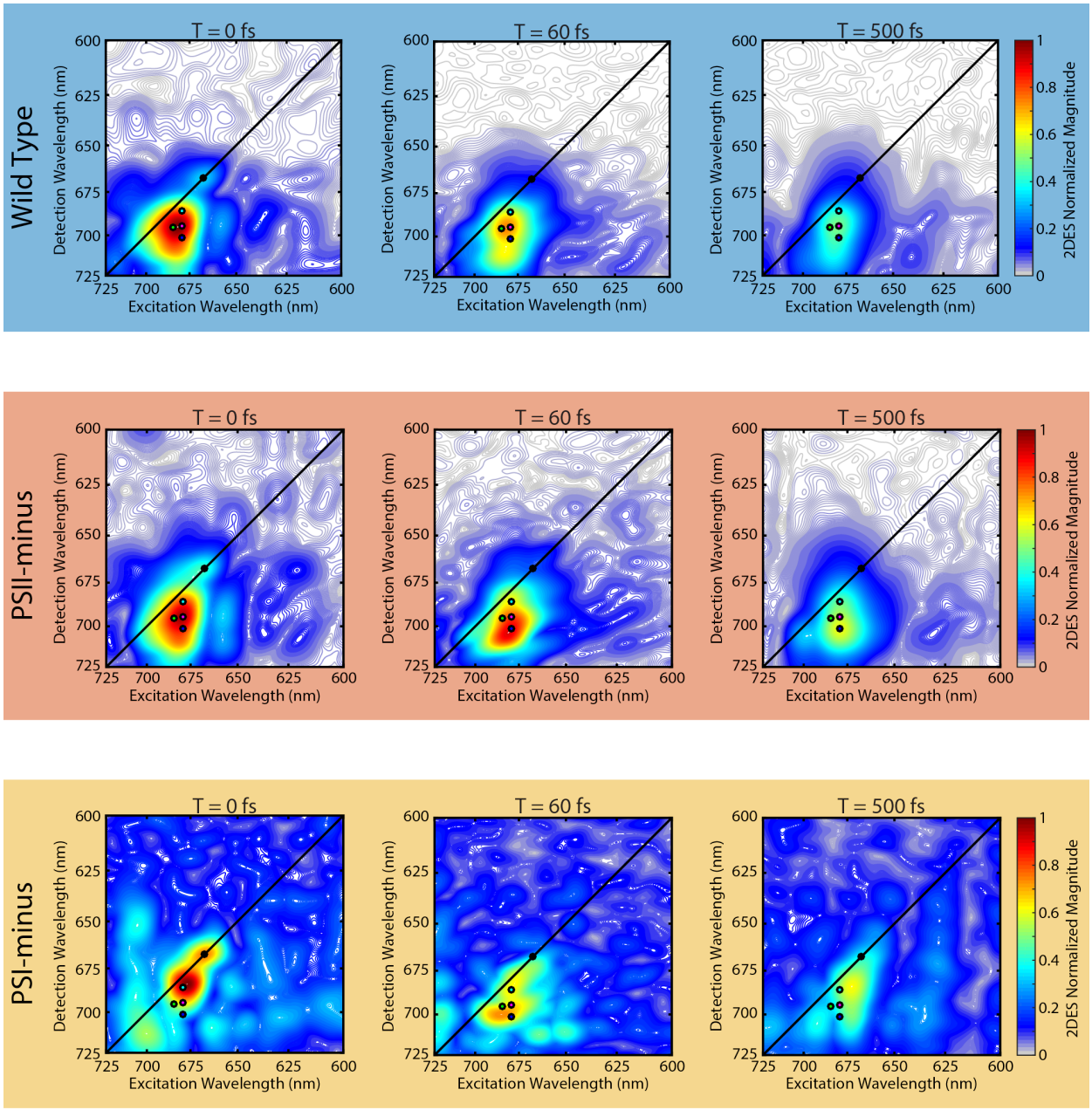

Figure 6.2: Normalized absolute valued two-dimensional electronic spectra of membrane fragments from *Synechocystis* sp PCC 6803 (top) wild-type, (middle) PSII-minus, and (bottom) PSI-minus cells at waiting times of 0, 60, and 500 fs. Spectra are shown as an average of three scans. Points indicate the spectral locations of the waiting time traces shown in Figure 6.3.

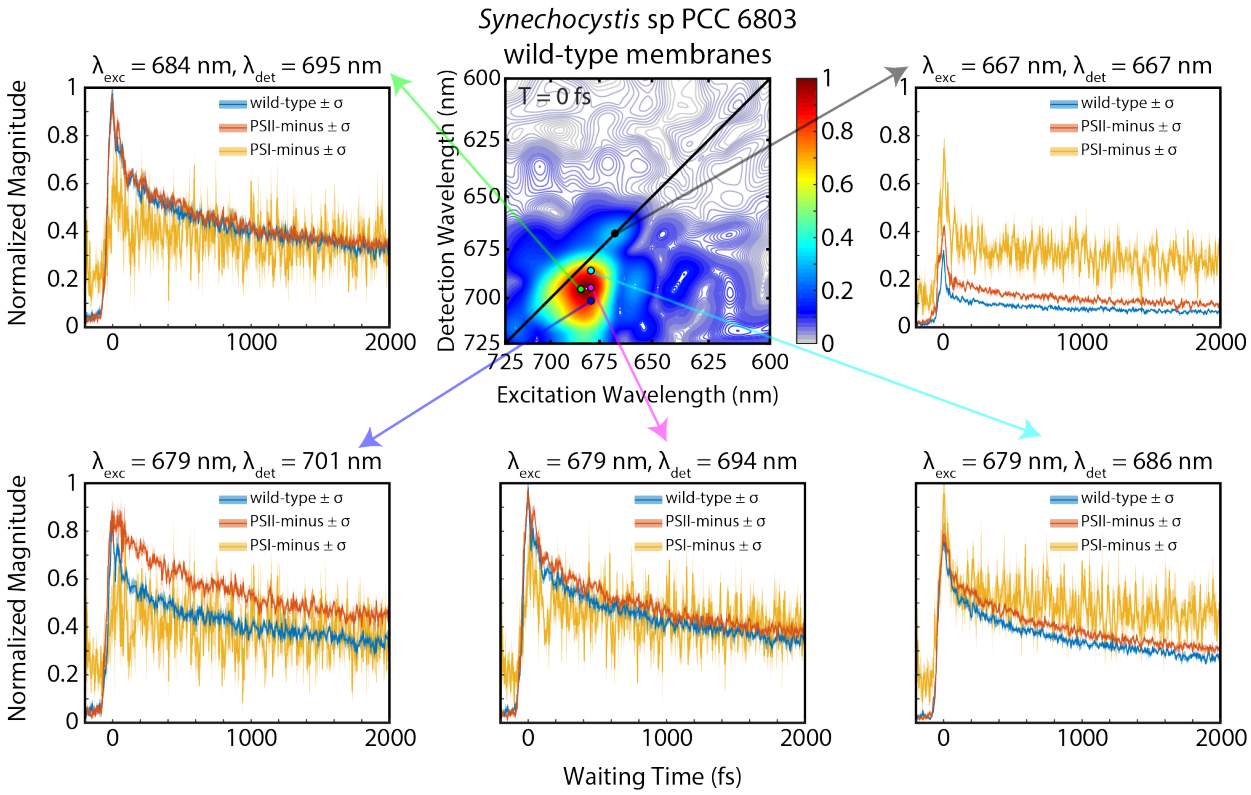

Figure 6.3: Waiting time traces from absolute valued 2DES spectra of wild-type (blue), PSII-minus (orange), and PSI-minus (yellow) membrane fragments, shown as the average from three scans. Spectral locations correspond to the points on the 2D spectrum, clockwise from top right: $\lambda_{exc} = 667$ nm, $\lambda_{det} = 667$ nm (black), $\lambda_{exc} = 679$ nm, $\lambda_{det} = 686$ nm (cyan), $\lambda_{exc} = 679$ nm, $\lambda_{det} = 694$ nm (pink), $\lambda_{exc} = 679$ nm, $\lambda_{det} = 701$ nm (blue), and $\lambda_{exc} = 684$ nm, $\lambda_{det} = 695$ nm (green). Shaded area indicates ± the standard error of the mean (σ) from three scans.

nm. Both PSI and PSII absorbances fall under this peak, with the PSI absorbance (centered at 680 nm) slightly red-shifted relative to the PSII absorbance (centered at 670 nm). The spectral contributions of the photosystems are inseparable in the wild-type, so we employ mutant strains lacking one of the photosystems to investigate the spectral signatures of each photosystem. In this preliminary dataset, the PSI-minus sample had a higher scatter background and lower OD compared to the wild-type and PSII-minus samples. These factors contribute to the higher noise floor and lower signal-to-noise ratio observed in 2D spectra and waiting time traces for the PSI-minus sample.

Figure 6.2 shows absolute valued 2DES spectra of wild-type, PSII-minus, and PSI-minus

membrane fragments at waiting times of 0, 60, and 500 fs. The wild-type and PSII-minus spectra show relaxation to 720 nm due to the red Chl content of PSI. The PSI-minus spectra are blue-shifted relative to the PSII-minus. Waiting time dynamics from the indicated points are shown in Figure 6.3 for short times (< 2 ps). PSI-minus spectra show predominant diagonal features centered around 667 nm and 676 nm which relax down to 700 nm within the first 60 fs. The 667 diagonal feature decays quickly in all three samples. Spectra and waiting time traces from the PSI-minus membranes have significantly lower signal-to-noise due to the lower concentration and higher scatter background in these samples.

Long waiting times dynamics (1 ps - 1 ns) are shown in Figure 6.4. Long waiting times spectra were normalized at 1 ps to the maximum value in the normalized short times 1 ps spectra. In the wild-type and PSII-minus samples, most of the signal decays within the first 100 ps. The PSI-minus sample may have a longer-lived signal, but the low signal-to-noise ratio makes this assessment inconclusive.

Pump-probe spectra were separately acquired for the wild-type membrane samples. These data were used to determine the absolute phase of the 2DES spectra according to the projection slice theorem. [10] Figure 6.5 shows phased absorptive 2DES spectra from a single scan of wild-type membranes. As in the absolute valued data, the wild-type membranes show ultrafast energy transfer from the 680 nm feature down to 720 nm.

6.3 Inter-Complex Energy Transfer

An excitation originating on a given PSI monomer has a 50.6% probability of being trapped by the P700 reaction center on that monomer. There is a 35.3% probability that the excitation is trapped by the RC on one of two neighboring monomers that are part of the same trimer and a 6.1% probability that the excitation is trapped by the RC on an adjacent monomer that is not part of the same trimer. [11] The center-to-center distance between PSI monomers within a trimer is 10-11 nm which is comparable to the LH2-LH2 and LH2-LH1 separation in *Rba. sphaeroides*. [11, 12] Given the high density of reaction centers, excita-

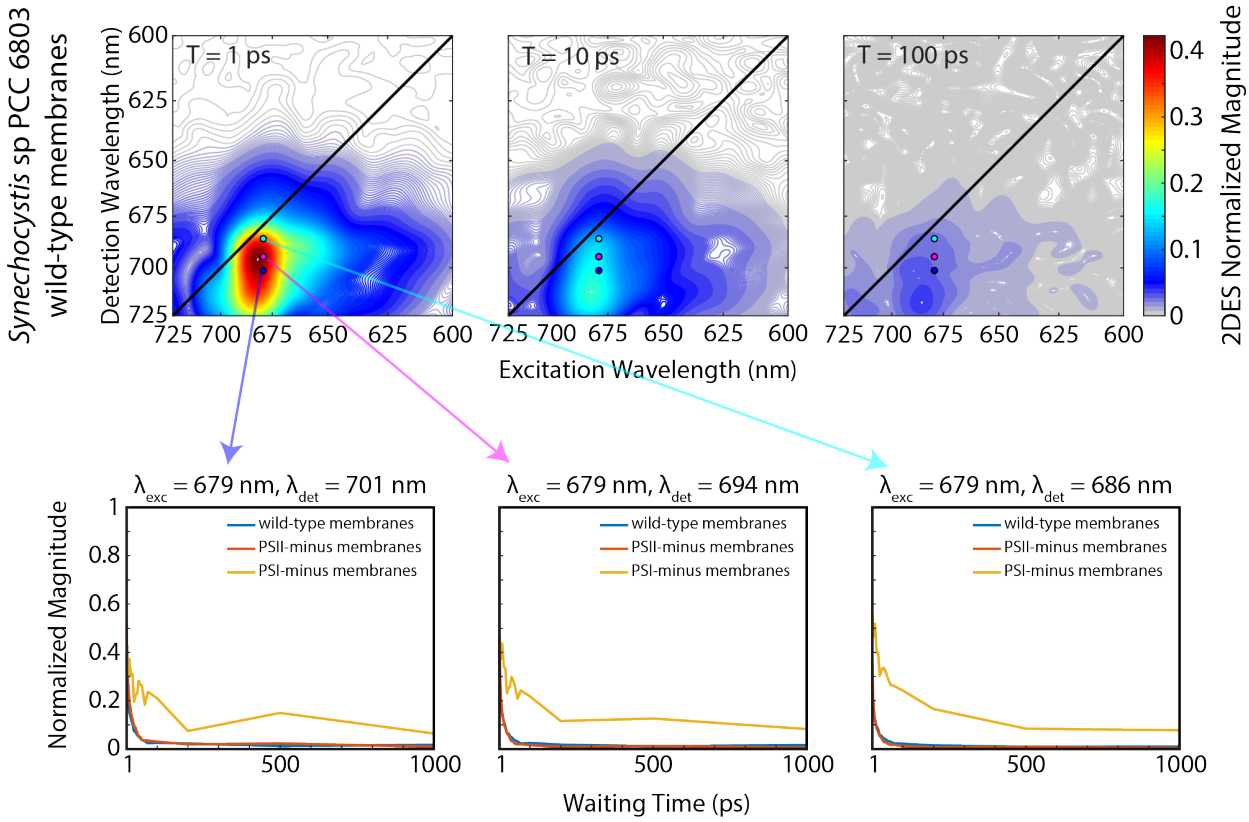

Figure 6.4: (top) Normalized absolute valued two-dimensional electronic spectra of membrane fragments from wild-type *Synechocystis* sp PCC 6803 at waiting times of 1, 10, and 100 ps. (bottom) Waiting time traces from absolute valued 2DES spectra of wild-type (blue), PSII-minus (orange), and PSI-minus (yellow) membrane fragments. Spectra and waiting time traces are shown as an average from three scans.

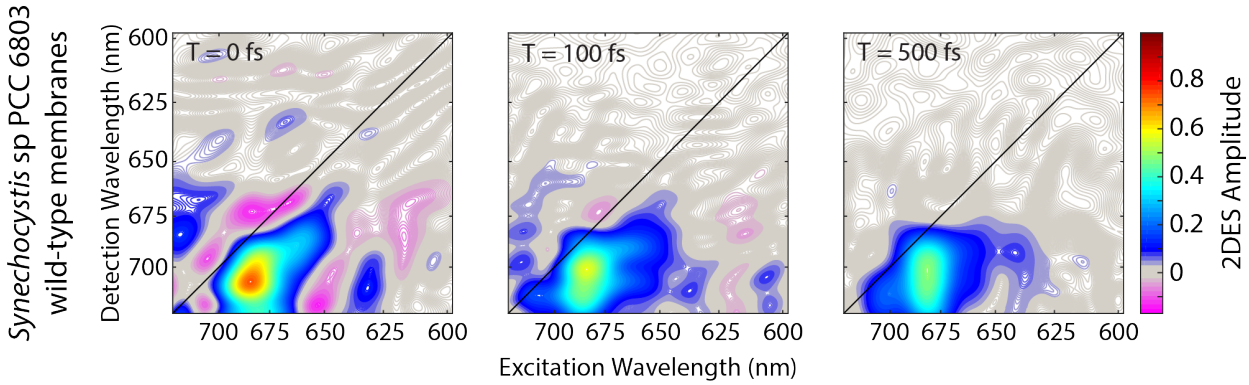

Figure 6.5: Absorptive 2DES spectra of wild-type *Synechocystis* sp PCC 6803 membrane fragments at waiting times of 0, 100, and 500 fs from a single scan. Spectra were phased by fitting to separately acquired pump-probe spectra according to the projection slice theorem.

tions are unlikely to migrate far through the network of PSI trimers. Therefore, to generate a sufficient excitation density to achieve exciton-exciton annihilation, a higher power will be needed than was required for annihilation in *Rba. sphaeroides*.

We collected long waiting times data on wild-type *Synechocystis* membrane fragments at a high power (460 μW per beam), medium power (210 μW per beam), and low power (60 μW per beam) to investigate whether annihilation was present in the high power sample (Figure 6.6). Results for the low power experiment are not shown due to low signal:noise. We expect to observe shorter lifetimes in high power samples if annihilation is present. The long waiting time dynamics are similar at high and medium powers, indicating that very little, if any, annihilation is present at high power. Due to the experimental constraint of GRAPES in which the entire beam is focused to a line instead of a single point, we will not be able to achieve high enough power to achieve significant annihilation with the current experimental setup. Our high power of 460 μW per beam is analogous to 1-2 nJ/pulse for a 50 μm spot size at the sample. Lee et al. observed annihilation in isolated PSI complexes in a power dependence study at 14.5 nJ/pulse for a 71 μm spot size. [4] To observe annihilation in GRAPES, we could increase the flux by focusing more tightly at the sample and decreasing the vertical height of the beam at the sample, but these improvements are unlikely to produce the high excitation density required for annihilation.

We plan to repeat a power dependence study as a pump-probe experiment to achieve a higher excitation density for annihilation in thylakoid membranes to recover the PSI-PSI and PSII-PSII inter-complex transfer rates. These experiments will additionally need to be performed on PSI-only and PSII-only mutants to distinguish the unique inter-complex hopping rates between each of these spectrally overlapping complexes.

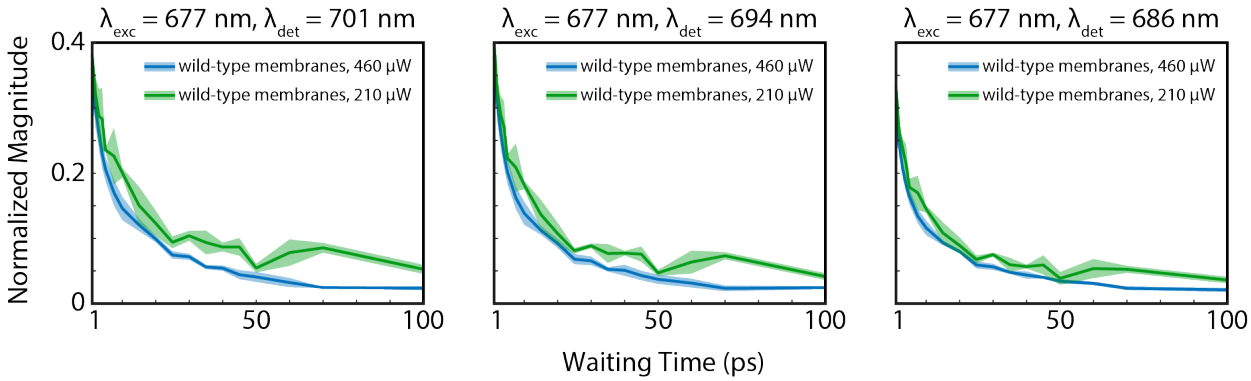

Figure 6.6: Waiting time traces from absolute valued 2DES spectra of wild-type *Synechocystis* sp PCC 6803 membrane fragments at two different pulse powers, 460 μW (blue) and 210 μW (green). The similar observed lifetimes at these two powers indicate that the dynamics are not dominated by annihilation in the high power experiment.

6.4 Path Forward to Map Inter-Complex Energy Transfer and Disentangle Spectral Contributions

Replication of the preliminary results as well as further experiments are needed to map out the spectral contributions of the photosystems and inter-complex energy pathways. We will repeat the preliminary 2DES experiments using more concentrated PSI-minus samples to improve the signal-to-noise. By fitting weighted sums of the early times decay dynamics of the PSI and PSII features, we will recover the relative ratio of each photosystem in the wild-type membranes. We will additionally collect pump-probe data to phase all samples and generate absorptive spectra. Power dependence experiments to investigate inter-complex energy transfer will be performed using pump-probe to achieve high enough excitation densities for singlet-singlet annihilation.

REFERENCES

[1] L. Bar-Eyal, A. Shperberg-Avni, Y. Paltiel, N. Keren, and N. Adir. Light harvesting in cyanobacteria: The phycobilisomes. In R. Croce, R. van Grondelle, H. van Amerongen, and I. H. van Stokkum, editors, *Light Harvesting in Photosynthesis*, book section 5. CRC Press, Boca Raton, FL, 2018.

[2] Y. Umena, K. Kawakami, J. R. Shen, and N. Kamiya. Crystal structure of oxygen-evolving photosystem II at a resolution of 1.9 Å. *Nature*, 473(7345):55–60, 2011.

[3] M. Sener, J. Strumpfer, J. Hsin, D. Chandler, S. Scheuring, C. N. Hunter, and K. Schulten. Forster energy transfer theory as reflected in the structures of photosynthetic light-harvesting systems. *Chem. Phys. Chem.*, 12:518–531, 2011.

[4] Y. Lee, M. Gorka, J. H. Golbeck, and J. M. Anna. Ultrafast energy transfer involving the red chlorophylls of cyanobacterial photosystem I probed through two-dimensional electronic spectroscopy. *J. Am. Chem. Soc.*, 2018.

[5] J. M. Hayes, S. Matsuzaki, M. Ratsep, and G. J. Small. Red chlorophyll *a* antenna states of photosystem I of the cyanobacterium *Synechocystis* sp. PCC 6803. *J. Phys. Chem. B*, 104:5625–5633, 2000.

[6] L. O. Palsson, C. Flemming, B. Gobets, R. van Grondelle, J. P. Dekker, and E. Schlodder. Energy transfer and charge separation in photosystem I: P700 oxidation upon selective excitation of the long-wavelength antenna chlorophylls of *Synechococcus elongatus*. *Biophys. J.*, 74:2611–2622, 1998.

[7] K. Satoh. Introduction to the photosystem II reaction center - isolation and biochemical and biophysical characterization. In D. R. Ort and C. F. Yocum, editors, *Oxygenic Photosynthesis: The Light Reactions*, pages 193–211. Kluwer Academic Publishers, Dordrecht, 1996.

[8] Y. Shibata, S. Nishi, K. Kawakami, J. R. Shen, and T. Renger. Photosystem II does not possess a simple excitation energy funnel: time-resolved fluorescence spectroscopy meets theory. *J. Am. Chem. Soc.*, 135(18):6903–6914, 2013.

[9] J. Pan, A. Gelzinis, V. Chorosajev, M. Vengris, S. S. Senlik, J. R. Shen, L. Valkunas, D. Abramavicius, and J. P. Ogilvie. Ultrafast energy transfer within the photosystem II core complex. *Phys. Chem. Chem. Phys.*, 19(23):15356–15367, 2017.

[10] T. Brixner, T. Mancal, I. V. Stiopkin, and G. R. Fleming. Phase-stabilized two-dimensional electronic spectroscopy. *J. Chem. Phys.*, 121:4221–4236, 2004.

[11] C. MacGregor-Chatwin, M. Sener, S. F. H. Barnett, A. Hitchcock, M. C. Barnhart-Dailey, K. Maghlaoui, J. Barber, J. A. Timlin, K. Schulten, and C. N. Hunter. Lateral segregation of photosystem I in cyanobacterial thylakoids. *Plant Cell*, 29(5):1119–1136, 2017.

[12] P. D. Dahlberg, P.-C. Ting, S. C. Massey, M. A. Allodi, E. C. Martin, C. N. Hunter, and G. S. Engel. Mapping the ultrafast flow of harvested solar energy in living photosynthetic cells. *Nat. Commun.*, 8:988–994, 2017.

CHAPTER 7

FUTURE DIRECTIONS

There remain many exciting avenues in bacterial photosynthesis that can be explored with 2DES as well as steady-state techniques such as circular dichroism (CD) spectroscopy. The first proposed experiment presented here follows up on an interesting CD result observed in isolated LH2 and LH2-only membranes. The next two experiments involve exploration of photoprotection and the effect of environmental stressors on light harvesting in cyanobacteria. The Engel group's unique capabilities to conduct real-time 2DES experiments on live cells has brought the study of *in vivo* photoprotective mechanisms close to fruition. Finally, membrane and *in vivo* samples can be used to investigate the effects of environmental stressors, such as iron depletion, on ultrafast light-harvesting dynamics.

7.1 Linear Circular Dichroism of LH2

I collected linear circular dichroism (CD) spectra of both isolated LH2 from semi-aerobically grown wild-type *Rba. sphaeroides* and membrane fragments from a semi-aerobically grown LH2-only mutant of *Rba. sphaeroides*, shown in Figure 7.1. The spectrum of isolated LH2 matches closely with CD spectra published by Georgakopoulou et al. [1]. The isolated and membrane-bound LH2 samples exhibit similar spectral characteristics in the 800-900 nm region of the spectrum, but differ on the blue edge of the B800 peak in the 750-800 nm region. While the isolated LH2 shows a negative feature, recovers to 0, and then dips negative again before the B800 feature, LH2-only membranes only show a negative feature in this region. This difference persisted across a number of different samples. We were unable to collect CD spectra of intact cells with acceptable signal-to-noise in the 750-900 nm spectral region.

CD spectra of the diatom *Phaeodactylum tricornutum* have shown variations in the CD spectra as the system is studied at varying levels: whole cells, purified thylakoid membranes, and isolated fucoxanthin chlorophyll protein (FCP) complexes. [2]

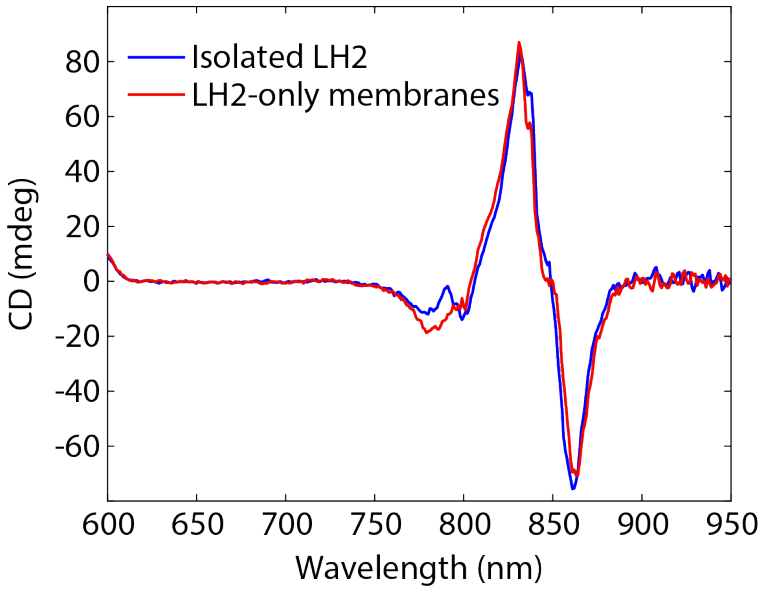

Figure 7.1: Linear CD spectra of LH2 isolated from semi-aerobically grown wild-type *Rba. sphaeroides* (blue) and membrane fragments from a semi-aerobically grown LH2-only mutant of *Rba. sphaeroides*. We acknowledge the UChicago BioPhysics Core Facilities for use of the Jasco J-1500 CD spectrometer.

It should be noted that these samples were prepared in 2015 and have been stored at -80 °C. The isolated LH2 is believed to be intact and functional, as the linear CD does match the literature, but we do not know the long-term storage integrity of the membrane fragments. Therefore, fresh cultures of wild-type and LH2-only *Rba. sphaeroides* should be grown up, disrupted to prepare membrane fragments, and analyzed by CD. Further efforts to obtain CD spectra of intact cells would also be worthwhile to see the effect of this additional level of organization and complexity.

7.2 Determining the Energy Quenching Pathway via the OCP in Cyanobacteria

Once a chlorophyll (Chl) molecule has been excited, the excitation may be transferred for photosynthesis, fluoresce from the Chl molecule, undergo intersystem crossing to form triplet Chl and then cause the formation of reactive oxygen species (ROS), or be quenched by a nonphotochemical quenching (NPQ) mechanism that dissipates the energy as heat. [3]

In cyanobacteria, photoactivation of the orange carotenoid protein (OCP) induces sub-picosecond quenching of the phycobilisome, the cyanobacterial light-harvesting antenna, preventing energy transfer from the phycobilisome to photosystems I or II for photosynthesis, illustrated in Figure 7.2. [4] In the photoactivated form, OCP is able to quench 80% of excitations from the phycobilisome. [5] The Engel group is well equipped to determine whether the ultrafast OCP quenching mechanism takes place via direct energy transfer from the phycobilisome to the OCP, or whether OCP binding induces a conformational change in the phycobilisome that nonradiatively quenches excitations without energy transfer to the OCP. Broadband *in vivo* 2DES measurements of cyanobacteria will enable investigation of the OCP NPQ mechanism.

The OCP is a pigment-protein complex containing a single carotenoid molecule, 3'-hydroxychinenone (hECN). [6] Photoactivation under blue-green illumination exposes the carotenoid by separating the C-terminal domain of the protein from the N-terminal domain. [7–9] This reorientation transforms the inactive orange form of the complex, OCP^O into the activated red form, OCP^R. The exposed carotenoid in OCP^R is then able to bind to the phycobilisome to induce quenching with a separation of only 5-10 Å between the carotenoid molecule and the phycobilisome core chromophores at the site of allophycocyanin APC_Q^{660}. [4, 5, 7, 10] The exact OCP binding site and the model of OCP-PBS interaction are unknown. [3] I hypothesize that the close contact of the OCP with the PBS core will enable quenching by direct energy transfer from the phycobilisome core to hECN.

There are two possible mechanisms for direct quenching by the OCP which should be distinguishable by *in vivo* 2DES: (1) charge transfer from APC_Q^{660} to the OCP, or (2) excitonic energy transfer from the phycobilisome core to the S_1 state of hECN. Our *in vivo* 2DES is uniquely suited to test these mechanisms due to our ability to observe real-time dynamics spanning a broadband spectrum in intact cells with ultrafast time resolution. To confirm mechanism (1), we would detect a near-infrared signal that corresponds to the carotenoid radical cation resulting from the charge transfer state. [11]. To confirm mechanism (2), we

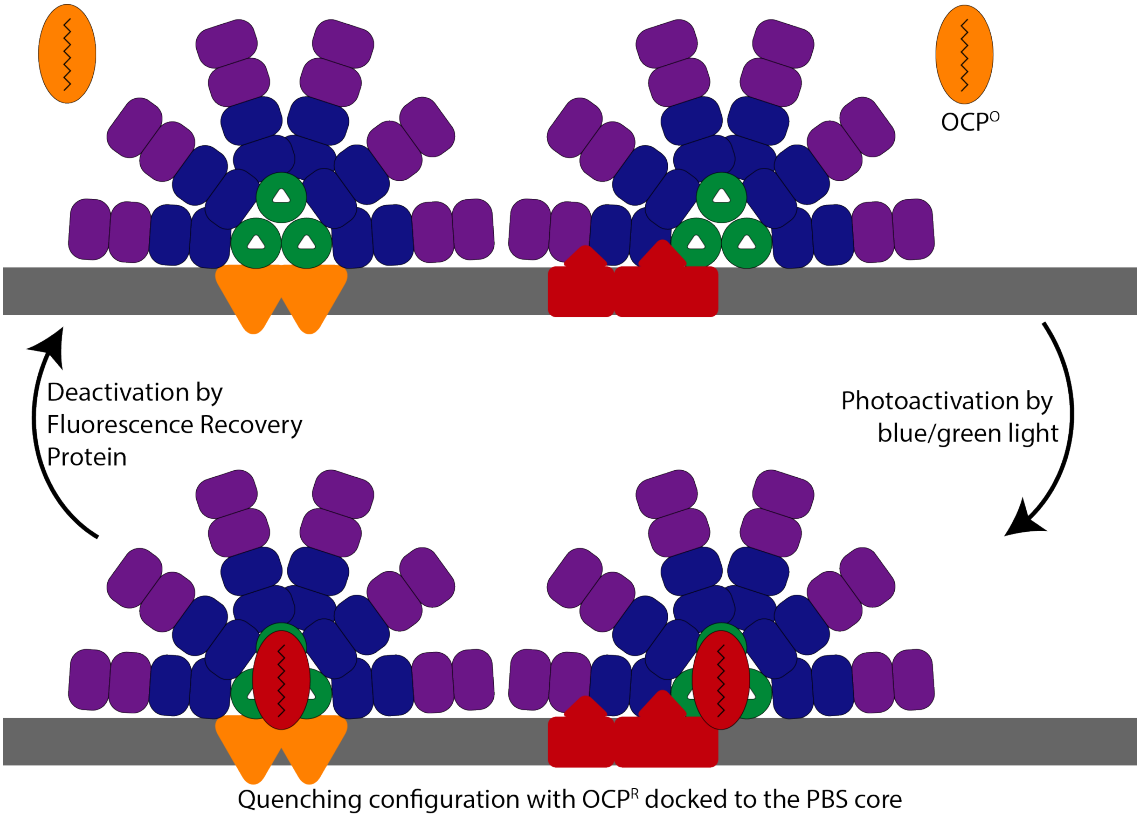

Figure 7.2: (Top) Unquenched configuration and (Bottom) quenched configuration by OCP photoprotection. Upon photoactivation converting the inactive OCP^O to the active OCP^R, OCP^R docks to the PBS core and causes quenching of excitations from the PBS. OCP^R can be deactivated to OCP^O by the fluorescence recovery protein.

would monitor ESA signals from the hECN S_1 to S_N transition corresponding to excited state absorption to higher-lying carotenoid excited states. Since S_1 is an optically dark state, we would not see stimulated emission from this state. Both of these experiments would require broadband 2DES or a 2-color experiment to pump in the visible region and probe in either the near-IR or bluer visible wavelengths to observe the CT signature or ESA from S_1.

We have obtained wild-type and ΔOCP strains of *Synechocystis* sp PCC 6803 from Prof. Neil Hunter's group, which would allow for a control species for this study. However, due to issues with scatter from the *Synechocystis* cells, we may need to look for a ΔOCP mutant of a smaller cyanobacterial species.

7.3 Effect of Iron Stress on Light Harvesting in Cyanobacteria

Under low iron conditions, cyanobacterial growth is limited and PSI concentration decreases drastically due to its high iron content. PSI contains 3 iron-sulfur centers used for electron transport. [12] Under iron stress, the organisms produce a chlorophyll-binding pigment-protein complex called IsiA (iron stress induced protein A) which is encoded by the *isiA* gene. [13, 14] IsiA proteins encircle PSI under iron-deficient conditions forming light-harvesting supercomplexes with containing up to 21 IsiA around a PSI trimer. [13] These supercomplexes have twice the light-harvesting capacity of a PSI trimer in the absence of IsiA, increasing the efficiency of each PSI while the overall concentration of PSI is decreased. [15, 16] IsiA absorbs at 670 nm, providing a downhill gradient for energy transfer from IsiA to PSI. In addition to increasing the light-harvesting capacity of PSI, IsiA also causes an increased electron transfer rate through PSI. [14] Other IsiA proteins form rings without PSI that are believed to have a photoprotective function for PSII by absorbing and dissipating excess excitations. [13] Figure 7.3 shows illustrations of IsiA-PSI supercomplexes and IsiA supercomplexes that have been observed under iron stress conditions. [12, 13]

We already have on hand membrane fragments from IsiA-containing PSII-minus cells. Prof. Neil Hunter's group also has a Δ*isiA* mutant of *Synechocystis* sp that would be a

Figure 7.3: Illustration of (left) PSI-IsiA supercomplex with 18 IsiA proteins encircling a PSI trimer and (right) an IsiA supercomplex containing an outer ring of 19 IsiA proteins and inner ring of 13 IsiA proteins. Both types of supercomplexes may form under iron stress conditions.

useful sample for this study. Wild-type, PSI-minus, or PSII-minus cells could be grown under the same iron-stress conditions as the $\Delta isiA$ mutant and additionally compared to strains grown under iron-replete conditions.

In addition to investigating the energy transfer pathway from IsiA to PSI and the energy dissipation within IsiA using 2DES, CD spectroscopy and chiral 2DES of these IsiA supercomplexes is also worth exploring. The rings of IsiA around PSI may result in interesting static chirality and chiral dynamics. Figure 7.4 shows linear absorbance spectra of PSII-minus and iron-starved PSII-minus membrane fragments from *Synechocystis* sp. The iron-starved PSII-minus mutant shows a blue-shift of the Chl absorbance peak consistent with the IsiA complex. These data should be repeated to additionally compare to a PSII-minus sample that is not iron-starved, as well as an iron-starved wild-type sample to determine which factors are contributing to the spectral changes.

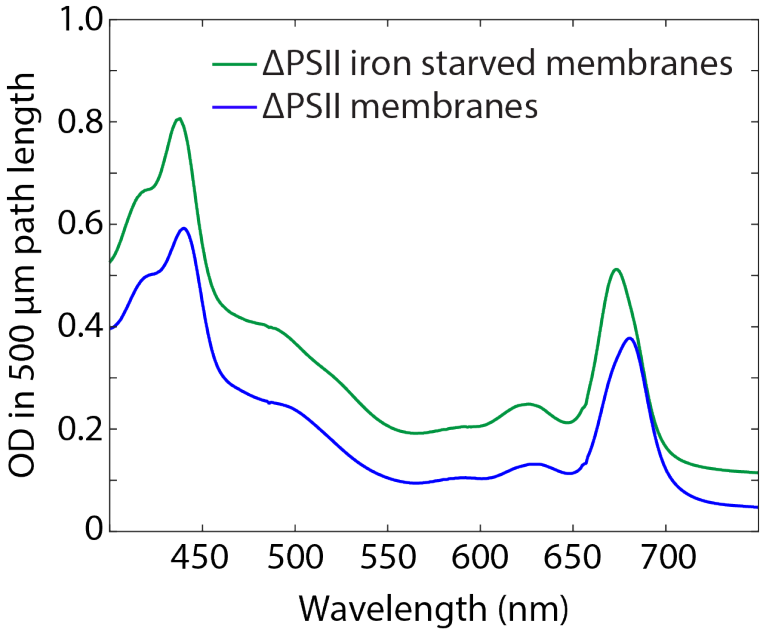

Figure 7.4: Linear absorbance spectra of PSII-minus (blue) and iron-starved PSII-minus (green) *Synechocystis* sp. The Chl absorbance near 680 nm is blue-shifted in the iron-starved PSII-minus mutant, consistent with the presence of the IsiA complex.

REFERENCES

[1] S. Georgakopoulou, R. N. Frese, E. Johnson, C. Koolhaas, R. J. Cogdell, R. van Grondelle, and G. van der Zwan. Absorption and CD spectroscopy and modeling of various LH2 complexes from purple bacteria. *Biophys. J.*, 82:2184–2197, 2002.

[2] M. Szabo, B. Lepetit, R. Goss, C. Wilhelm, L. Mustardy, and G. Garab. Structurally flexible macro-organization of the pigment-protein complexes of the diatom *Phaeodactylum tricornutum*. *Photosynth. Res.*, 95(2-3):237–245, 2008.

[3] A. Pinnola, D. Kirilovsky, and R. Bassi. Photoprotective excess energy dissipation. In R. Croce, R. van Grondelle, H. van Amerongen, and I. H. van Stokkum, editors, *Light Harvesting in Photosynthesis*, book section 11. CRC Press, Boca Raton, FL, 2018.

[4] L. Tian, M. Gwizdala, I. H. van Stokkum, R. B. Koehorst, D. Kirilovsky, and H. van Amerongen. Picosecond kinetics of light harvesting and photoprotective quenching in wild-type and mutant phycobilisomes isolated from the cyanobacterium *Synechocystis* PCC 6803. *Biophys. J.*, 102(7):1692–1700, 2012.

[5] L. Tian, I. H. van Stokkum, R. B. Koehorst, A. Jongerius, D. Kirilovsky, and H. van Amerongen. Site, rate, and mechanism of photoprotective quenching in cyanobacteria. *J. Am. Chem. Soc.*, 133(45):18304–11, 2011.

[6] D. Kirilovsky and C. A. Kerfeld. The orange carotenoid protein in photoprotection of photosystem II in cyanobacteria. *Biochim. Biophys. Acta*, 1817(1):158–166, 2012.

[7] R. L. Leverenz, M. Sutter, A. Wilson, S. Gupta, A. Thurotte, C. B. de Carbon, C. J. Petzold, C. Ralston, F. Perreau, D. Kirilovsky, and C. A. Kerfeld. A 12 Å carotenoid translocation in a photoswitch associated with cyanobacterial photoprotection. *Science*, 348(6242):1463–1466, 2015.

[8] A. Wilson, J. N. Kinney, P. H. Zwart, C. Punginelli, S. D'Haene, F. Perreau, M. G. Klein, D. Kirilovsky, and C. A. Kerfeld. Structural determinants underlying photoprotection in the photoactive orange carotenoid protein of cyanobacteria. *J. Biol. Chem.*, 285(24):18364–18375, 2010.

[9] S. Gupta, M. Guttman, R. L. Leverenz, K. Zhumadilova, E. G. Pawlowski, C. J. Petzold, K. K. Lee, C. Y. Ralston, and C. A. Kerfeld. Local and global structural drivers for the photoactivation of the orange carotenoid protein. *Proc. Natl. Acad. Sci. USA*, 112(41):E5567–E5574, 2015.

[10] D. Harris, O. Tal, D. Jallet, A. Wilson, D. Kirilovsky, and N. Adir. Orange carotenoid protein burrows into the phycobilisome to provide photoprotection. *Proc. Natl. Acad. Sci. USA*, 113(12):E1655–E1662, 2016.

[11] N. E. Holt, D. Zigmantas, L. Valkunas, X. P. Li, K. K. Niyogi, and G. R. Fleming. Carotenoid cation formation and the regulation of photosynthetic light harvesting. *Science*, 307(5708):433–436, 2005.

[12] E. J. Boekema and D. A. Semchonok. Organization of photosynthetic membrane proteins into supercomplexes. In R. Croce, R. van Grondelle, H. van Amerongen, and I. H. van Stokkum, editors, *Light Harvesting in Photosynthesis*, book section 10. CRC Press, Boca Raton, FL, 2018.

[13] N. Yeremenko, R. Kouril, J. A. Ihalainen, S. D'Haene, N. van Oosterwijk, E. G. Andrizhiyevskaya, W. Keegstra, H. L. Dekker, M. Hagemann, E. J. Boekema, H. C. P. Matthijs, and J. P. Dekker. Supramolecular organization and dual function of the IsiA chlorophyll-binding protein in cyanobacteria. *Biochemistry*, 43:10308–10313, 2004.

[14] J. Sun and J. H. Golbeck. The presence of the IsIA-PSI supercomplex leads to enhanced photosystem I electron throughput in iron-starved cells of *Synechococcus* sp. PCC 7002. *J. Phys. Chem. B*, 119(43):13549–13559, 2015.

[15] A. N. Melkozernov, T. S. Bibby, S. Lin, J. Barber, and R. E. Blankenship. Time-resolved absorption and emission show that the CP43' antenna ring of iron-stressed *Synechocystis* sp. PCC6803 is efficiently coupled to the photosystem I reaction center core. *Biochemistry*, 42:3892–3903, 2003.

[16] E. G. Andrizhiyevskaya, D. Frolov, R. Van Grondelle, and J. P. Dekker. Energy transfer and trapping in the photosystem I complex of *Synechococcus* PCC 7942 and in its supercomplex with IsiA. *Biochim. Biophys. Acta*, 1656(2-3):104–113, 2004.

CHAPTER 8

CONCLUSIONS

Absorption and ultrafast energy transfer events initiate the process that leads to charge separation and ultimately the production of ATP in photosynthetic organisms. This thesis brings new insight to these ultrafast processes in *Rba. sphaeroides* and *Synechocystis* sp and additionally makes spectroscopic advances giving us the tools to observe the dynamics of transition dipole orientations with two-dimensional anisotropy spectroscopy.

I used 2D anisotropy to reveal ultrafast energy transfer in membrane-bound LH2 from higher-lying B850* excited states to B850, coinciding with a transition from out-of-plane B850* states to in-plane B850 states. Our results also showed an orientational preference for excited state absorption along the same transition axis as the initial excitation, as well as ultrafast equilibration within the manifold of B850 states. These experimental results were supported by modified Redfield theory calculations.

The carotenoid switch from spheroidene to spheroidenone in semi-aerobic growth conditions was proposed to introduce an energy quenching pathway from BChl to the carotenoid. Our results did not provide sufficient evidence of this pathway by monitoring the BChl lifetimes. We proposed two-color experiments to follow up on this work to directly interrogate the carotenoid S_1 dark state.

A power dependence study of isolated LH2 and LH2-only membranes revealed power-dependent dynamics of B850 on the 150-1000 fs timescale, revising the pre-existing picture of B850 dynamics. We propose that the slow decay of the B850 signal observed at high powers is due to singlet-singlet annihilation from B800-B850 intra-complex energy transfer.

We report the first 2DES spectra of cyanobacterial thylakoid membranes, using a series of mutant strains alongside the wild-type *Synechocystis* sp PCC 6805 to disentangle the spectral contributions of photosystems I and II. We show preliminary power dependence data and propose future experiments to determine inter-complex rates of energy transfer using pump-probe spectroscopy.

Spectroscopic experiments on photosynthetic membranes allow us to study energy transfer dynamics of pigment-protein complexes in the greater context of their native environment, capturing effects such as inter-complex hopping and removing the influence of a detergent solvent environment. We continue to push forward in pursuing *in vivo* experiments in cyanobacteria. I have proposed experiments to study the nonphotochemical quenching mechanism of the orange carotenoid protein in live cells of cyanobacteria. We are also interested in the response of these organisms to changes in their environments. Future directions include the study of iron starvation effects through the incorporation of IsiA pigment-protein complexes in *Synechocystis* sp. The experiments presented here push toward the study of photosynthetic systems as they respond to dynamic environments.